UNIVERSITY OF COPENHAGEN

Master of Science in Astrophysics

Resolving the Properties of Dust and Stellar Populations of Nearby Galaxies with the Hubble Space Telescope

Clara Giménez Arteaga

clara.arteaga@nbi.ku.dk

Supervised by Dr Gabriel Brammer

June 30, 2020

Clara Giménez Arteaga
`clara.arteaga@nbi.ku.dk`
Resolving the Properties of Dust and Stellar Populations of Nearby Galaxies with the Hubble Space Telescope
Master of Science in Astrophysics, June 30, 2020
Supervisors: Dr Gabriel Brammer

University of Copenhagen
Niels Bohr Institute
The Cosmic Dawn Center (DAWN)
Lyngbyvej 2
2100 Copenhagen Ø

Abstract

To understand how galaxy formation and evolution proceed, spectral energy distributions (SEDs) of hundreds of thousands of galaxies are modelled, in order to estimate their redshifts and study the properties of their gas, dust and stellar population. To derive these intrinsic properties, one must have an in-depth understanding of the dust content of the sources, since it modifies the galaxies' inherent SEDs in a wavelength-dependent way, in terms of both extinction and reddening.

In this work, we use recently obtained and processed images from the Hubble Space Telescope to study the properties of a sample of 53 nearby star-forming galaxies at $z < 0.05$. Of these objects, 24 are local infrared-luminous galaxies (LIRGs) in the GOALS survey and are likely reasonable analogues of dusty star-forming galaxies in the early Universe. We conduct this study with Hubble images of the local galaxies because this allows us to resolve structures on the scale of tens of parsecs that are unresolved in more distant galaxies. We obtain high spatial resolution dust extinction maps of the nearby galaxies by imaging them in narrow-band filters centered on the redshifted Hα and Paschen β (Paβ) Hydrogen recombination lines. By measuring the Balmer decrement with Hα and Paβ emission line maps, we can probe sites of ongoing star formation activity and dust reddening.

We fit stellar population synthesis models to the spatially resolved HST photometry to derive physical properties across the sample galaxies, such as the star formation rate, the stellar mass surface densities and continuum dust attenuation. By comparing the continuum attenuation to the one obtained with the decrement, we demonstrate that the diffuse dust in the interstellar medium is not the only source of extinction, and accounting for the birth cloud attenuation is also required. We compare results from two population synthesis fitting codes, EAZY and Prospector, which yield somewhat distinct results. These differences are driven by differing parametrisations of star formation histories. Finally, we investigate how the resolution of our photometric measurements affects the derived stellar masses and star formation rates of our galaxies by comparing the ensemble of spatially resolved measurements to quantities derived from integrated measurements of the galaxies as a single source. We conclude that we obtain distinct estimates for these quantities depending on the resolution of our observations. The integrated measurements underestimate the stellar masses and overestimate the SFRs, with respect to the spatially resolved photometry.

Contents

1 Introduction

The aim of this work is to obtain extinction maps of nearby galaxies in order to constrain their dust obscuration. For this, we first need to understand how we can obtain information in extragalactic astronomy, starting with an introduction of basic concepts. Since our work is based on two emission lines - Hα and Paschen-β - we also demonstrate how we can use emission lines to understand galaxies. To finalise this introductory chapter, we explain the importance of dust in galaxies and expand on the motivation for conducting this work.

In the next chapters we will further elaborate on our observations with the Hubble Space Telescope, our methodology to analyse the data and obtain our results, and a final discussion on the resulting images and study, as well as future perspectives of this work.

1.1 Concepts of Extragalactic Astronomy

Astrophysics could be thought of as a detective work. Just by getting clues and hints left along the path, we can uncover the mysteries of the Universe. But this detective work is harder than it seems, since we cannot have direct contact with our clues. Our primary way of shedding light into the matter is (no pun intended) light. By measuring the photons emitted by the different objects in the cosmos, we are able to derive physical parameters, to prove theories and compare with simulations. This allows us to explain why the Universe is as it is, and why it behaves as it does. We cannot go to the nearest galaxy with a thermometer and expect to get its temperature (at least not yet), but after years of international effort in all branches of physics, we can derive that temperature from the photons that the galaxy emits, since we know the physical processes involved in the production of those photons, as well as the conditions of the environment where they are produced.

One of the most surprising discoveries in the recent era of extragalactic astronomy was a realisation regarding how big our field of study is. When the Hubble Space Telescope (HST) looked at an apparently dark and empty spot in the sky, it found thousands of galaxies, in what is called the Hubble Deep Field (Williams *et al.*, 1996) (Figure 1.1). This also revealed that most of the observed galaxies in the field were young high-redshift sources, providing for the first time a landmark to look into the early Universe.

Figure 1.1: The Hubble Deep Field (HDF). It covers an area of 6.8 arcminutes squared, about one 24-millionth of the whole sky. The image was obtained with HST over ten consecutive days on December, 1995.

By observing galaxies at different redshifts, we also see the Universe at different stages of its existence, thus we can study the evolution that these complex systems undergo, trying to connect galaxies from the past with what we see in the local Universe, with the hypothesis that these distant old objects are the progenitors of our current neighbours.

One possible classification of galaxies relies on separating them between elliptical and spiral galaxies. An example of both can be seen in Figure 1.2. Galaxy structure (e.g., spiral and elliptical) seems to correlate with other properties, such as the star formation history. The existence of a causal relationship between structure and these other characteristics remains a key question in galaxy evolution. Spiral galaxies are observed as blue disk-like structures containing gas, dust, and star-forming regions, with older stellar populations within the dormant bulge around the centre of the galaxy. On the other hand, red elliptical galaxies have normally low star formation and are associated with being older. These elliptical galaxies that have ceased forming stars are called "quiescent". Galaxy evolution studies face the major challenge of understanding how and why star formation turns off. Many theoretical explanations have been proposed (see e.g., Man and Belli, 2018 for a review), but no definitive general agreement has yet been reached.

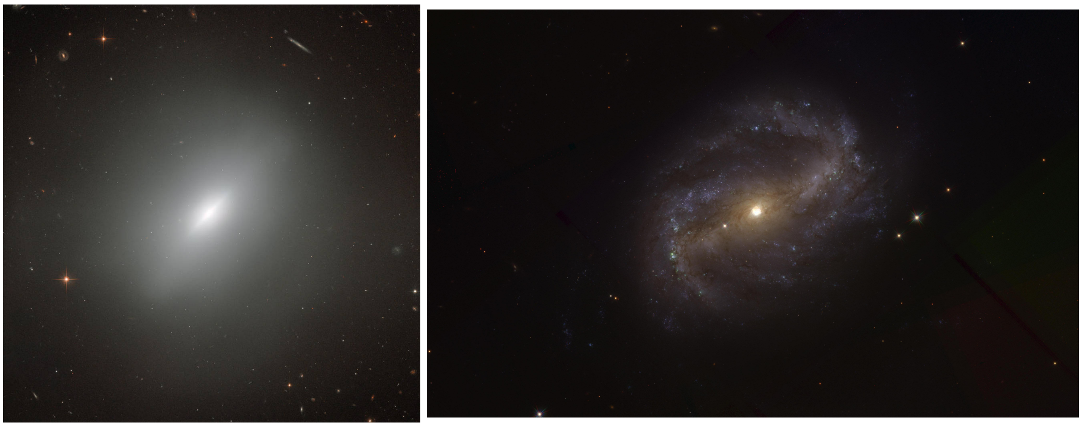

Figure 1.2: Example of the basic distinction between elliptical and spiral galaxies. On the left, the elliptical galaxy NGC 3610 observed by the Hubble Space Telescope. Credit: Francois Schweizer (CIW/DTM). On the right, one of our Dusty Cosmos galaxies - NGC 6217 - classified as a spiral.

The ultimate goal of the study of galaxy evolution would be to reach a deep understanding of the full sequence of events that happen from the formation of the first stars and galaxies, to the currently diverse Universe in shapes, masses, colours, sizes and many other properties of galaxies.

1.2 Galaxy Composition

A galaxy is an astronomical object that consists of a gravitationally bound system of stars and an interstellar medium (ISM) made of gas and dust. Using different observations we can separate and understand these components: continuum from stellar photospheres, emission lines for ionised and molecular gas, colours and line ratios for dust (as well as far-infrared emission of the dust itself). Later on we will examine in more detail the interplay between these components.

As an example, the well-studied nearby galaxy M51 - the Whirlpool Galaxy - has been observed across the whole electromagnetic spectrum and can be seen here in Figure 1.3. Each panel has a caption indicating the observed wavelength of the image, and what it would trace. The first four panels of the figure are obtained with HST broad- and narrow-band filters. The top left panel is generated from ultraviolet Hubble filters F275W, F336W and F435W, with bright blue knots showing clusters of young, massive stars. These regions correspond to bright areas in Hα and Paβ line emission (captured with HST narrow-band filters), shown in the middle panels, which trace ionised gas around the hot, young stars. We can also see that the dust lanes are most prominent in the UV image than in the near-IR, which is represented by the top right panel. In the UV, the dust is absorbing the stellar light, whereas its re-emission is directly observed in the far-IR, which traces the dust lanes. The top right image is generated from HST broad-band filters such as F110W, F814W and F689M, tracing the comparatively smooth continuum emission from older stars. On the other hand, by observing the J = 1-0 transition of the carbon monoxide (CO) molecule, we can trace the molecular gas content of M51, which is displayed in the bottom left panel of the figure. We can see a direct visual connection between Hα and Paβ and the CO traced gas in M51. The bottom right panel on Figure 1.3 shows the mid-IR observations obtained with Spitzer (Dumas *et al.*, 2011), which trace the continuum emission dominated by the stellar light that has been absorbed and re-emitted by dust.

1.3 Understanding Galaxies Through Emission Lines

Extensive knowledge can be gained from a galaxy spectrum, regarding all the physical processes that occur within the galaxy. A single spectrum enables us to learn about the formation history of the stellar population, the dust content, the metallicity, the pressure of the interstellar medium (ISM), the ongoing star formation rate (SFR), among others[1]. Galaxy spectra modelling has improved extensively over the last few decades. In upcoming chapters we expand on SED-fitting methods.

[1] High resolution spectra can also reveal the line-of-sight velocities of the gas and stars in galaxies, though here we concentrate on the overall shape of the galaxy spectral energy distributions.

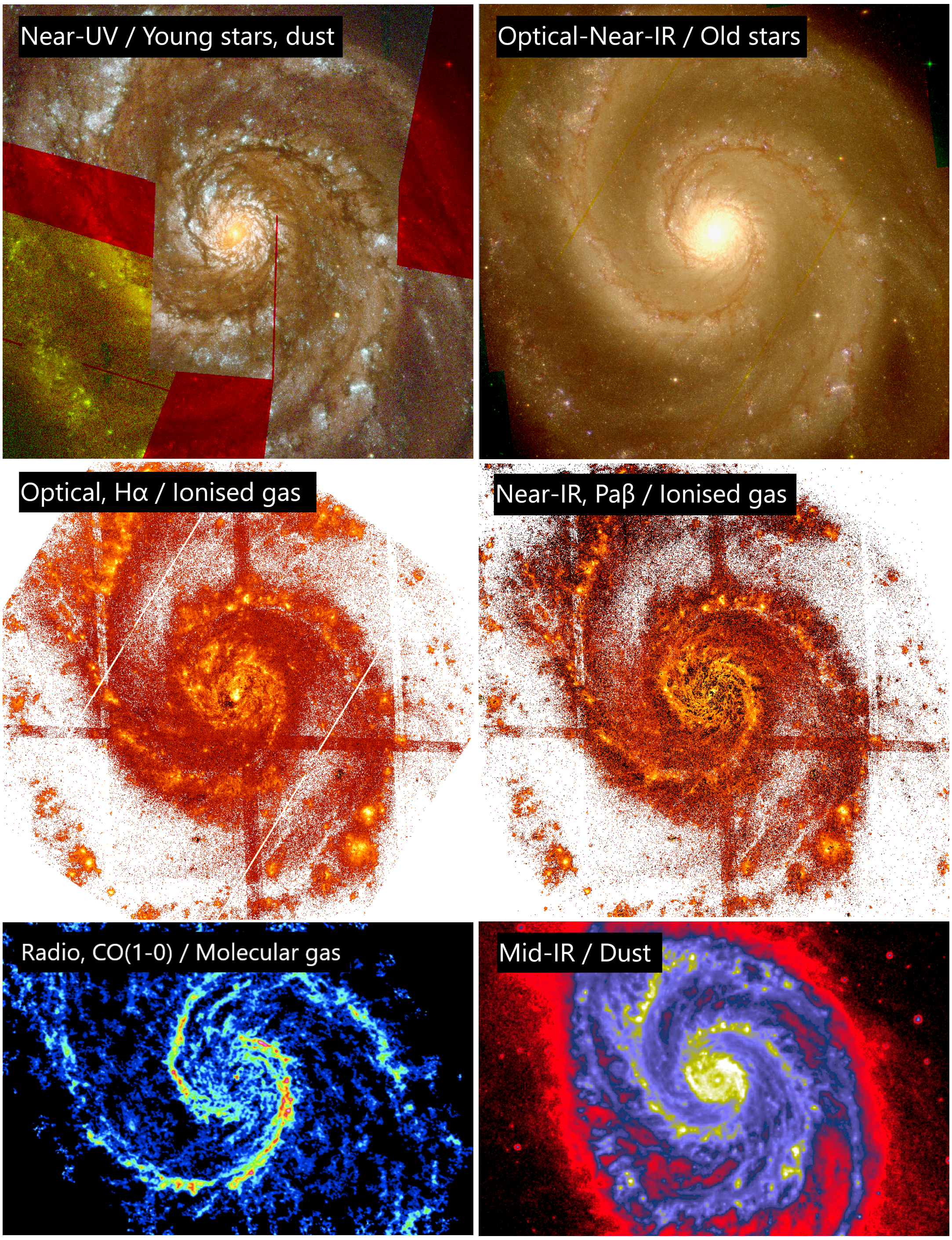

Figure 1.3: Observations of M51, in different parts of the spectrum. Each image represents a different luminous component of the galaxy. The top panels shows the stellar continuum emission: on the left, UV radiation of young stars, whereas on the right, light from the older stellar population. The middle panels show the recombination emission lines Hα and Paβ, emitted by ionised gas from HII regions surrounding young stars (Images Credit: NASA, ESA, STScI/AURA). The bottom left panel displays the CO(1-0) transition emission line detected with IRAM (Schinnerer *et al.*, 2013). The bottom right panel shows the mid-IR emission obtained with Spitzer at 8 μm (Dumas *et al.*, 2011), attributed mostly to dust re-emission of absorbed star light.

Spectral lines constitute powerful diagnostics of the physics and chemistry occurring within astronomical objects. The emission lines detected in a galaxy spectrum can be used to infer fundamental galaxy properties and to understand how these have changed across cosmic time. Emission lines have been broadly used to measure star formation rates or dust extinction (see Kennicutt, 1998; Calzetti *et al.*, 2007; Calzetti *et al.*, 2010; Calzetti, 2013). Other works have used emission lines to obtain the chemical abundance, excitation source of galaxies, ISM pressure and electron density (Kewley *et al.*, 2019).

Nowadays, we are able to explore the evolution of galaxies across 13 billion years of cosmic time, or up to $z \sim 11.1$ (GN-z11, Oesch *et al.*, 2016), thanks to the observations of multiple ground and space-based telescopes. As reviewed in Kewley *et al.*, 2019, these instruments cover the electromagnetic spectrum from the rest-frame UV emission-lines, which are vital for comprehending the first chapters of galaxy evolution, to the infrared lines. The whole spectrum is necessary to understand all phases of the evolution of galaxy properties. In the coming years, upcoming larger facilities such as the James Webb Space Telescope (JWST), will reach further than ever into the early Universe, allowing us to get a closer look at the first galaxies to ever exist.

1.3.1 Recombination lines, Hα and Paβ

According to the Bohr model of the atom, the atom's nucleus is surrounded by quantised energy levels where electrons exist. Each energy level is defined by its principal quantum number n. Electrons can only exist in these states and transit from one to the other, losing or gaining energy by emitting or absorbing photons, whose energy equals the energy difference between the initial and final levels. These photons can be detected in a galaxy spectrum as emission lines. Recombination lines are those that are produced when free electrons recombine with ions, and instead of going straight to the ground state, the electron cascades through the energy levels by emitting photons (Bohr, 1913).

In this work we use the recombination lines Balmer-alpha (Hα) and Paschen-beta (Paβ). Hα occurs when a hydrogen electron falls from its third to second lowest energy level. Hα has a rest-frame wavelength of 6564.6Å and lies in the visible part of the electromagnetic spectrum. Hα is widely used to trace ionised hydrogen in gas clouds- so-called HII regions - as can be seen in Figure 1.3, where Hα traces the ionised gas in M51. On the other hand, Paβ occurs when a hydrogen electron falls from its fifth to the third lowest energy level, emitting a photon. All Paschen lines lie in the infrared band. Paβ has a rest-frame wavelength of 1.2818 μm.

One could measure SFRs of galaxies by using hydrogen recombination lines such as Hα and Lyman-alpha (transition from the second to the first energy level). This method allows to trace massive star formation in a direct way, since star formation gives rise to nebular emission lines in ionised and excited HII regions.

Hα has crucial characteristics that make it the most commonly used among recombination lines. It is one of the most luminous lines, as well as much less sensitive to dust attenuation when compared to other nebular lines that fall towards bluer wavelengths. Despite this, other assumptions still affect Hα, such as the form of the initial mass function (IMF) and other features on stellar absorption (e.g., Calzetti *et al.*, 1994; Kennicutt, 1998; Sullivan *et al.*, 2001; Hopkins *et al.*, 2001; Rosa-González *et al.*, 2002; Kewley *et al.*, 2002). We can detect Hα with optical observations only at $z < 0.5$, and we need near-infrared (NIR) measurements to study it at higher redshifts.

For any observation, by measuring the Balmer decrement (the ratio of Hα to Hβ line fluxes) we can obtain trustworthy corrections on the extinction. As we explain in the following sections, we can also obtain extinction maps with the Hα/Paβ decrement.

1.4 The Importance of Dust in Galaxies

The diffuse interstellar medium (ISM) is composed of gas and dust that fills the space between the stars in a galaxy. Dust is less than 1% of the total mass of the ISM, which itself is only 10% of the luminous mass of the galaxy. Dust is formed and spread through the ISM in supernovae explosions and during the asymptotic giant branch phase (AGB) of a star's life (e.g., Draine, 2009; Hirashita, 2012). A typical size distribution of dust grains is $n(a) \propto a^{-3.5}$, where a is the radius of the dust particle, and is typically in the interval

$50\text{Å} < a < 0.25\mu$m. Dust grains in the ISM are mainly made up of silicate and carbon.

How do we know that there is dust in the ISM?

For starters, because of its interaction with starlight, since dust absorbs the ultraviolet (UV) emission of young stars and re-emits it in the infrared (IR) (e.g., see Figure 1.3). We observe total and wavelength-selective extinction of starlight (see Figure 1.4). We also observe reflection of starlight by dusty clouds located behind bright stars, polarisation of light, and absorption of starlight in silicate or ice bands. On the other hand, we also observe emission from dust grains: thermal continuum emission, IR emission bands from the heated grains and radio continuum emission from rotating grains. Finally, we can also know about the presence of dust in the ISM due to the depletion of chemical elements.

Why should we care or worry about dust?

At shorter wavelengths, extinction may diminish incoming radiation. On the other hand, at longer wavelengths emission from dust grains may dominate the continuum emission. Dust is also fairly important in chemical reactions, as it can act as a catalyst for interactions between other molecules. We also care about dust because it can serve as an independent tracer of physical conditions, for example, it can be used to indirectly infer the molecular gas mass. Furthermore, it is also important for calibration of many other tracers, such as for CO as a mass tracer.

In this work, we are primarily concerned with how the presence of dust affects other observables, rather than the intrinsic physics of dust production, grains, etc., that is its own whole field.

Our understanding of galaxy evolution is deeply influenced by the presence of dust in these astronomical objects. During its short lifetime in 1983, the InfraRed Astronomy Satellite (IRAS; Neugebauer *et al.*, 1984) revealed that the majority of galaxies in the local Universe had at least some dust content (Soifer *et al.*, 1987). This changed the way we approached dust until that moment. Astronomers stopped asking whether there was dust or not in the ISM, and started focusing on answering more complex questions, such as when

Figure 1.4: The Milky Way in stars and dust. A vast network of complex dust filaments obscuring the light from stars can be seen. Dust particularly obscures the galactic centre in visible light, which has an inferred visual extinction of $A_V \sim 40$ (Gao *et al.*, 2013) (Image credit: Serge Brunnier).

did galaxies begin to enhance their metals and dust content and how did these evolve across cosmic time.

Nowadays we implement extinction curves to our measurements, in an attempt to constrain and account for the effect of dust in the derived intrinsic properties of the sources. Extinction curves provide measurements of the wavelength-dependent cross-section between dust and light. To obtain observational measures of an extinction curve, individual stars need to be resolved. This has only been possible for the Milky Way, M31 and the Magellanic Clouds (Cardelli *et al.*, 1989; Bianchi *et al.*, 1996; Fitzpatrick, 1999; Gordon *et al.*, 2003; Calzetti, 2013).

For farther objects, we make the distinction between "attenuation" and "extinction". We define "extinction" as the effect caused by dust on starlight. Dust both attenuates and reddens the light from stars in a galaxy by absorbing and scattering the photons that they produce. A widely used assumption in treating the dust content is the foreground screen model. This model presumes that the dust is located in front of the star and separated from it. This simple approach is of course far from reality if we consider more complex systems, such as considering the diverse structures seen across the face of a large, extended galaxy (e.g., Fig. 1.3, see also Liu *et al.*, 2013). In the case of a galaxy, we no longer have dust in front of isolated stars and well separated from them. Instead, dust can mix in between stars and create complicated geometries. This is what we term "attenuation", the combination of extinction and geometry. Figure 1.5 shows the impact of the geometrical relation between dust and stars in the output spectrum of a source.

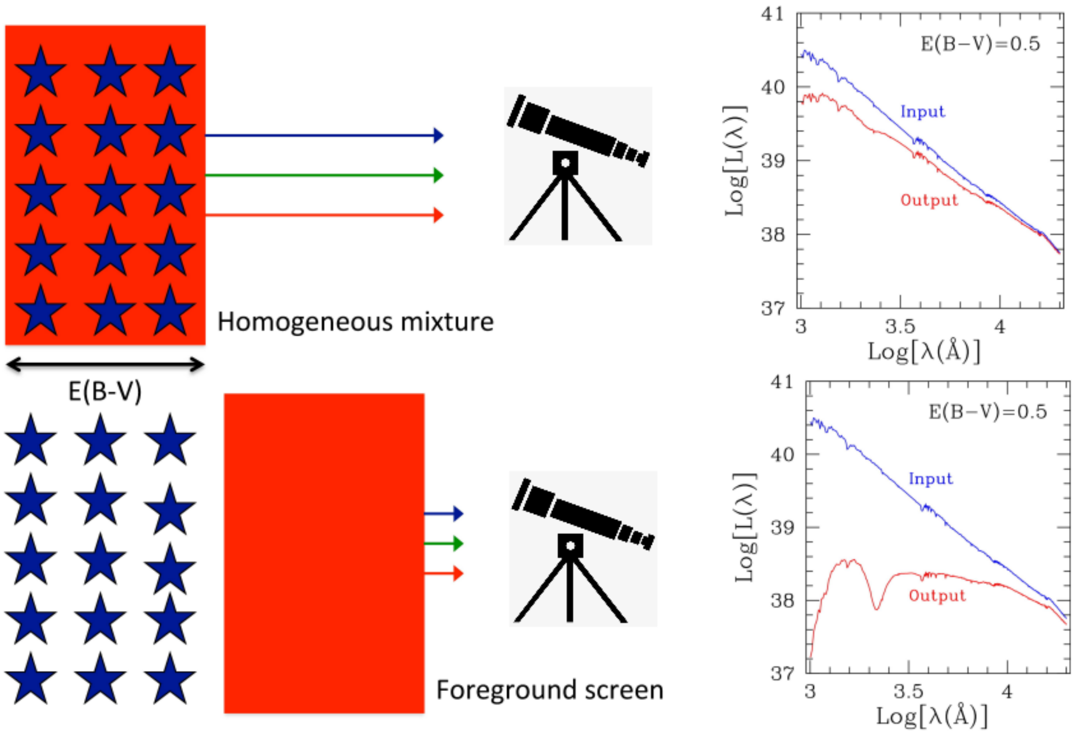

Figure 1.5: The top panel shows a homogeneous mixture of dust and stars, while in the bottom panel the dust is in a foreground screen and not mixed with the stars. The right panels show the input and output stellar SEDs, assuming the Milky Way extinction curve. We see that the input is the same for both cases, but the different geometric relation between the stars and the dust considerably affects the output spectrum. Sketch from Calzetti, 2013.

As we have hinted before, hydrogen recombination lines can be used to derive both the dust extinction and its geometry. In order to obtain these lines from external galaxies and determine their dust content, very high spatial resolution observations are needed in multiple bands of the electromagnetic spectrum. Theoretical calculations of the intrinsic ratios of the recombination lines are easy to obtain. Plus, under broad differences in chemical and physical conditions, these ratios barely change. By observing two hydrogen lines we can obtain a rough determination of the foreground extinction, while we need at least three lines to constrain both extinction and geometry (Liu *et al.*, 2013).

1.5 Motivation for this Work

Recent multi-wavelength extragalactic surveys both on the ground and in space (e.g., CANDELS/3D- HST, Grogin *et al.*, 2011; Koekemoer *et al.*, 2011; Skelton *et al.*, 2014; UltraVISTA, McCracken *et al.*, 2012; Muzzin *et al.*, 2013; UKIDSS, Lawrence *et al.*, 2007), have allowed us to closer examine the processes in many thousands of stellar-mass-selected galaxies back to when the Universe was only 1.5 Gyr. Well sampled photometry of these objects enables us to robustly model their spectral energy distributions (SEDs) and thus estimate their redshifts and study the properties of their stellar population (e.g. stellar mass, star formation rate, extinction, stellar age) over a wide range of redshifts. We can then study how these galaxies form, evolve and interact across cosmic time. However, it is important to remember that, as with any modelling, the SED fitting approach relies on a number of assumptions (e.g., the initial mass function, the dust geometry and extinction law, star formation history) which are often overly simplified and surprisingly poorly constrained, even at low redshift.

To derive the intrinsic properties of a galaxy, one must have an in-depth understanding of the dust content of the sources, since it modifies the galaxies' inherent SEDs in a wavelength-dependent way, in terms of both extinction and reddening. The most commonly used dust obscuration prescription is the local starburst "attenuation" curve (e.g., Calzetti *et al.*, 2000). As we look back in time, the conditions we observe and measure in galaxies change (SFR, metallicity, dust content, etc.), and it remains unknown whether this attenuation curve is valid for high-redshift galaxies or the variations in these properties make it also dependent on redshift.

Recent works show larger amount of dust obscuration with increasing redshift among the most massive galaxies (log$M/M_{\odot} > 10.5$; Brammer *et al.*, 2009; Marchesini *et al.*, 2014; Spitler *et al.*, 2014). The detection of many of these objects in the MIPS 24 μm band implies that they have $L_{IR} > 10^{11} L_{\odot}$, typical of luminous and ultra-luminous infrared galaxies (LIRGs or ULIRGs; Sanders and

Mirabel, 1996). At z<1, this population of galaxies seems to have generally diminished. The major complication to comprehend these systems is that at high-redshift they might be multiple unresolved objects in the process of merging, as well as how little we know about the dust distribution in them, leading to oversimplified assumptions of their dust modelling.

Understanding the dust distribution in local LIRGs and ULIRGs is imperative to further our comprehension of the population of massive galaxies at the peak of star formation (z$\sim$2, Madau and Dickinson, 2014). Instruments such as WFC3 onboard of the HST allow us to closely examine this by obtaining Hα and Paβ extinction maps. Although separated by billions of years of evolution, these local highly luminous objects are not too dissimilar to very distant massive dusty galaxies, both in their luminosity and amounts of dust extinction. Therefore, the high spatial resolution images and high signal-to-noise-ratio (S/N) of these local systems can prove beneficial in aiding our closer examination of the distant Universe. The Hα/Paβ decrement technique has been demonstrated for local-group HII regions (Pang *et al.*, 2011; De Marchi and Panagia, 2014) and for a portion of the nearby starburst M83 (Liu *et al.*, 2013); however, surprisingly, it has not yet been used for systematic study of the extinction properties of local galaxies.

Observations

2

2.1 The Hubble Space Telescope

The Hubble Space Telescope (HST) is the first major optical telescope to be placed in space. Hubble launched in April 1990 (Figure 2.1 shows the telescope in orbit). After 30 years of operations, our view of the Universe and knowledge about our place within it has grown immensely.

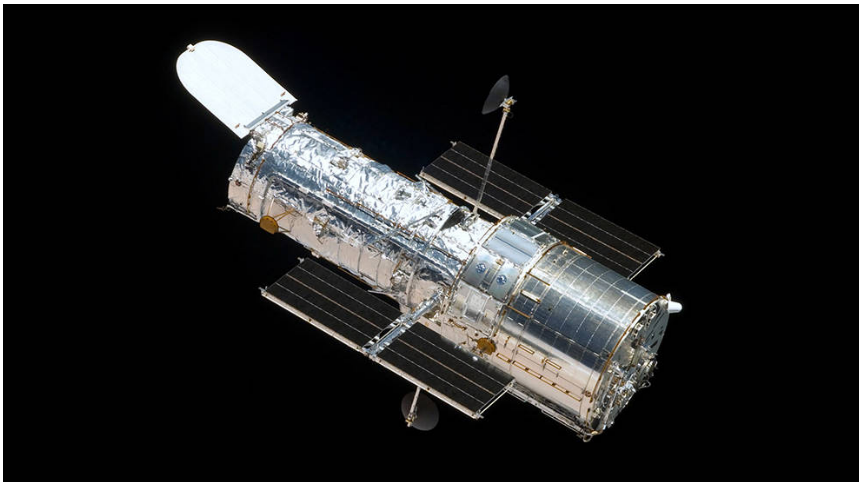

Figure 2.1: This photograph of NASA's Hubble Space Telescope was taken on the fifth servicing mission to the observatory in 2009. Credits: NASA.

The HST has a 2.4-meter primary mirror, and its four main instruments allow it to observe in the ultraviolet, visible and near infrared parts of the spectrum. Being in space allows it to not be subject to atmospheric absorption in the near-IR and obtain extremely high-resolution images.

Hubble's characteristics make it the perfect observatory to conduct our study. The emission lines that we are targeting, Hα and Paβ, fall in the optical and near infrared regions of the electromagnetic spectrum, so they are visible by HST. In particular, our observations use Hubble's Wide Field Camera 3 (WFC3) UVIS and IR imaging filters. We also use archival continuum imaging obtained with the Advanced Camera for Surveys Wide Field Camera (ACS WFC). As an example, Figure 2.2 shows the transmission curves as a function of wavelength for some of the HST filters used in this study. We also overplot a normalised EAZY SED galaxy template (see section 3.5.2) at redshift z=0.03 (same as one of our galaxies, as an example), to show where the Hα and Paβ lines fall within the filters. We observe that at redshift 0.03, we would capture Hα and Paβ (indicated in the plot) with the filters F673N and F132N, respectively, which appear coloured to highlight them.

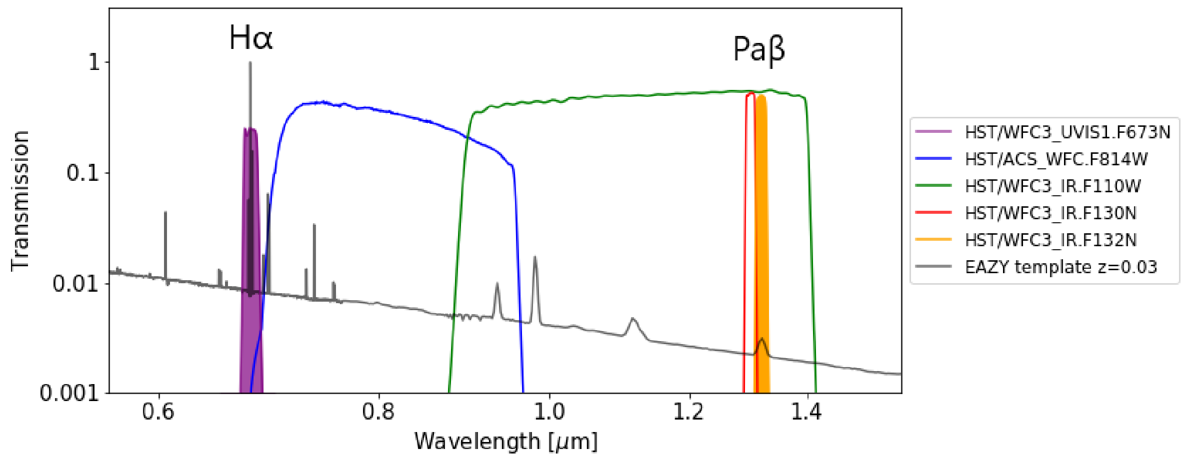

Figure 2.2: Plot of the transmission of some of the HST filters that we use to observe our emission lines at different wavelengths. The filter transmission curves are taken from the SVO Filter Profile Service (Rodrigo *et al.*, 2012). The solid grey line corresponds to the normalised SED of an EAZY galaxy template redshifted to emulate one of our galaxies at z=0.03. The position of the Hα and Paβ emission lines are indicated.

2.2 Dusty Cosmos Survey

Our galaxies have been imaged in multiple narrow-bands targeting hydrogen recombination lines (Hα in the optical and Paβ in the near-IR), which enables an unprecedented detailed study of the dust extinction in the nebular gas of nearby galaxies.

Calibrating the Dusty Cosmos is an HST snapshot survey program that was conducted in HST Cycle 23 (HST-14095, PI: Gabriel Brammer). The observations focus on a sample of 53 local galaxies, some of them from the GOALS survey plus targets that already had ACS Hα in the archive. The narrow-band filters included those that fall into the Hα (λ6563Å, depending on the redshift can be F673N, F665N or FR656N) and Paβ (λ12818Å, F128N, F130N or F132N) emission lines wavelength ranges.

The GOALS sample

The Great Observatories All-Sky LIRG Survey (GOALS; Armus *et al.*, 2009) offered the perfect local sample to conduct our study: IR-luminous galaxies at z$\sim$0.02 with a broad array of archival HST, Spitzer, and additional ancillary data. For a typical GOALS galaxy that had only broad-band ACS or WFC3 imaging, we observed both narrow-band Hα with WFC3/UVIS and Paβ with WFC3/IR. We also obtained short WFC3/IR F110W images to facilitate continuum removal from the Paβ images (with archival ACS images used for Hα). Figure 2.3 shows an overview of the GOALS Hα/Paβ sample.

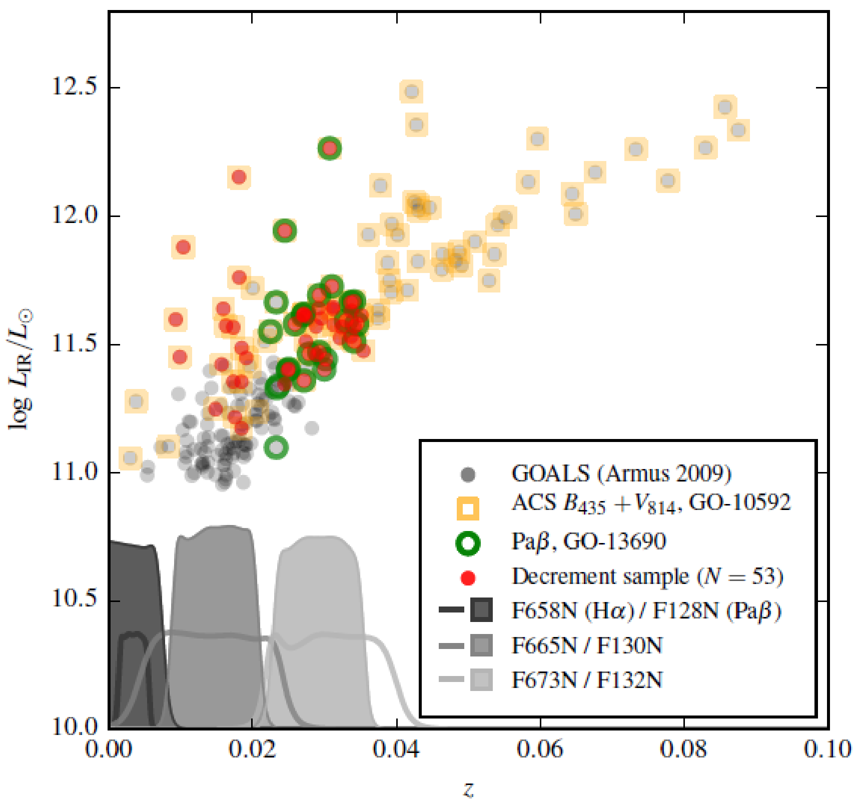

Figure 2.3: Overview of the GOALS Hα/Paβ sample. The LIRGs are uniformly observed with ACS F435W and F814W (GO-10592, yellow points). We select the sub-sample of GOALS galaxies with ACS broad-band imaging and redshifts that put the hydrogen recombination lines in the F665N/F130N and F673N/F132N filter pairs (red points). We will add Hα imaging to the sub-sample of GOALS galaxies already observed in Paβ by GO-13690. Plot from the HST proposal HST-14095, PI: Gabriel Brammer (Brammer, internal communication).

Processed Data

The fully-processed images for our sample of 53 nearby star-forming galaxies can be found on `http://cosmos.phy.tufts.edu/dustycosmos/`. The images were processed by Varun Bajaj, Research Assistant at STScI (Space Telescope Science Institute). Varun Bajaj and Daniel Lange-Vagle, from Tufts University, put together the website with the results.

Each target has at least both hydrogen recombination lines - Hα and Paβ - as well as the local continuum for each line. Each image was processed/created using the DrizzlePac package, the publicly available software from STScI for aligning and combining HST images. The package TweakReg was used for alignment, plus to combine data from additional visits, and once the full set of images of a target were properly aligned, the package AstroDrizzle was used for stacking them into final mosaics for each filter. Where available, the images were aligned to the Hubble Source Catalog to provide an absolute astrometric reference.

The original pixel size of the mosaics obtained with the WFC3 IR channel is 0.13 arcsec/pixel. The pixels are then resampled (drizzled) to 0.1" in the IR mosaics (0.05" pixels for ACS/WFC and $\sim$0.04" for WFC3/UVIS). The conversion to physical size per resolution element is a function of redshift. Our sample spans redshifts from 0.0001 to 0.035, with the median being $\sim$0.02. This translates to a physical size of 0.3 pc/pixel for the closest galaxy and 70 pc/pixel for the farthest[1] . For the median redshift of the sample we obtain a physical size of $\sim$40 pc/pixel.

Figure 2.4 shows the resulting sample of 53 nearby star-forming galaxies. The whole sample is also summarised in Tables 2.1 and 2.2. Table 2.1 contains the LIRGs that are in the GOALS survey (Armus *et al.*, 2009), whereas Table 2.2 includes the rest of galaxies from our Dusty Cosmos observations that are not in that survey. The tables show the coordinates and redshifts of all galaxies. For all the GOALS galaxies the infrared luminosity is available. For the rest of the targets, we obtain some infrared luminosities from the KINGFISH survey (Kennicutt *et al.*, 2011).

[1]WMAP9 cosmology (Hinshaw *et al.*, 2013) assumed: $H_0 = 69.32$ km s^{-1} Mpc^{-1}, Ω_M=0.287, Ω_Λ=0.712.

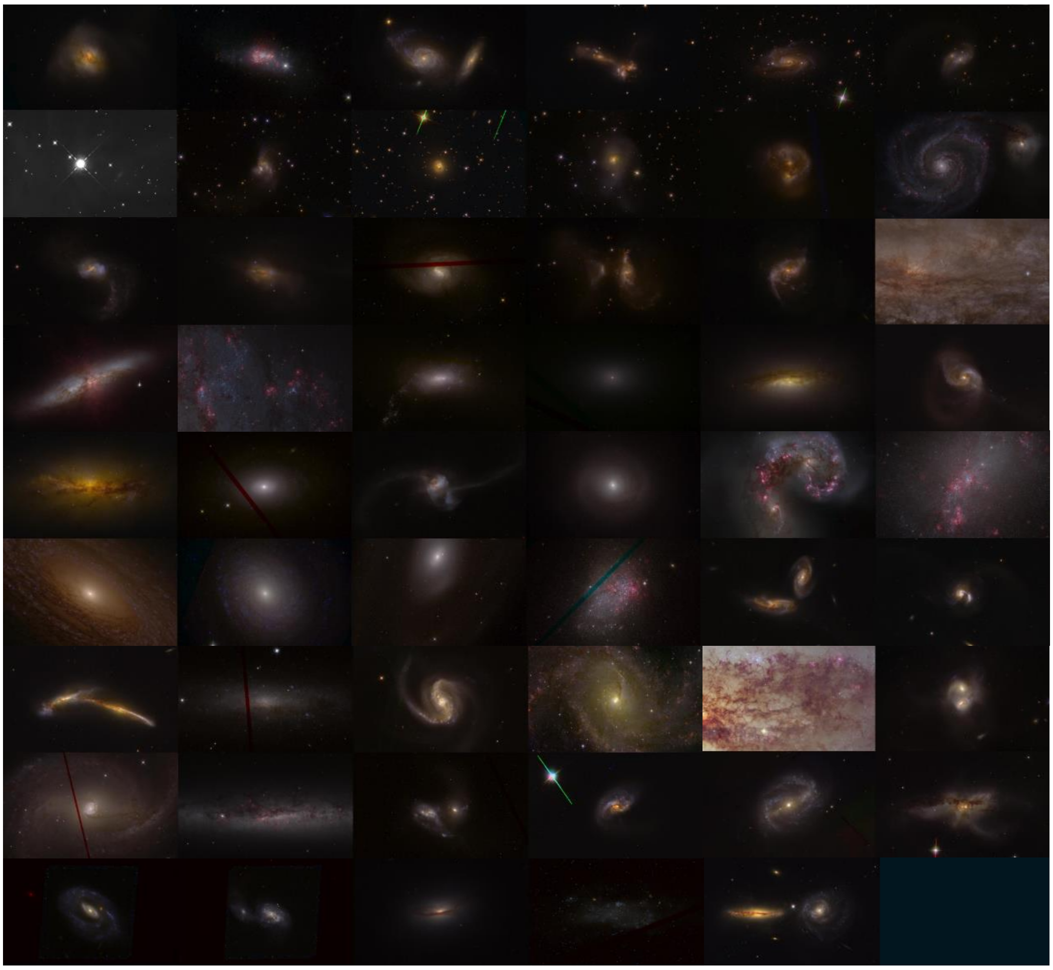

Figure 2.4: Snapshot of the sample from the Dusty Cosmos Survey.

Name	RA	DEC	z	$\log(L_{IR}/L_{\odot})$
ESO550-IG025	65.33333	-18.81333	0.0322	11.5
IRAS03582+6012	60.63374	60.34383	0.030453	11.4
IRAS05223+1908	81.31875	19.17944	0.029577	11.6
IRAS08355-4944	129.25761	-49.90841	0.026279	11.6
IRAS12116-5615	129.25761	-49.90841	0.027460	11.6
IRAS13120-5453	198.77660	-55.15628	0.031227	12.3
IRAS18090+0130	272.91010	1.52771	0.028923	11.6
IRAS23436+5257	356.52380	53.23235	0.034712	11.5
IRASF10038-3338	151.51938	-33.88503	0.0342	11.7
IRASF16164-0746	244.799	-7.90081	None	11.6
IRASF16399-0937	250.66709	-9.7205	None	11.6
MCG-02-01-051	4.71208	-10.376803	0.027	11.4
MCG+12-02-001	13.51643	73.084786	0.015812	11.4
NGC1614	68.50011	-8.57905	0.015851	11.6
NGC2146	94.65713	78.35702	0.002973	11.1
NGC2623	129.60039	25.75464	0.01847	11.5
NGC5256	204.57417	48.27806	0.02737	11.5

Name	RA	DEC	z	$\log(L_{IR}/L_{\odot})$
NGC5331	208.06729	2.10092	0.033043	11.6
NGC6090	242.91792	52.45583	0.029434	11.5
NGC6240	253.24525	2.40099	0.024323	11.9
NGC6670	278.3975	59.88881	0.028807	11.6
NGC6786	287.7247	73.41006	0.025	11.4
NGC7592	349.59167	-4.41583	0.02441	11.3
VV340A	224.25127	24.606853	0.03275	11.7

Table 2.1: Table summarising the Dusty Cosmos LIRGs that are in the GOALS survey (Armus *et al.*, 2009).

Name	RA	DEC	z	$\log(L_{IR}/L_{\odot})$
ARP220	233.7375	23.5031	0.018126	-
ESO338-IG004	291.99308	-41.57523	0.009480	-
M51	202.46958	47.19526	0.00155	-
M82	148.96846	69.67970	0.00073	-
M83	204.25383	-29.86576	0.001732	-
MCG+00-29-023	170.30109	-2.984167	0.0247	-
NGC0253	11.88806	-25.2888	0.000863	-
NGC1140	43.63976	-10.0285	0.004999	-
NGC1396	54.52743	-35.43992	0.002945	-
NGC1482	58.6622	-20.50245	0.006331	10.6
NGC2551	126.20956	73.41200	0.007739	-
NGC2681	133.38641	51.31371	0.00225	-
NGC2841	140.51106	50.97648	0.0019	10.1
NGC2985	147.59264	72.27865	0.004306	-
NGC3358	160.88763	-36.41071	0.010067	-
NGC3738	173.95085	54.52373	0.00072	-
NGC4038	180.47084	-18.86759	0.005589	-
NGC4214	183.91323	36.32689	0.000977	-
NGC5128	201.36506	-43.01911	0.001825	-
NGC6217	248.16340	78.19821	0.004556	-
NGC6690	278.70935	70.52389	0.001631	-
NGC6946	308.718	60.1539	0.000133	10.9
NGC6951	309.30865	66.10564	0.00475	-
NGC7090	324.12027	-54.55732	0.002837	-
PGC4798	20.01106	14.36153	0.0312	-
SDSS-J110501.98+594103.5	166.25825	59.68431	0.0338	-
SDSS-J172823.84+573243.4	262.09933	57.54539	0.029	-
SDSS220141.64+115124.3	330.4235	11.85675	0.0296	-
UGC5626	156.11644	57.39251	0.008469	-

Table 2.2: Table summarising the Dusty Cosmos nearby star-forming galaxies which are not in the GOALS survey. The infrared luminosity values (L_{IR}) are obtained from the KINGFISH survey (Kennicutt *et al.*, 2011).

3 Methodology

In this chapter we explain in detail the different methods and analysis approaches that we have followed with our sample of nearby galaxies to reach our goal of obtaining high-resolution extinction maps.

The starting point of this thesis is the data from `http://cosmos.phy.tufts.edu/dustycosmos/`. The images are already fully processed, aligned and stacked, so they are ready for the analysis.

Parallel to our work in Copenhagen, a group from Tufts University in Boston has also been working with this data to obtain physical parameters with the SED-fitting code `Prospector` (Johnson and Leja, 2017; Leja *et al.*, 2017). In this section we also elaborate on this method and our own "competing" approach, which consists in using EAZY (Brammer *et al.*, 2008) for SED-fitting.

3.1 Voronoi Binning

Modern instruments allow us to spatially resolve nearby extended sources. However, these observations can display a significant anisotropy in the signal-to-noise-ratio (S/N) across the target. Sometimes these variations differ by orders-of-magnitude, and some pixels often have poor S/N. To resolve this, the spatial elements can be grouped locally to improve the S/N across the image, however this results in a loss of spatial resolution.

Binning and smoothing are the two types of averaging methods available. Binning consists of grouping together data points that are in close proximity to each other and taking the average of their parameters. The resulting data has fewer points, but a more uniform S/N than the original. Alternatively, smoothing keeps the number of original data points, while enhancing the local

S/N. This is achieved by correlating nearby data points so that the amount of independent measurements is reduced. Binning is more appropriate when a robust treatment of uncertainties is required or when limiting the number of data points is important (for example to make computations feasible), which is the case for our study.

As mentioned before, in the case of an extended galaxy, the S/N can vary significantly from the outskirts towards the centre of the source. Disk galaxies typically have "exponential" surface brightness profiles (Boroson, 1981), thus the outskirts are much fainter than the centres. With this in mind, we should implement an adaptive binning scheme: for lower S/N, larger bins are created, whereas for high S/N regions, the bins will be smaller and a high resolution is maintained.

The first step of this work has been to develop a binning procedure to generate spatial bins with roughly constant S/N using an adaptation of the Voronoi binning method by Cappellari and Copin, 2003. This method implements adaptive spatial binning of integral-field spectroscopic (IFS) data to achieve a specified constant signal-to-noise ratio per bin. A secondary reason to perform the binning is to be able to run `Prospector` in a time-saving manner, by reducing the number of original data points in which it has to fit SEDs. Results of the binning for a galaxy from our survey can be seen in Figure 3.1.

Cappellari and Copin use the Voronoi Tessellation to generate bins with optimal 2D tessellations while satisfying topological, morphological and uniformity requirements of the binning scheme. A 1D-binning algorithm would work as follows: the binning starts from the unbinned pixel with highest S/N, generating a first bin there and accreting to the adjacent pixels. When a chosen S/N is reached, that bin is complete, and a new bin is started. This process is repeated until all original pixels have been binned. To learn in detail how this idea is extended to 2D, see Cappellari and Copin, 2003.

Cappellari's Voronoi algorithm is inefficient for handling datasets with millions of data points as in the case for the large image mosaics used here. Furthermore, the algorithm is not robust in the regime of low S/N per original data point (Cappellari and Copin, 2003), as in the outskirts of the galaxies in our Hubble images. For these reasons, we adopt a hybrid approach of

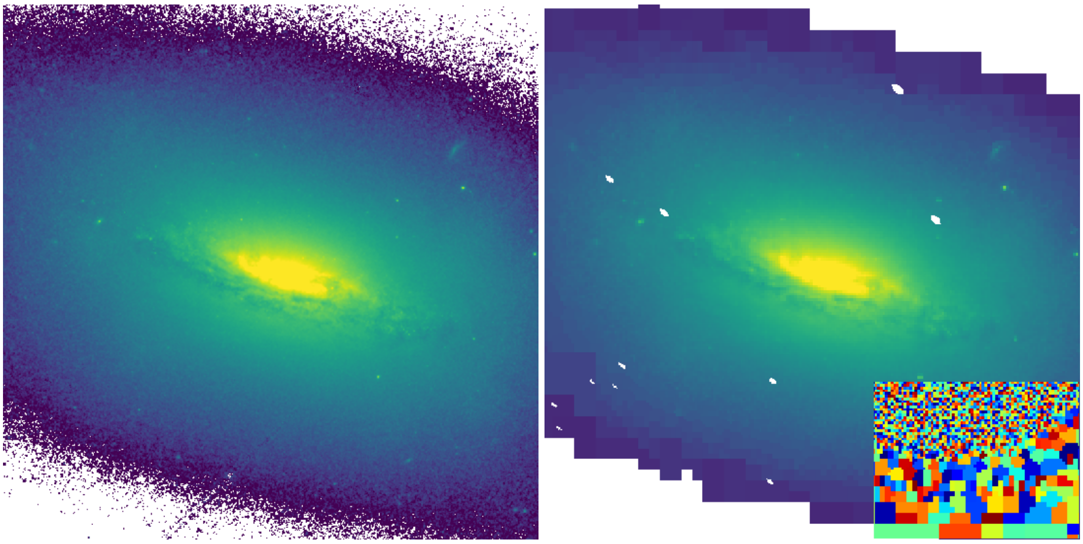

Figure 3.1: Example of our binning algorithm on the NGC1482 image obtained with the F110W filter. On the left we have the original image and on the right the binned one. The minimum size of a bin here is 4 pixels across, which is equivalent to 0.4 arcsec and a physical scale of 53 pc. The white "holes" correspond to masked pixels in the mosaic generally not covered by the input exposures for various reasons. On the right binned image, we can see that the outskirts of the galaxy contain larger bins in order to reach the specified constant signal-to-noise ratio per bin. On the bottom right we overlay a different colouring scheme to highlight this even more and separate adjacent bins using random colours.

block-averaging the galaxy mosaics in progressively-shrinking box sizes and applying the Voronoi algorithm on the blocked image.

Our adaptation of this binning procedure will thus start by defining a reference image that will be used in the binning. We usually use F110W since it generally has the highest S/N of all bands, mainly because the filter is extremely broad. The code creates a block averaged image, where each block has 32×32 original pixels. We mask any pixels where these large bins have S/N less than a minimum threshold, which is one of our binning parameters. Then, we run Cappellari's optimal Voronoi 2D-binning algorithm on this large blocked image. We adopt as a Voronoi bin anything with more than one individual (blocked) pixel (N>1), and these pixels are now "frozen" in the binning. Individual pixels that satisfy the target S/N (i.e., N=1 blocked bins) are sent to the next step, which consists in reducing the block size by a factor of two (e.g., 16×16 at the second stage). Pixels in blocks where there is not enough S/N to reach the target S/N, and therefore the Voronoi code bins multiple blocks together, are not sent to the next step and remain in that assigned Voronoi bin. The code repeats these steps until the desired minimum bin size is achieved (e.g., if the minimum possible size is wanted, it will stop when it reaches 1×1, i.e., native pixels). For our study we stop at 4×4 pixels as the minimum size of a bin, reducing the number of points to be able to run `Prospector`, but at the same time not losing drastically the high resolution in our images. For example, for a 4×4 pixels bin, which would be 0.4" across, we still achieve a resolution of 160 pc at $z \sim 0.02$.

Once we create the F110W binned image, we apply the binning derived from F110W to the other images obtained with different filters on the same galaxy. However, this means that for some bins the target S/N criteria will not necessarily be met in all bands, which could later on affect the robustness of the derived physical parameters in that bin. Nonetheless, it is important to have the same binning in all images to be able to perform different studies on them.

Figure 3.2 shows the S/N of the images from Figure 3.1, before and after the binning. Figure 3.3 shows a scatter plot of the S/N of the resulting binned pixels. We can see in both figures that, after the binning, all bins reach a target S/N that we impose in our code, which is S/N=50. We can also see that the S/N is considerably smoother across the image after the binning. Except for the central region, where individual pixels satisfy the target S/N criteria and there is a peak in the S/N, the outskirts show a noticeably uniform distribution in the S/N.

The Voronoi binning code from Cappellari and Copin, 2003, can be found here `https://www-astro.physics.ox.ac.uk/~mxc/software/`. Our adaptation of this scheme for bigger images can be found here `https://github.com/claragimenez/voronoi`.

3.2 Continuum Subtraction

Once we have applied the binning method, the next step is to obtain emission-line images. To target spectral lines, as we have explained before, we use narrow-band filters from HST. Despite being appropriate for isolating light

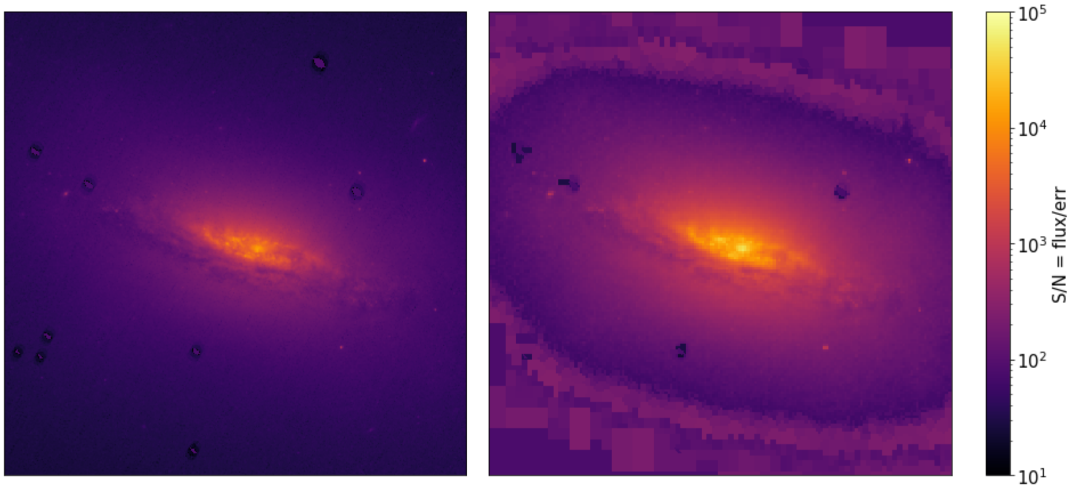

Figure 3.2: Comparison of the S/N in NGC1482 F110W image before (left) and (right) after binning. We can see that for the binned image the S/N is much smoother and uniform across the image, as opposed to the big gradient in the unbinned image, when going from the outer parts to the centre of the galaxy. We can also notice that no bins have S/N<50 (our target S/N) in the binned image, which was not the case for the original.

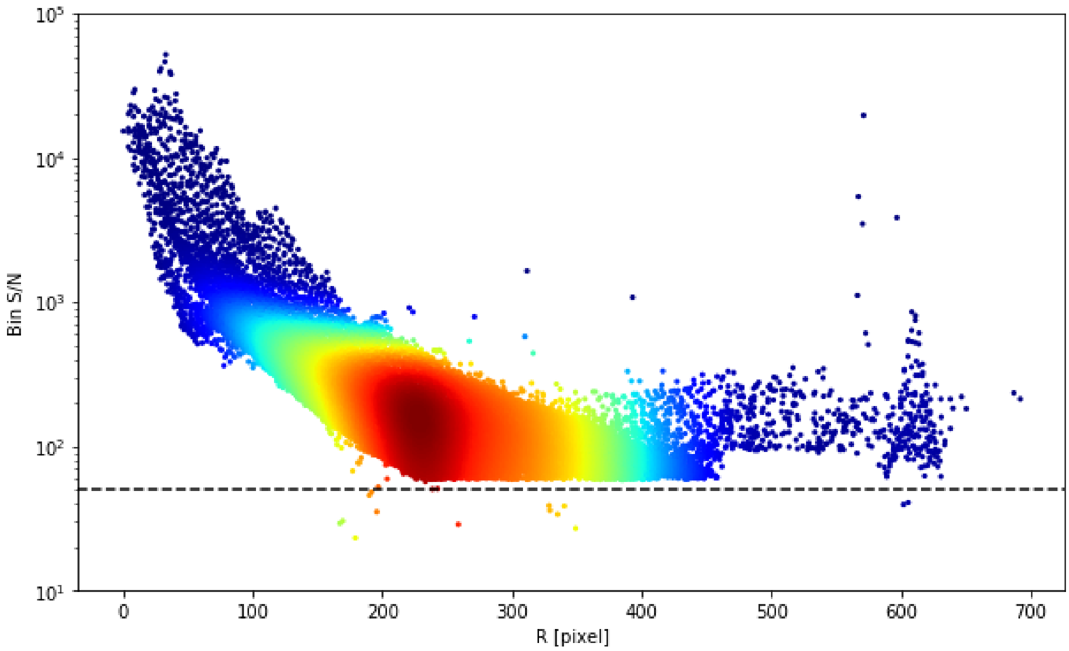

Figure 3.3: Scatter plot of the bin S/N as a function of the distance to the centre of the galaxy (R, in pixels). We can observe that, except the central region that has very high S/N, the outskirts have a very uniform S/N around ~100, and even the farthest bins have more than S/N=50 (dashed black line), which is the target S/N that we impose in our algorithm.

from emission lines, a narrow-band filter will still measure flux that will be a combination of the emission from the continuum and the spectral lines.

To produce pure hydrogen emission line images, we remove the stellar continuum by subtracting broad-band filters from the respective narrow-band filters. For Hα, we usually employ F814W images to remove the continuum. For Paβ, the narrow-band line image is accompanied by the very broad F110W, which we use for subtracting the continuum. From our sample, 26 of the targets have paired close narrow-band images. For these targets, we subtract one narrow-band from the other to obtain the emission line image.

First, we start by using PySynphot (STScI Development Team, 2013) to compute flux calibration factors that convert instrumental count rates (electrons per second) to physical flux. PySynphot simulates photometric data and spectra as they are observed with HST using comprehensive instrumental sensitivity calibrations such as detector quantum efficiency and filter bandpasses. This conversion is implemented in the continuum subtraction scheme explained below, so that our resulting line images will have units of flux (in particular, erg/s/cm^2). This should improve the conversion to flux densities that we would obtain using the PHOTFLAM or PHOTFNU values from the image headers, which are derived with a specific assumption of the underlying spectral shape across the filter bandpass.

Pysynphot allows us to implement different continuum shapes in order to scale it across various broad-band filters. We could enforce, for example, a flat spectrum for the continuum using `pysynphot.FlatSpectrum()`. A less basic continuum shape would be a spectrum with a slope. For a slope = 0 we would recover our flat spectrum, but a slope of 1 would mean a red tilt, increasing towards longer wavelengths. What we end up applying is a galaxy model to scale the continuum shape. We use one of EAZY's galaxy templates, `'alf_SSP.dat'`, which is a characteristic SED of an early-type galaxy. This template was modelled after the spectrum described in Conroy *et al.*, 2014. Such a population might be appropriate, e.g., for the (un-reddened) evolved stars in the central spheroid (bulge) components of our galaxies. This template contains some absorption at the location of Hα. The template will not necessarily have the correct tilt for the different continuum shapes of all galaxies in our study, but it is considerably more appropriate than using a flat spectrum, in particular because it accounts for that small absorption effect. We model the line emission with a Gaussian profile using `pysynphot.GaussianSource()`, to calculate emission-line calibration factors, and the calibration does not depend on the assumed line width.

Once we have our flux calibration factors and our line and continuum models, we can subtract the continuum from the line and obtain a continuum-subtracted, flux-calibrated, emission-line image. We additionally calculate the propagated error of the subtraction. Some results of the basic empirical subtraction $line - continuum$ (taking into account calibration factors and models) can be seen in Figure 3.4.

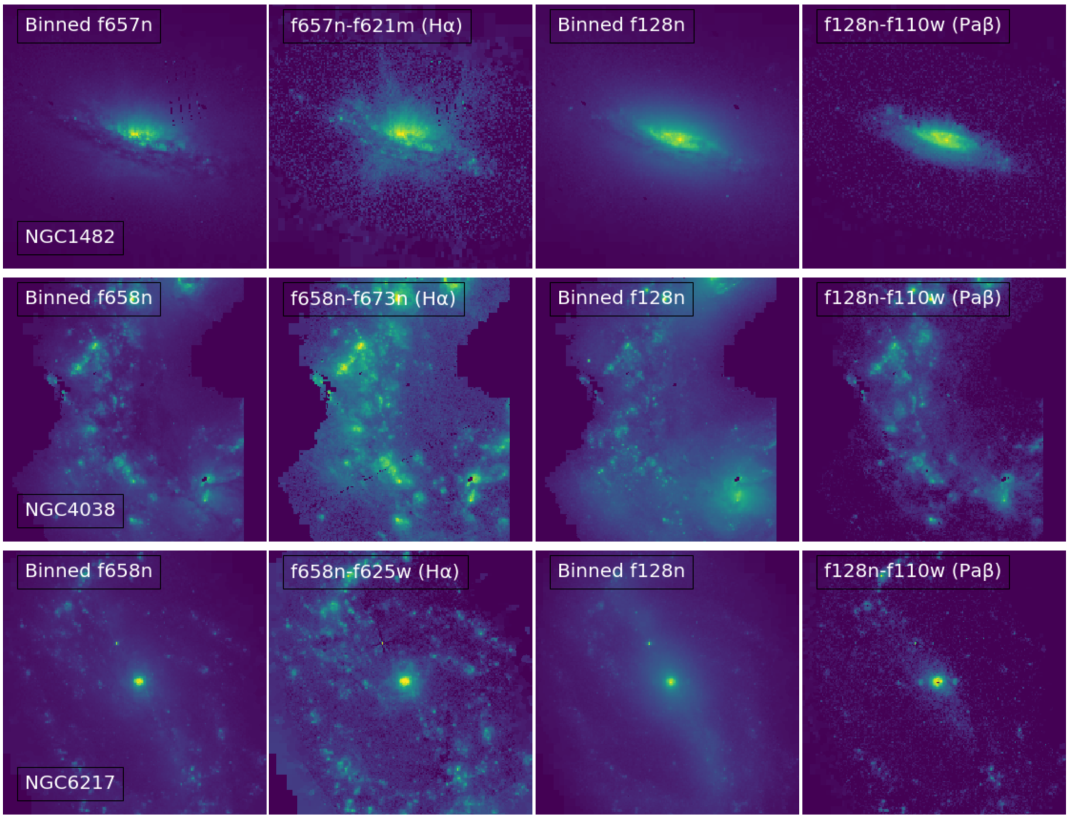

Figure 3.4: Continuum-subtracted, flux-calibrated, emission-line images of three galaxies from our Dusty Cosmos survey. The narrow- and broad-band filters used in the subtractions to obtain emission-line images are displayed for each galaxy.

With the binned images we can also produce colour Red-Green-Blue (RGB) images. An RGB image can be thought of as a MxNx3 array, where M and N are y and x of the image respectively and the length-3 layer represents the different colours.

The visualization tools from Astropy (Astropy Collaboration *et al.*, 2018; Astropy Collaboration *et al.*, 2013) can be used to change the stretch and scaling of the individual layers of the RGB image. Lupton *et al.*, 2004, describes an 'optimal' algorithm for producing red-green-blue composite images from three separate high-dynamic range arrays. This method is implemented in `astropy.visualization.make_lupton_rgb` and requires that the three images are aligned and have the same pixel scale and size. By using our binned broad-band images from the blue, green and red parts of the spectrum, we obtain RGB images such as the ones in Figure 3.5.

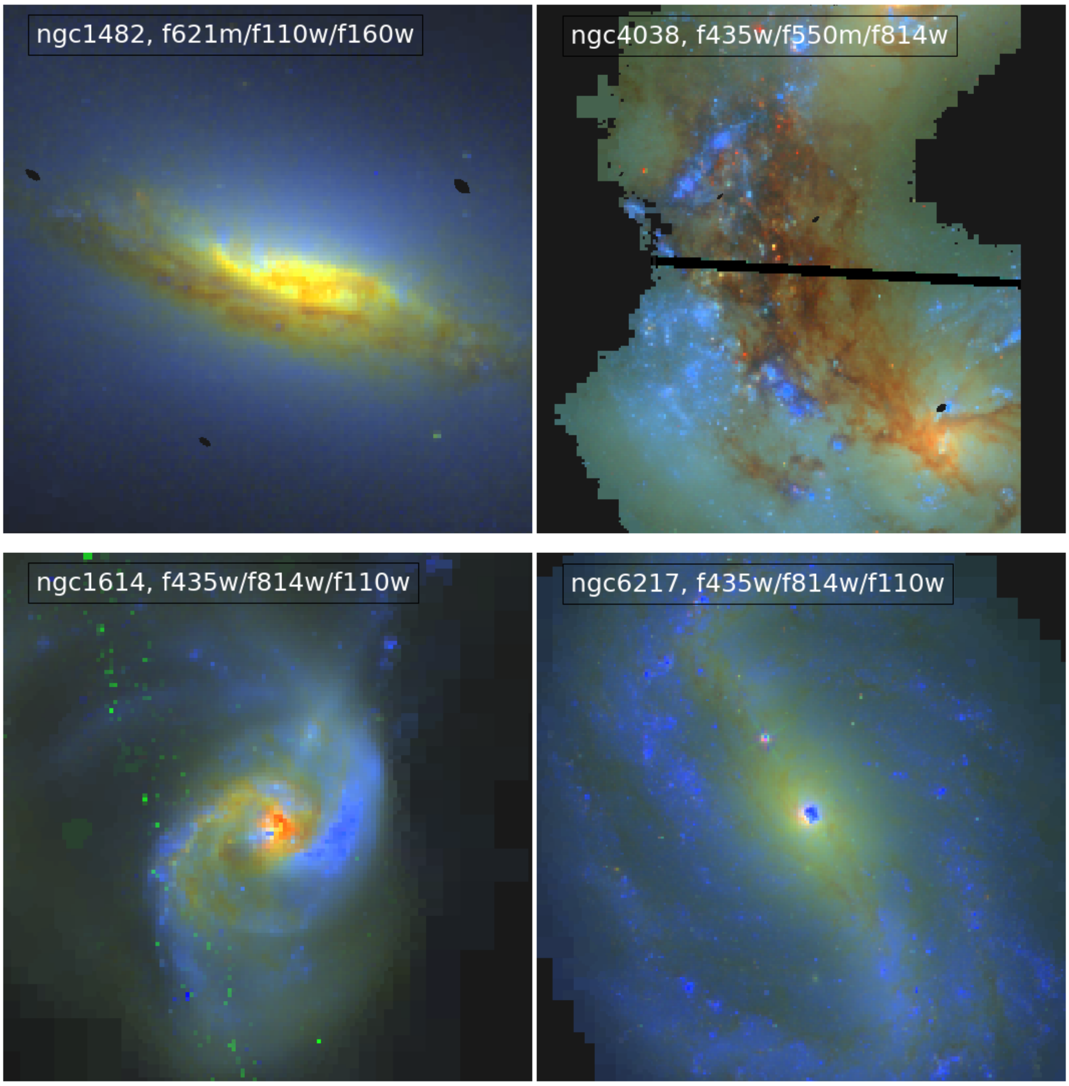

Figure 3.5: RGB images for different galaxies from our Dusty Cosmos sample. The name of the galaxy, as well as the blue, green and red filters used to build the RGB image, are displayed for each panel.

3.3 Extinction Maps Hα/Paβ

As we have seen in the introductory chapter, particularly in section 1.4, hydrogen recombination lines can be used to derive both the dust extinction and geometry. The most common pair of recombination lines used for this purpose is the Balmer decrement, Hα/Hβ, so why do we study Hα/Paβ instead? The

GOALS LIRGs (and their high-z counterparts) often have significant reddening/extinction with $A_V > 2$ mag over a large fraction of the visible extent of the galaxies. Liu *et al.*, 2013, show that Paβ is much more effective than the Balmer lines for probing large optical depths, with A_V values determined from Hα/Paβ larger than those derived from the optical Balmer lines alone by $\gtrsim$1 mag. In the case of the Calzetti reddening curve, we can calculate the A_V value at which the observed fluxes of different recombination lines become equivalent. We will obtain f(Hα)=f(Paβ) at A_V=4.7 mag, whereas we achieve f(Hβ)=f(Paβ) at A_V=1.8 mag. This implies that the ratios between redder lines (e.g. Hα/Paβ) allow us to probe larger optical depths than bluer lines such as the Balmer decrement.

The intrinsic ratios of the Hydrogen recombination lines show relatively little variation across a broad range of physical conditions of the ionised gas. As shown in Liu *et al.*, 2013, assuming Case B recombination, with changes in the temperature between 5×10^3 and 10^4 K and in the electron density of an HII region between 10^2 and 10^4 cm^{-3}, the Hα/Paβ line ratio only changes between 16.5 and 17.6 ($\sim$7%, Osterbrock, 1989). For our galaxies we adopt an electron density n_e=10^3 cm^{-3} and temperature T_e=7500 K, resulting in an intrinsic ratio (Hα/Paβ)$_{int}$=17.56 (Osterbrock, 1989). Under the assumption of constant electron density and pressure, deviations measured from this intrinsic value can thus be directly associated to dust attenuation.

To create the extinction maps from the hydrogen recombination line ratios, we use our binned, continuum-subtracted emission line images. We simply calculate the ratio of Hα and Paβ and divide by the intrinsic ratio 17.56. We propagate the errors to track the corresponding uncertainties of the resulting extinction maps. Just as a matter of plotting, the output is better behaved if we plot Paβ/Hα instead of Hα/Paβ, but it represents the same quantity and will equally trace the dust extinction. Examples of our results can be seen in Figure 3.6. In the next chapter we will analyse and discuss these results.

3.3.1 Conversion to A_V

Once we have our extinction maps obtained with the hydrogen recombination lines, in the following chapter we want to compare these results with SED-fitting methods. With this purpose in mind, we need to convert the ratio

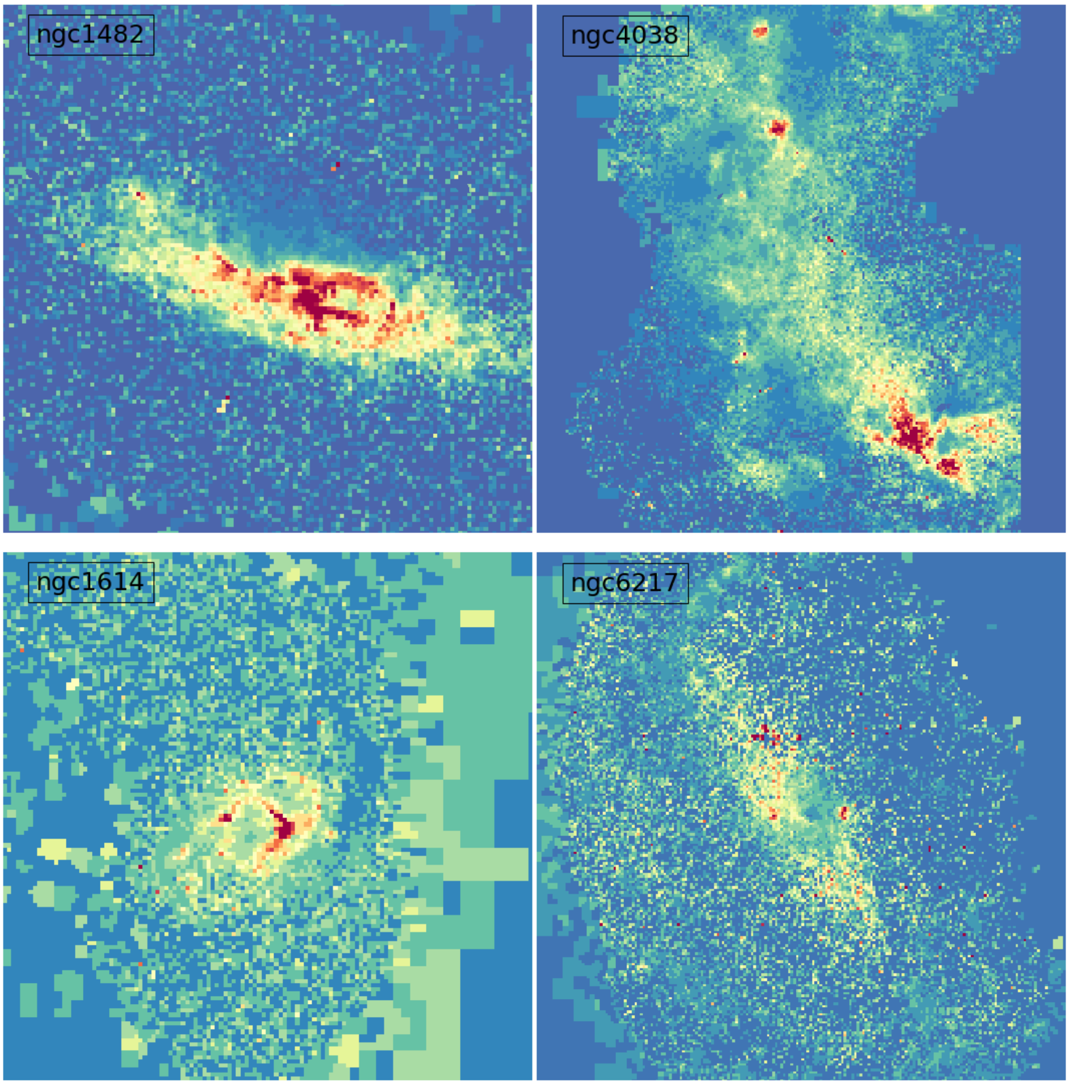

Figure 3.6: Extinction maps Paβ/Hα for four galaxies from our Dusty Cosmos sample. The RGB images of these galaxies are shown in Figure 3.5.

Hα/Paβ to visual extinction A_V, to compare with continuum A_V values that we obtain from the SED-fitting.

We need to assume dust attenuation curves to determine A_V from Hα/Paβ. We use the python package `dust_attenuation`, which provides models of interstellar dust attenuation curves. For our study, we will use the attenuation curve $k(\lambda)$ from Calzetti *et al.*, 2000, hereafter C00, which assumes a basic foreground dust screen geometry.

The ratio of dust attenuation to colour excess at a given wavelength is $R_\lambda = A_\lambda / E(B-V)$. C00 presents different values of R_V for various galactic components. For the measurements of the Hα/Paβ decrement, we select

R_V=3.1. Now we can obtain the dust attenuation in our galaxies with the emission line measurements Hα and Paβ alone. Hereafter we term $A_{V,gas}$ the A_V extinction derived from the line ratio, following Greener *et al.*, 2020, which assumes that the decrement will trace the attenuation in the gas content of the galaxy. To convert from the line ratio to visual extinction we thus use $A_{V,gas} = 3.1E(B-V)$.

We can define the colour excess $E(B-V)$ as the difference between the observed and intrinsic $(B-V)$ colour index:

$$E(B-V) = (B-V)_{obs} - (B-V)_{int} \tag{3.1}$$

This change is attributed to dust attenuation. We can express the colour excess in terms of the Hα/Paβ decrement (for details see, e.g., Momcheva *et al.*, 2013):

$$E(B-V) = \frac{E(\text{Pa}\beta - \text{H}\alpha)}{k(\text{Pa}\beta) - k(\text{H}\alpha)} = \frac{2.5}{k(\text{Pa}\beta) - k(\text{H}\alpha)} \log_{10}\left[\frac{(\text{H}\alpha/\text{Pa}\beta)_{obs}}{(\text{H}\alpha/\text{Pa}\beta)_{int}}\right] \tag{3.2}$$

where k(Paβ) and k(Hα) are the reddening curves evaluated at Paβ and Hα wavelengths, respectively. (Hα/Paβ)$_{obs}$ is the observed line ratio and (Hα/Paβ)$_{int}$ is the intrinsic ratio, which we choose to be 17.56, as explained before. E(Paβ–Hα) is akin to the colour excess $E(B-V)$, but defined at the wavelengths of Paβ and Hα instead of the blue and visible bands. Assuming a C00 reddening curve, we obtain k(Paβ)=1.27 and k(Hα)=3.33. The reddening curves are defined in rest-frame, so we do not calculate different values for each of our target's redshift.

In the next chapter, we will perform a comparison of the derived A_V measurements, both with the Hα/Paβ decrement and with full population synthesis models.

3.4 The *UVJ* Diagram

Part of what makes understanding galaxy evolution so challenging is the wealth of galaxy properties. Explaining the evolution of all these properties and the correlation between them is a daunting task. Two-colour diagrams have been shown to be a useful and simple mechanism for comprehending astronomical objects, in particular the *UVJ* diagram, which is obtained by plotting the rest-frame $U - V$ versus $V - J$ colours.

The *UVJ* diagram separates quiescent from star forming galaxies (SFGs). It is particularly useful due to its ability to break the degeneracy between age and reddening for red galaxies: in most cases, galaxies with blue UV colours display rather dust-free star formation activity, whereas galaxies can appear red due to dust obscuration or being quiescent, since evolved older stellar populations will dominate. On the other hand, quiescent galaxies unobscured by dust are blue in *VJ*, therefore they will be in a different position than the SFGs in the *UVJ* plane, leaving the two types of sources empirically set apart. Williams *et al.*, 2009, determined a border between the two regions that is still relevant and is being used in the present-day.

The distribution of quiescent galaxies and SFGs in the *UVJ* diagram is very distinct. While quiescent systems are located in a compact locus of *UVJ* colours, SFGs occupy a wide domain. This can be seen in Figure 3.7. Wuyts *et al.*, 2007, credited varying dust extinction as the reason for the broad distribution of SFGs in the *UVJ* colour space. This idea is shared by later works, finding that the reddening vector, computed assuming a reddening law from Calzetti *et al.*, 2000, suggests that by changing the quantity of dust extinction we can obtain a considerable range of SFGs colours (Patel *et al.*, 2011; Patel *et al.*, 2012).

As we have seen, besides separating quiescent from SFGs, the *UVJ* colours of a galaxy show close correlation with its specific star formation rate (sSFR, defined as the star formation rate divided by the stellar mass) and visual extinction (A_V) (Fang *et al.*, 2018). Since the location in the *UVJ* relates to direct continuum attenuation measurements, in this work we plot spatially resolved *UVJ* diagrams to further study the dust obscuration of our nearby galaxies.

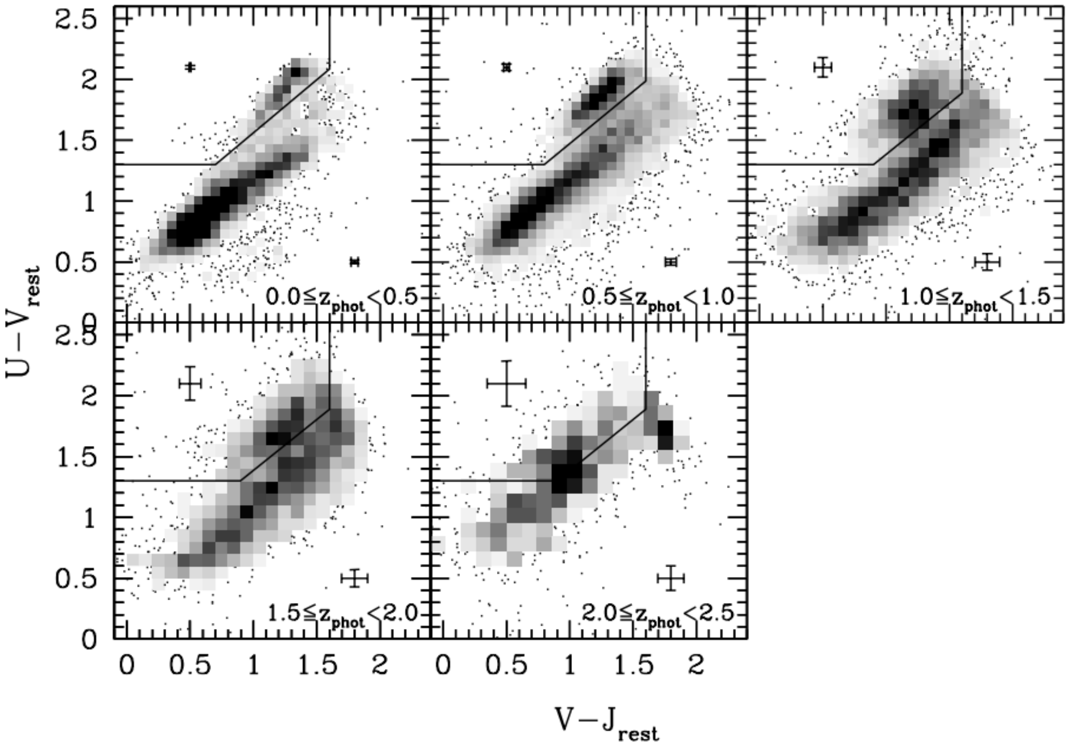

Figure 3.7: UVJ diagrams from Williams *et al.*, 2009, of UKIDSS Ultra–Deep Survey (UDS) $K < 22.4$ galaxies in five redshift bins. The solid lines show the adopted division between SFGs (broad distribution) and quiescent galaxies (compact sample, within the upper-left region) determined by Williams *et al.*, 2009.

To create a spatially resolved *UVJ* diagram we can follow two recipes. One way consists in obtaining continuum "colour" images without any SED modelling. We can derive effective *UVJ* colours from our measured fluxes with broad-band filters that fall within the U, V and J bands of the spectrum. We convert from fluxes to magnitudes/colours using the following:

$$U - V = -2.5 \log_{10}\left(\frac{f_U}{f_V}\right) \tag{3.3}$$

where f_U and f_V are the observed fluxes in the U and the V band, respectively. The other method is based in performing SED-fitting for each galaxy's bin and then calculate U, V and J magnitudes based on the best-fitting model spectrum. EAZY can perform this fitting and provide rest-frame U, V and J fluxes from which we can calculate the corresponding magnitudes. By later inspecting which bins fall into the dusty star-forming locus, the dust content can be traced. A detailed study of a spatially resolved *UVJ* diagram for one of our galaxies can be found in the next chapter.

3.5 SED-Fitting

Galaxies emit radiation in all parts of the electromagnetic spectrum. As we previously introduced, the analysis of this radiation is our primary tool to study these astronomical objects and learn about their formation and evolution. How energy is distributed over different wavelengths or frequencies is called the Spectral Energy Distribution (SED). There is a wealth of available models and techniques that fit SEDs of galaxies from the whole observed spectral range, from the ultraviolet to the infrared.

The various physical processes that take place within galaxies leave particular signatures on their integrated SEDs, each prevailing at different parts of the spectrum. By analysing in detail the SED of a galaxy, we should thus be able to thoroughly comprehend its properties. SED-fitting consists in fitting models to observed SEDs with the goal of deriving its physical properties and therefore analysing the galaxy in detail.

In the last decade we have seen the development of new facilities and emergence of large multiwavelength surveys, allowing us to observe full SEDs of galaxies. Simultaneously, models and techniques have been conceived to distil the complicated information engraved in the SEDs. These models are vital to link the observed fluxes with physical properties of the galaxy.

In this work we use two distinct SED-fitting techniques: Prospector and EAZY. In the following sections we delve into these two different methods of modelling galactic SEDs.

3.5.1 Population Synthesis Models

The electromagnetic radiation in galaxies originates from stellar light, excluding AGN dominated galaxies, either from direct emission from stars or from reprocessed radiation by dust and gas in the ISM. Therefore, the UV-to-IR SED includes a wealth of information about the stars and the surrounding ISM.

The two spectral fitting codes that we explain below, EAZY and Prospector, use population synthesis models to interpret galaxy spectral energy distributions. Population synthesis ties back to what was previously introduced about the different components of galaxies and the light they emit.

The primary component of any stellar population synthesis (SPS) model is a gas cloud of some fixed mass, which then collapses to form a simple stellar population (SSP) (Conroy, 2013). The SSP then describes the evolution of an SED for a single stellar population, that evolves simultaneously, at a fixed metallicity and chemical abundance. Therefore, we can see that an SSP will be dependent on a set of basic input parameters, which are the initial mass function (IMF), itself dependent on metallicity and abundance of various elements, the luminosity and temperature evolution of stars of different masses tracked by the isochrones and the libraries containing the stellar spectra.

The IMF is required to assign the distribution of the stars along the main sequence within a given stellar population. It also describes the overall mass-to-light ratio and play a role in determining the rate of the passive luminosity evolution. The isochrone curves, as the name suggests, describe the position of stars that share age and metallicity on the Hertzsprung-Russell (HR) diagram. These are constructed by considering the evolution of the stars at both extremes of hydrogen burning limits ($0.1M_{\odot} - 100M_{\odot}$). The libraries of stellar spectra are used to interpret the output physical parameters of stellar evolution calculations such as the surface gravities and metallicity dependant effective temperatures, and convert them into an observable SED. These libraries could be either based on theoretical predictions or empirical models based on observations, with each one having its own advantages and disadvantages (Conroy, 2013).

The SSPs can then act as foundations for a more elaborate model of stellar emission - the composite stellar populations (CSPs). The CSPs contain multiple populations instead of a single SSP, and differ from SSPs in three major ways. Firstly, CSPs contain SSPs with stars at a range of different ages that are given by star-formation histories (SFHs). Secondly, they can contain populations of different metallicities, given by time-dependent chemical abundance models. Lastly, the dust attenuation is now being taken into account.

There are various degrees of complexity that can exist for SFHs. However, most of these can be generalised as either parametric or non-parametric descriptions of the star formation rate across cosmic time. The dust in the ISM is present in all star-forming galaxies and is an important factor to take into account when considering stellar models. We have already introduced how dust attenuates light in the bluer wavelengths (UV through optical to NIR) and re-emits in the NIR through to FIR. Generally, these two aspects are modelled separately as they depend on different properties. A principal component in describing dust obscuration is the amount and geometric distribution of dust in the galaxy, while the re-emission is primarily described through distribution of grain sizes and the effective intensities of the interstellar radiation fields.

Another important input parameter for modelling a stellar population are the nebular emission lines. These are normally handled by a wide array of available photoionisation codes that are able to make calculations for the nebular emission lines as a function of the physical state of ISM. These include CLOUDY (Ferland *et al.*, 1998) and MAPPINGSIII (Groves *et al.*, 2004). It is necessary to include nebular emission lines in our recipes of stellar populations because they can contribute to a significant fraction of the flux density integrated across a broadband filter, with the fractions reaching 20% to 60% for low metallicity environments (Anders and Fritze-v. Alvensleben, 2003). The effects of nebular emission lines will therefore be highly pronounced at high redshift where a significant portion of galaxies is dominated by Population II stars (Schaerer and de Barros, 2010; Atek *et al.*, 2011).

With all the combined components one can then integrate through a range of metallicities and stellar ages to obtain a composite stellar population that can be used to provide model SEDs of entire galaxies. The whole process to obtain a CSP can be seen in Figure 3.8.

Both EAZY and Prospector SED-fitting methods incorporate FSPS (Flexible Stellar Population Synthesis; Conroy *et al.*, 2009; Conroy and Gunn, 2010) models, which are composite stellar population models that allow user input.

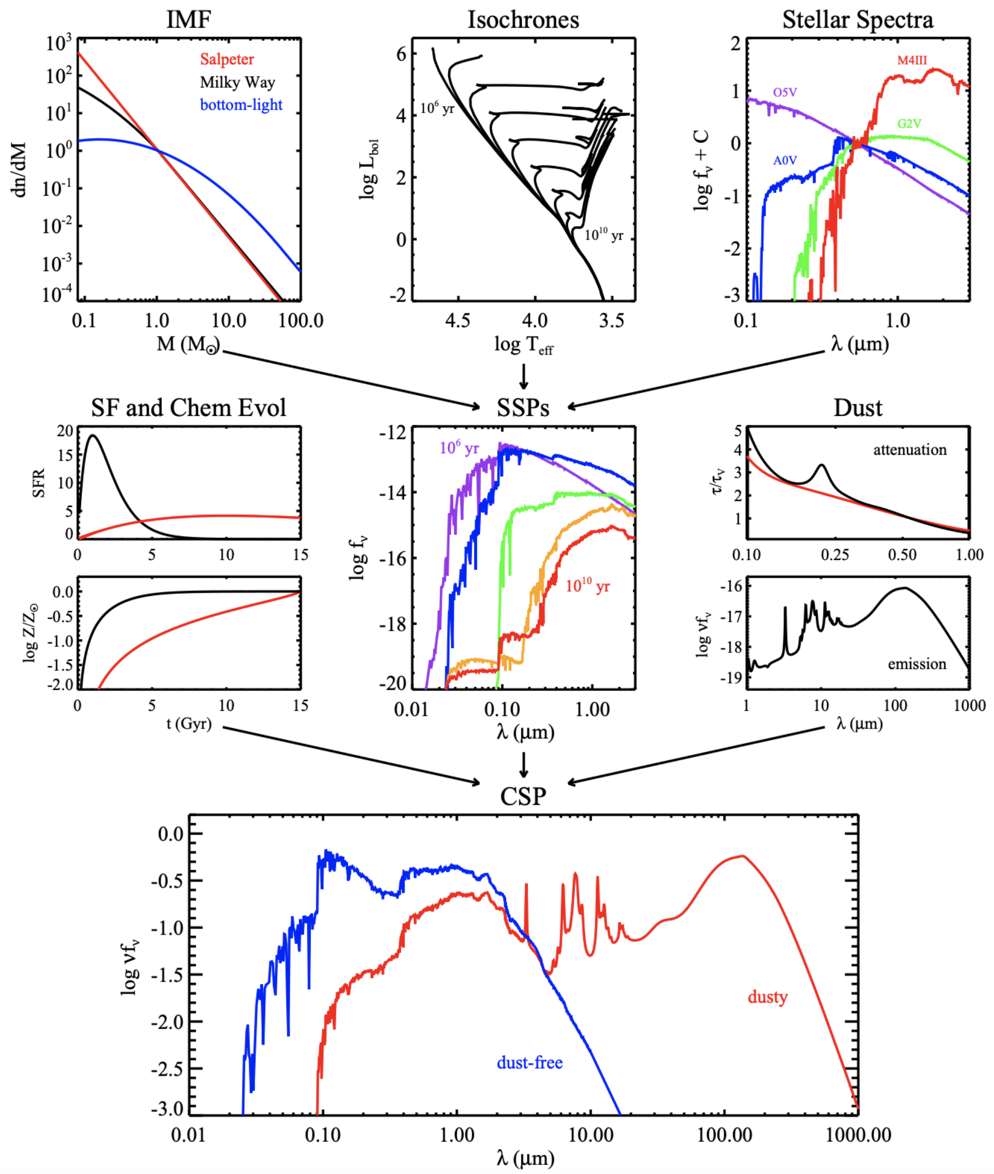

Figure 3.8: An overview of constructing a composite stellar population (CSP). The top panel shows the essential ingredients that are used to construct a simple stellar population (SSP) - the IMF, isochrone curves and the stellar spectra libraries. The middle panel displays the components of a composite stellar population - the SFH and metallicity evolution models, multiple SSPs and the dust (Image credit: Conroy, 2013).

3.5.2 EAZY

EAZY (Brammer *et al.*, 2008) is a public software program that fits a set of galaxy SED templates to the observed photometry, providing photometric redshifts as well as other physical properties. The templates are FSPS models, as described above.

The EAZY algorithm moves across a grid of redshifts defined by the user. At each redshift, it fits the best synthetic template spectrum using χ^2 minimisation, where χ^2 is defined as

$$\chi^2_{z,i} = \sum_{j=1}^{N_{filt}} \frac{(T_{z,i,j} - F_j)^2}{(\delta F_j)^2} \tag{3.4}$$

with N_{filt} the number of filters, $T_{z,i,j}$ the synthetic flux of template i in filter j for redshift z, F_j the observed flux in filter j, and δF_j the uncertainty in F_j. Instead of finding the template T_i that fits the source best, the code obtains the best-fitting coefficients, α_i, in

$$T_z = \sum_{i=1}^{N_{temp}} \alpha_i T_{z,i} \tag{3.5}$$

with all $\alpha_i \geq 0$. The resulting fit is therefore a linear combination of the input templates.

The template set is based on synthetic UBVRIzJHK "photometry" of galaxies in a semi-analytic model, which is based on the Millenium Simulation (Springel *et al.*, 2005). While models cannot accurately reproduce the observed galaxy population at high redshift, this set is comparable and sometimes more complete and representative at high redshifts than local current spectroscopic surveys.

In this work we use `eazy-py`: a set of pythonic photometric redshift tools based on EAZY, that is available on `https://github.com/gbrammer/eazy-py`. This public software allows us to fit SEDs to our galaxies and obtain physical parameters. In the next chapter, we compare results from the EAZY and Prospector SED-fitting schemes, as well as compare the derived EAZY A_V with our extinction maps obtained with Hα/Paβ.

3.5.3 Prospector

Parallel to our study in Copenhagen, a group from Tufts University in Boston, led by Danilo Marchesini, has also been working with the Dusty Cosmos Survey. They have been using the SED-fitting code `Prospector` (Johnson and Leja, 2017; Leja *et al.*, 2017), to obtain physical parameters of the galaxies. The code is publicly available here `https://github.com/bd-j/prospector`.

Until now, SED-fitting techniques of galaxies have broadly adopted basic models to obtain stellar masses, with fixed stellar metallicities, simple parametric star formation histories (SFHs), rigid and simplistic dust attenuation curves, and minimisation of chi-squared. On the other hand, Prospector includes a flexible attenuation curve and metallicity. Prospector uses FSPS, which contains nebular emission and considers both attenuation and re-radiation from dust. Prospector provides some innovation on flexible SFHs and also techniques for sampling parameter distributions. It comprises a 6-component non-parametric star formation history. With such a wide and adjustable range of parameters, Prospector is able to supply realistic uncertainties and unbiased parameters.

The Tufts team use the Prospector package to fit our broad- and narrow-band HST flux measurements in order to infer stellar population properties, using the Flexible Stellar Populations Synthesis (FSPS) stellar populations code (Conroy et al. 2009).

For both Prospector and EAZY, we use as input the images that are first PSF-matched and then binned with our Voronoi algorithm. Matching the PSF (Point Spread Function) consists roughly in degrading the UVIS and optical images to match the resolution of the IR data. Normally, we match the PSF to the F110W image, which has a growth curve figure for PSF-matching. The comparison and discussion between EAZY and Prospector can be found in the next chapter.

Star Formation History

The fundamental difference between EAZY and Prospector is that the latter allows various parametrisation schemes of the star formation history. The star formation history (SFH) describes how stars formed across cosmic time. The evolution of the SFH is mainly driven by a balance between feedback mechanisms and gas accretion. Other events such as merger driven starbursts are thought to play a comparable role albeit in a secondary sense. As we have seen before, the SFHs can either be parametric (i.e. described by models of varying complexity) or non-parametric, where the SFH could be dependent on a range of galaxy properties such as morphology or lookback time. Prospector allows for both cases, and later on we will compare its outputs with the EAZY modelling.

Parametric models estimate the SFHs of galaxies by using rather simple functional forms. Although they can be seen as the least flexible option for SFHs fitting, they are broadly used due to their relative simplicity and computational speed. The most widely used parametric SFH model is probably the exponentially declining model (tau models; Mortlock *et al.*, 2017; Wu *et al.*, 2018; McLure *et al.*, 2018). The tau models define T_0 as the time when star-formation goes from zero to its maximum value. Once the maximum is reached, the star-formation declines exponentially with some timescale τ:

$$SFR(t) \propto \begin{cases} \exp\Big(-\frac{t-T_0}{\tau}\Big) & t > T_0 \\ 0 & t < T_0 \end{cases} \tag{3.6}$$

Tau models can be extended into delayed exponentially declining SFHs (delayed models; Ciesla *et al.*, 2017; Chevallard *et al.*, 2019). These eliminate the condition that star formation must decline after reaching T_0 and solves the discontinuity at t=T_0. Delayed models are more physical and flexible than tau models, with the SFR being:

$$SFR(t) \propto \begin{cases} (t-T_0)\exp\Big(-\frac{t-T_0}{\tau}\Big) & t > T_0 \\ 0 & t < T_0 \end{cases} \tag{3.7}$$

On the other hand, Prospector also allows to model the SFHs with non-parametric prescriptions (Leja *et al.*, 2017). Non-parametric SFHs are very flexible and can provide accurate errors on SFH parameters when compared to simpler previous models, at the expense of longer computational time.

Given the characteristics of our sample, which contains a large number of merger driven starbursts, the non-parametric SFH model could be potentially more preferable, since tau models would not be sufficient to adequately address the processes that deviate from the 'regular' star formation.

4 Results and Discussion

In this chapter we delve into our results and discuss their implications. First, we present panels for the whole sample of 53 local galaxies, which consist of images obtained following the methodology explained in the previous chapter. Next, we compare attenuation inferred from the nebular regions to continuum attenuation derived from the EAZY template fits. Then, we study the association between extinction and the *UVJ* diagram. Later, we compare the SED-fitting methods from Prospector and EAZY, obtaining multiple physical properties with both techniques. Finally, we investigate how the resolution of our observations can affect the derived physical properties of galaxies.

The codes that we use for subtracting the continuum, creating the extinction maps with the Hα/Paβ decrement, plotting the RGB images of our galaxies, building the *UVJ* diagram and fitting our targets with EAZY, are available here `https://github.com/claragimenez/eazy-fitting`.

4.1 Extinction Maps

For all galaxies in our sample, we have produced Paβ/Hα extinction maps to measure the typical size scales and extinction levels of the dust obscuration. In this section we present some of the results. The rest can be found in the Appendix (section 8.1).

We create panels with the resulting images from every galaxy. Each panel contains the narrow-band filter images that target Hα and Paβ, the corresponding continuum-subtracted emission-line images, the RGB composite image, the extinction map obtained with the Paβ/Hα decrement, and the results from the EAZY fitting. Here we show the derived continuum attenuation (A_V) and specific star formation rate (sSFR) from the EAZY modelling. A relevant comment to make before inspecting some of the results, is that the Paβ/Hα decrement does not correspond to the visual extinction A_V, and thus cannot be expected to match the continuum A_V inferred by EAZY. This is because the lines and continuum, as we will test in detail later on, could trace different physical components of the galaxy, which could be mixed or spatially distinct, and that is part of what our extinction maps can test. A proper quantitative analysis of the extinction from both methods is performed in the next section.

We can start by discussing the results for one of the most extended sources in our sample, NGC4038, which is undergoing a merger with NGC4039 and the pair is also known as the "Antennae Galaxy". NGC4038 is currently going through a starburst phase (Wang *et al.*, 2004), which can be seen in the EAZY sSFR panel of Figure 4.1, with multiple substantial blue star-forming clumps. From the continuum subtracted images we can see that Hα is much brighter than Paβ. The correspondence between the EAZY A_V and the dust filaments from the RGB image is very noticeable. This behaviour is to be expected since EAZY will provide the continuum A_V, and the red channel in the RGB image (F814W) will be dominated by dust re-emission of absorbed continuum stellar light. The Paβ/Hα map also matches some high extinction regions from the continuum A_V plot, in particular in the lower right part of the image. The blue parts of the RGB image are well represented in the EAZY sSFR map as high-sSFR areas.

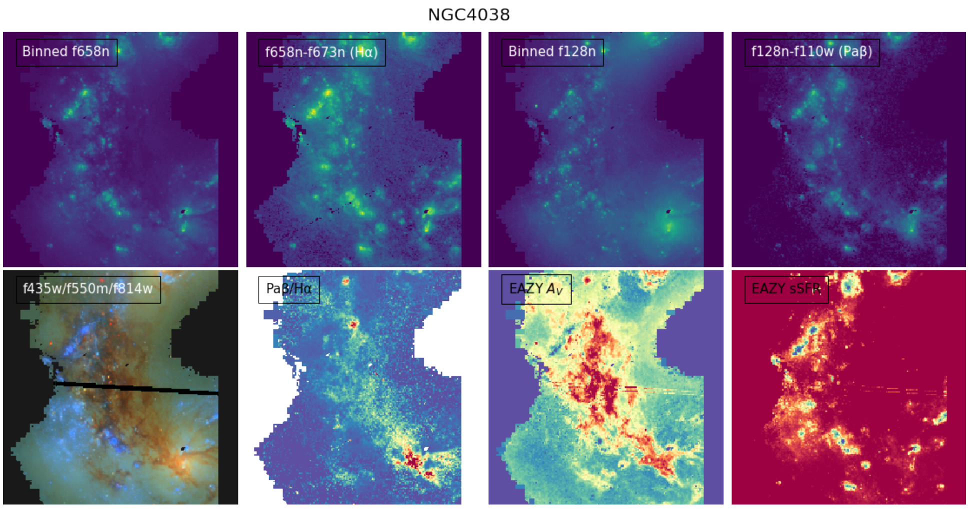

Figure 4.1: NGC4038 results.

Another interesting galaxy is NGC1482 (Figure 4.2). From the emission-line maps and the EAZY sSFR, we can see that most radiation is emitted from the nucleus, which is obscured from a highly inclined dusty disk with strong apparent dust lanes. This is confirmed by the RGB, the Paβ/Hα and the continuum A_V images. All of them show large amounts of dust extinction across the disk of the galaxy. In the continuum-subtracted Hα image there are hints of gas outflows from the bulge of the galaxy. As expected, both continuum A_V and Paβ/Hα match well with the infrared emission observed in the RGB image (red channel, obtained with the broad-band filter F160W), since this is where dust re-emits the radiation that it absorbs from optical and UV wavelengths.

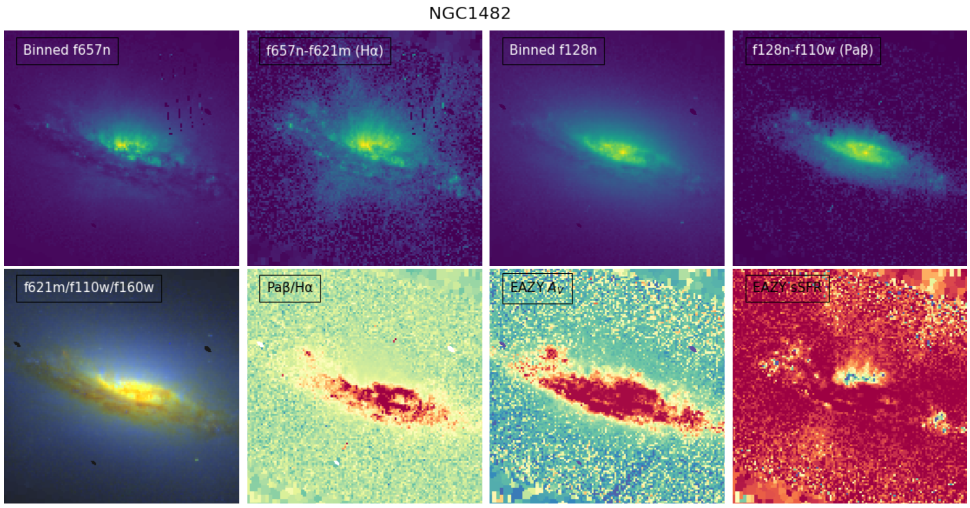

Figure 4.2: NGC1482 results.

Figure 4.3 shows the results for three galaxies from our sample. The top panel corresponds to ARP220, which is also an undergoing merger with another galaxy. It is the closest ultra-luminous infrared galaxy (ULIRG) to Earth. ARP220 is considered to be an example of a galaxy that has extremely obscured star-formation (Graham *et al.*, 1990). From the emission-line maps we can see that Paβ is brighter than Hα and appears not to be significantly extended, only shining in a small central part of the image. The RGB gives us a hint regarding the presence of dust across the image, with a particularly red area in the bulge. The Paβ/Hα matches this red spot. The results from EAZY agree with the rest of the tiles: continuum A_V is high across the image, especially in the centre, showing some filamentary shapes like the RGB IR channel, whereas we only see high sSFR where Paβ and Hα are bright. The middle panel in Figure 4.3 shows the IRASF10038-3338 galaxy. Later, we will conduct a comparison between the SED-fitting methods EAZY and Prospector using this galaxy. From the results in Figure 4.3, we can see that the line emission is very centralised, mostly appearing bright in the bulge, with some additional radiation in the lower spiral arm. The extinction is also very focused in the centre. The bottom panel of Figure 4.3 shows NGC2146. From the RGB image we already see long wide filaments of extinction, that are matched by

Paβ/Hα and continuum A_V. The sSFR is only high in small clumps in the edges of this extended extinction distribution. Despite having this broad seemingly all-obscuring dust distribution, the emission-line map for Paβ is very bright. On the other hand, Hα does appear to suffer extinction across the galaxy.

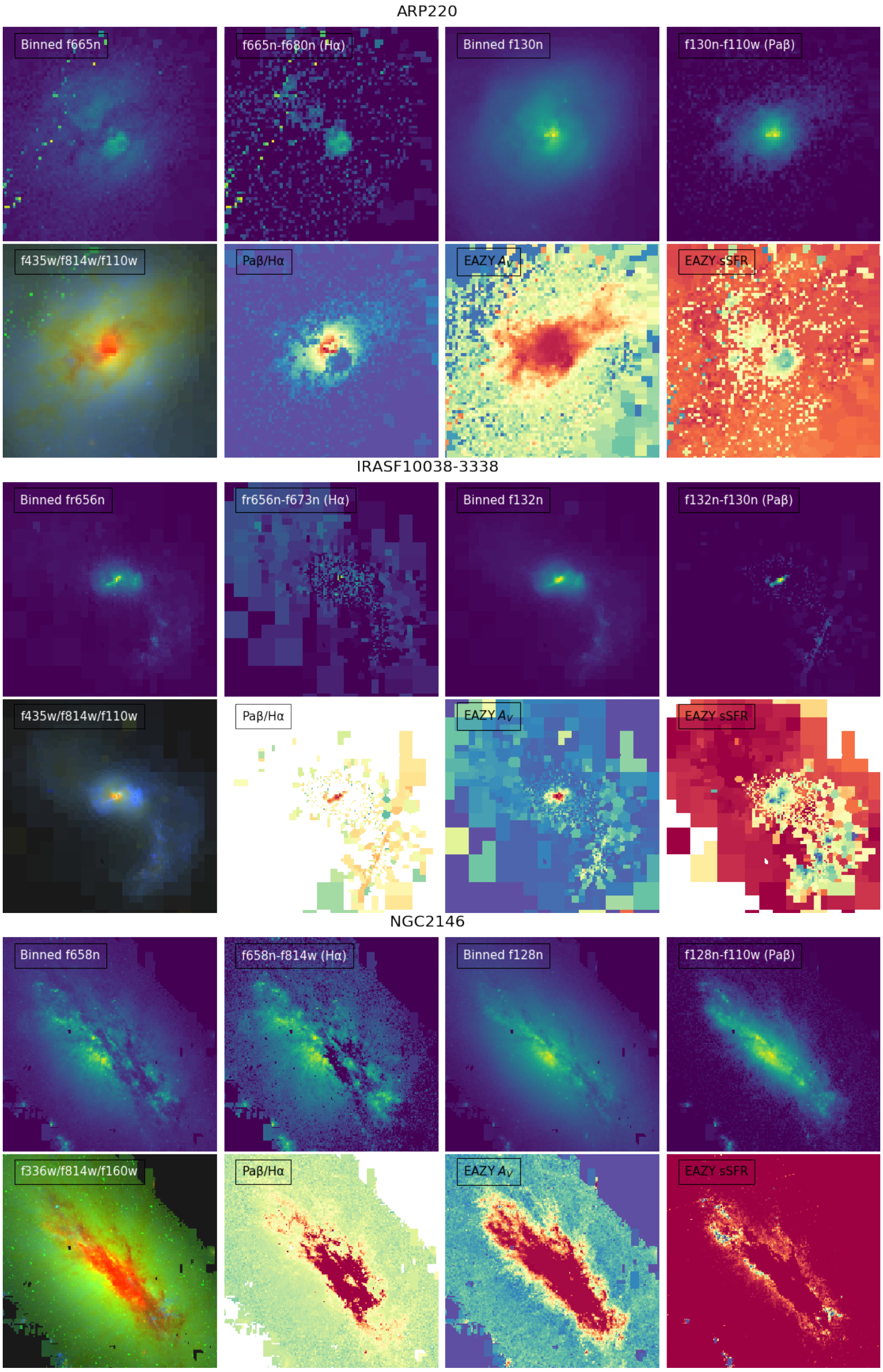

Figure 4.3: Multiple results for three galaxies of our Dusty Cosmos survey.

4.2 Line Ratio versus EAZY

To be able to compare the extinction inferred from the nebular lines versus that from the overall continuum shape (i.e., gas versus stars), we need to convert the line ratio to visual extinction A_V. In the previous chapter we explained in detail how to get A_V from the Hα/Paβ decrement, which we term $A_{V,gas}$, following the distinction by Greener *et al.*, 2020. Once we have $A_{V,gas}$ for all of our galaxies, we can compare with the continuum A_V obtained with EAZY. In this section we conduct the comparison on one galaxy first, NGC1482, and then extend it to the whole sample.

Dust attenuation models in spiral galaxies commonly distinguish two principal elements. The first component is the diffuse interstellar medium (ISM), that has a radial dependency and its density peaks towards the bulge. The other dust component is the birth clouds (BCs), where dust is very clumpy and optically thick. Only the youngest most massive O and B stars will stay near their BCs, the rest of stars will migrate outwards. These bright stars will ionise the surrounding gas creating HII regions.

As we have seen, measurements of the line ratio are used as a diagnostic to derive the dust attenuation in the gas. Following Greener *et al.*, 2020, we can hypothesise that the extinction obtained with the decrement is due to the birth clouds and not only to the diffuse ISM. On the other hand, the EAZY continuum A_V will account for the attenuation of the flux from the average stellar population. The study that follows will allow us to either test or discard these hypotheses.

We start by focusing our study on the NGC1482 galaxy. In multiple figures in our work we have portrayed many properties of this galaxy (see e.g., Figures 4.2 and 3.6). We calculate $A_{V,gas}$ from the line ratio as explained in section 3.3.1, assuming a reddening curve from Calzetti *et al.*, 2000 (C00), which yields k(Paβ)=1.27 and k(Hα)=3.33. Figure 4.4 shows the comparison between the continuum A_V values obtained with EAZY and with the Hα/Paβ decrement. Besides obtaining $A_{V,gas}$, we also calculate the corresponding propagated uncertainty ($\delta A_{V,gas}$). This allows us to mask any bins with $\delta A_{V,gas} > 0.1$ mag. Initially, the two extinctions seem to match in distribution, whereas we can already see that $A_{V,gas}$ values appear to be higher than the continuum A_V inferred with EAZY.

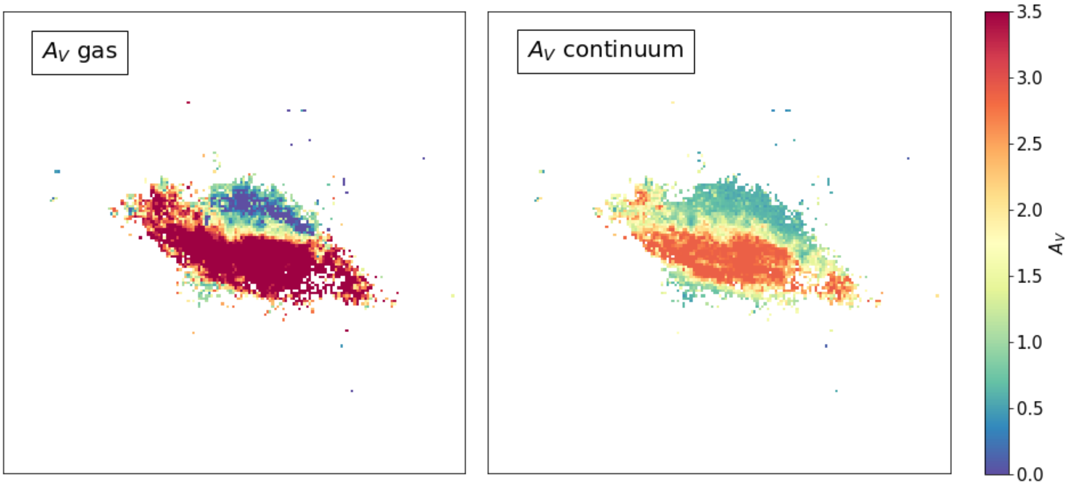

Figure 4.4: A_V maps obtained with the line ratio (left) and EAZY fitting (right) for NGC1482.

Figure 4.5 shows a quantitative comparison of the stellar and nebular extinction inferred from the continuum fits and line ratio maps, respectively. For starters, we see that the relation between the two is not 1:1. For almost each EAZY continuum A_V value, $A_{V,gas}$ is higher. EAZY A_V has an upper limit of 3 (intrinsic boundary from the templates). The red line corresponds to the median value of EAZY continuum A_V for bins of 0.4$A_{V,gas}$. Within the red dashed lines, 68% of the points are contained. The black lines indicate different scenarios of extra extinction following Wuyts *et al.*, 2013. This paper discusses the need to account for an extra extinction (A_{extra}) happening locally in the birth clouds, on top of the attenuation by diffuse dust in the galaxy (A_{cont}). We consider here that continuum A_V matches the A_{cont}, and that the extinction obtained from the line ratio corresponds to the sum of both terms, $A_{V,gas}$=A_{extra} + A_{cont}. The solid black line represents A_{extra}=0, meaning no extra extinction, so that the continuum A_V and $A_{V,gas}$ should match, since they would both simply represent the attenuation due to the diffuse ISM. The lower dashed line corresponds to a local calibration from C00, where the extra extinction from BCs represents 1.27A_{cont}. The middle black dashed line from Figure 4.5 represents the derived prescription for extra extinction from Wuyts *et al.*, 2013. They found $A_{extra} = 0.9A_{cont} - 0.15A^2_{cont}$.

For NGC1482 we obtain very interesting results. Both Figures 4.4 and 4.5 show higher $A_{V,gas}$ values than continuum A_V. Figure 4.5 clearly shows this

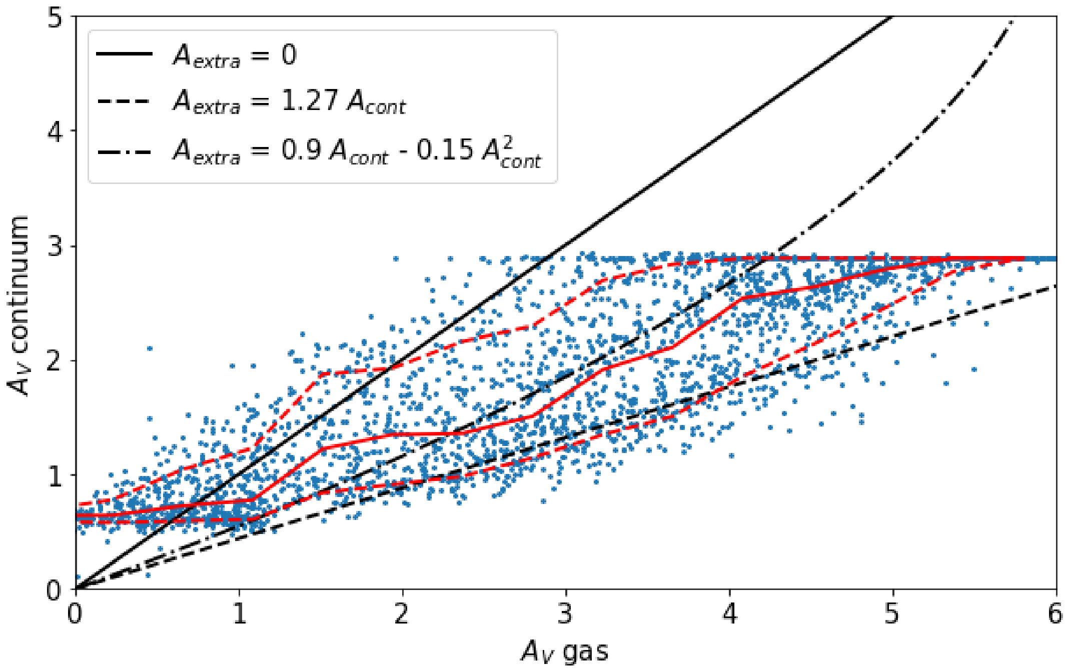

Figure 4.5: Scatter plot of $A_{V,gas}$, obtained using a reddening curve from C00, versus continuum A_V for NGC1482. The black lines indicate several scenarios of extra extinction as in Wuyts *et al.*, 2013. The red line is the median A_V for bins of $0.4 A_{V,gas}$. The dashed red lines stand for the 68% confidence interval.

trend, proving that for this galaxy we have to account for extra extinction from the birth clouds, and that the attenuation in the gas is not only due to diffuse ISM. Moreover, the median red line seems to fit best with the prescription for extra extinction from Wuyts *et al.*, 2013.

The next step is to extend this study to our whole sample, to see whether it agrees with the results from NGC1482 and there is indeed a consistent need to account for extra extinction for all galaxies. We obtain $A_{V,gas}$ exactly as before, using the reddening curves from C00. We reproduce the scatter plot from Figure 4.5, but this time plotting the measurements of the whole sample. Figure 4.6 shows the results. The points are binned so that we can see where the concentration is higher, and we have masked the contributions from bins where $\delta A_{V,gas} > 0.1$ mag. The same lines are used as in Figure 4.5. In this scenario, the solid red line seems to follow better the C00 prescription for extra extinction above $A_{V,gas} \sim 1.5$. This curve illustrates that the stellar continuum suffers 40% the reddening that the gas suffers, i.e., $E(B-V)_{stars} = 0.4E(B-V)_{gas}$ (Calzetti, 1997). $A_{V,gas}$ seems to be systematically higher than the continuum A_V at all regimes.

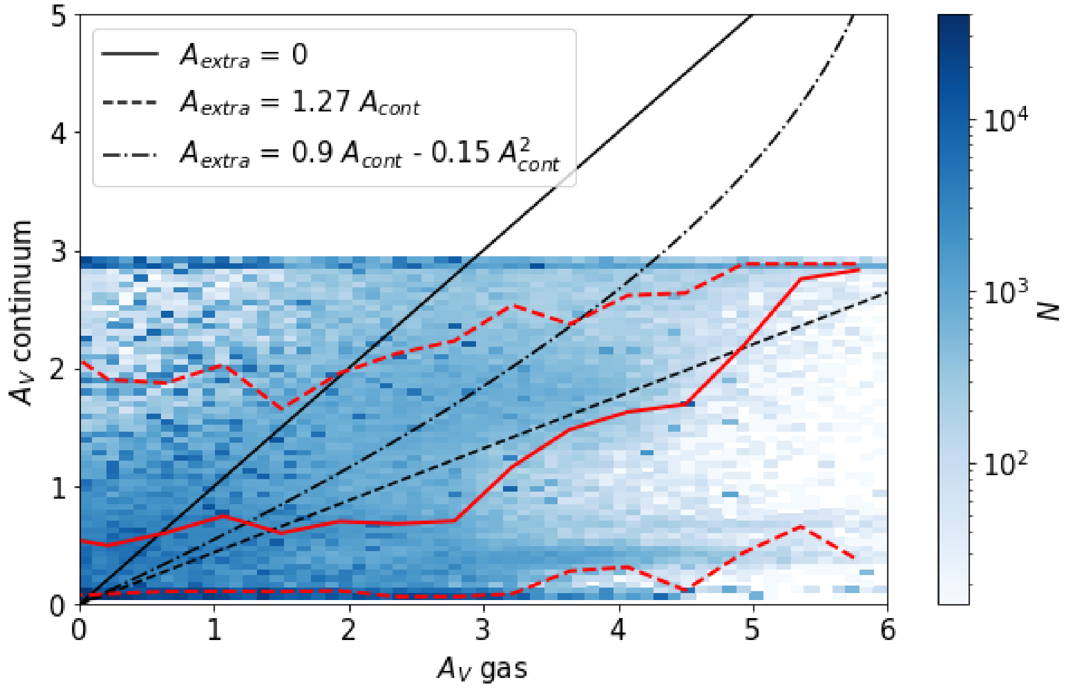

Figure 4.6: Scatter plot of $A_{V,gas}$, obtained using a reddening curve from C00, versus continuum A_V for our whole sample of nearby galaxies. The different coloured lines represent the same as in Figure 4.5.

These results suggest that we cannot consider the extra attenuation from birth clouds to be negligible in our sample, we must definitely account for it to provide a better prescription of the dust content of the galaxies.

4.3 Spatially Resolved *UVJ* Diagram

As we have seen in a previous chapter (section 3.4), the *UVJ* diagram separates between star-forming (SF) and quiescent galaxies. Furthermore, it breaks the degeneracy between age and reddening for red galaxies. The location in the *UVJ* diagram directly relates to continuum attenuation measurements, therefore, we will conduct a detailed study of a spatially resolved *UVJ* diagram to test how well it traces the dust content. We will perform this test on the NGC6786 galaxy.

Since this is a separate study from the SED-fitting comparison that we will conduct later on, we rebin this galaxy to reach a minimum bin size of 2×2 original pixels, so that the central parts have higher spatial resolution. The RGB image of NGC6786 can be seen in Figure 4.7. With this new binning, we can see in detail the dust filaments, as well as the bright blue gas ring in the bulge of the galaxy. The two oval black regions correspond to holes in the original weight image. The circular black spot in one of the spiral arms corresponds to a masked foreground star, in the line of sight of the galaxy.

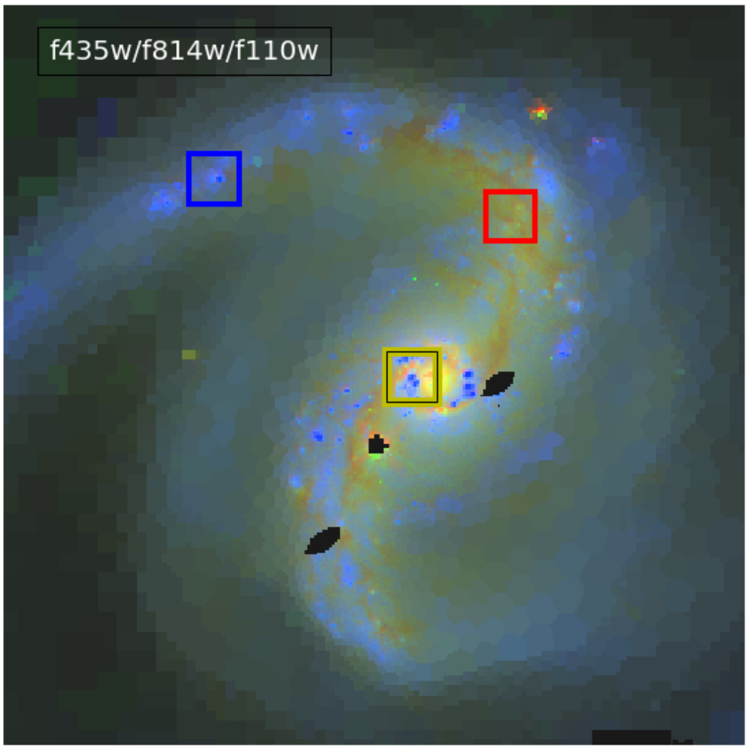

Figure 4.7: RBG image of the galaxy NGC6786. Three coloured boxes are plotted in different regions. Figure 4.8 shows where the bins from these regions fall within the spatially resolved *UVJ* diagram.

As we explained before, we use measured fluxes in the U, V and J bands to build the *UVJ* diagram. For NGC6786, these fluxes are obtained with the filters F435W, F814W and F110W, respectively. Since these are not precisely rest-frame *UVJ*, the separating border derived in Williams *et al.*, 1996, that splits quiescent from star-forming, does not work for our diagram. To determine this separation in our *UVJ*, we plot the twelve EAZY templates. These templates are scaled to the redshift of NGC6786, z=0.03. We are able to integrate the desired fluxes for each template, so every one of them will represent a point in our *UVJ* diagram. Since we know which templates represent quiescent or star-forming galaxies, we can determine the separation between the two regions. This separation is shown as the dashed black line in the spatially resolved *UVJ* diagram in Figure 4.8. The templates are represented by the triangles. They are colour-coded according to their specific star formation rate. This allows us to see which templates are quiescent (redder colours therefore low sSFR) and which are star-forming (appear bluer, which means high sSFR).

NGC6786 appears to be undergoing a starburst (also confirmed by the SFR versus M plot shown in Figure 4.23), so we will expect most of its bins to be in the star-forming region of the diagram. A galaxy is defined as a starburst when it is experiencing an exceptionally high rate of star formation relative to the average for galaxies with similar stellar mass. If the SF distribution is quite extended, according to multiple literature studies (Wuyts *et al.*, 2007; Patel *et al.*, 2011; Patel *et al.*, 2012; Fang *et al.*, 2018) this means that there will be varying extinction in the spatial bins of the galaxy.

To test the previous statement, we analyse different regions of the galaxy and see where they fall within the *UVJ* diagram. Taking as reference Figure 4.7, we want to select three distinct regions. One of them could be the central part of the galaxy. We would expect it to have high specific star formation, with some dust, and to be redder than other SF regions such as the spiral arms. The spiral arms could be another region to study. We anticipate them to be in a bluer region of the SF distribution, due to having little dust content (compared to other areas). The last domain that we can study is a specifically obscured place within the galaxy. We can see dust filaments in the inner part of the spiral arms, so that is where we will place our box to study. We would expect this domain to be within the red dusty area of the *UVJ* diagram, so in the top-right section.

Figure 4.7 shows the RGB image of NGC6786 with three marked boxes. They represent the areas described above, that we plot in the spatially resolved *UVJ* diagram shown in Figure 4.8. As we expected, the dusty and the spiral arm regions fall within the part of the diagram that we anticipated just by looking at its characteristics. On the upper right corner, we have the bins belonging to dusty filaments (red box and points). Blue SF regions of the spiral arms (blue box and points) fall within the lower left part of the wide SF distribution in the diagram. The region whose distribution in the diagram is a bit different than what we anticipated is the bulge. We expected a compact distribution towards the centre of the SF sequence in the *UVJ*. Instead, we obtain a wide scattered distribution, with parts that have high extinction and others that contain hardly any dust. These points can be seen in yellow in Figure 4.8 and correspond to the yellow box in Figure 4.7.

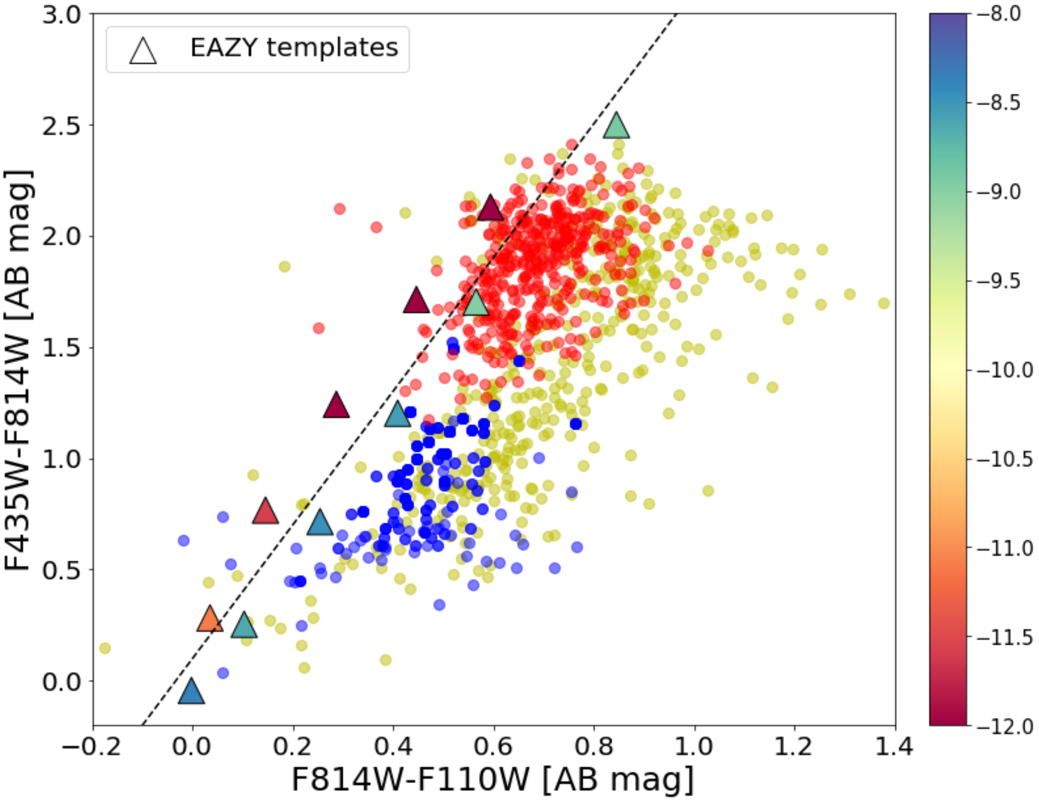

Figure 4.8: Spatially resolved *UVJ* diagram of NGC6786. The coloured points belong to the different regions assigned in Figure 4.7 to study various levels of extinction in NGC6786. The dashed black line separates quiescent from SF bins according to the EAZY templates, which are the triangles colour-coded according to their specific star formation rate (sSFR).

Figure 4.8 already seems to confirm that the wide distribution of SF bins can be explained by different levels of extinction. Even the colour gradient in the EAZY templates points that way: the SF templates appear greener on the top right (lower sSFR, more A_V) and bluer on the bottom left (higher sSFR, less obscuration in this region). We can do another experiment to finally test this and link the *UVJ* diagram with other studies conducted throughout this work. We can colour-code the points from the three regions in NGC6786 according to their inferred A_V from the nebular emission and from the continuum emission. Using the same procedure as explained in previous sections, we obtain $A_{V,gas}$ and A_V continuum for each bin that we plot in Figure 4.8. The results can be seen in Figure 4.9.

The top panel in Figure 4.9 displays the selected bins from Figure 4.7 colour-coded according to their $A_{V,gas}$, inferred from the Hα/Paβ decrement. We can perfectly see that $A_{V,gas}$ increases towards the upper right corner of the SF region on the *UVJ* diagram, as we would expect. On the other hand, the lower panel of the figure shows the same bins, but colour-coded according to their continuum A_V, computed by EAZY. The gradient of increasing A_V towards the upper right is less steep, but we can still see it. Furthermore, connecting with our previous results from Figures 4.5 and 4.6, $A_{V,gas}$ is systematically higher than the continuum A_V. For both panels, we observe that the EAZY templates' colour-scheme agrees with the trends of increasing extinction observed in the bins.

To wrap up this whole study, we can close the circle by going back to the scatter plot $A_{V,gas}$ versus A_V continuum, plotting the bins from the different NGC6786 regions. Figure 4.10 shows the result. If we first focus on the blue points, these correspond to the blue box on Figure 4.7. We selected this area because we expected it to be star-forming due to the visible blue knots in the RGB image and no apparent dust obscuration. On Figure 4.8 we confirm that the bins are star forming, and that they have high sSFR and low A_V, according to its position in the lower left corner of the *UVJ* diagram. When colour-coding according to A_V, we see that both $A_{V,gas}$ and A_V continuum are low for these bins. Finally, on Figure 4.10 they appear as not particularly extinct, since both A_V values do not surpass 2 mag. We can also see that the points are on the left of the solid black line. This means that there is no need to account for extra extinction due to birth clouds (BCs) in these bins.

If we now focus on the red points, on the RGB image they appear as a dusty region, particularly obscured. In the *UVJ* diagram, as we would expect, these bins appear in the upper right corner of the SF distribution, since we think that this is the region of higher A_V. Figure 4.9 confirms this hypothesis, since these bins have the highest $A_{V,gas}$ when compared with the rest of coloured regions. From the lower panel we see that it is not the highest A_V continuum region. Figure 4.10 displays the red points as a wide distribution, particularly scattered within the region where extra extinction due to BCs needs to be accounted for. For the majority of points, continuum A_V is lower than A_V inferred from the recombination line ratio.

Finally, the yellow points in Figure 4.10 correspond to the bulge of the galaxy. On the spatially-resolved *UVJ* diagram (Figure 4.8), we can see that some bins are quiescent in the bulge, but most of them are scattered across the SF distribution. From Figure 4.9, we see that these bins are particularly extinct

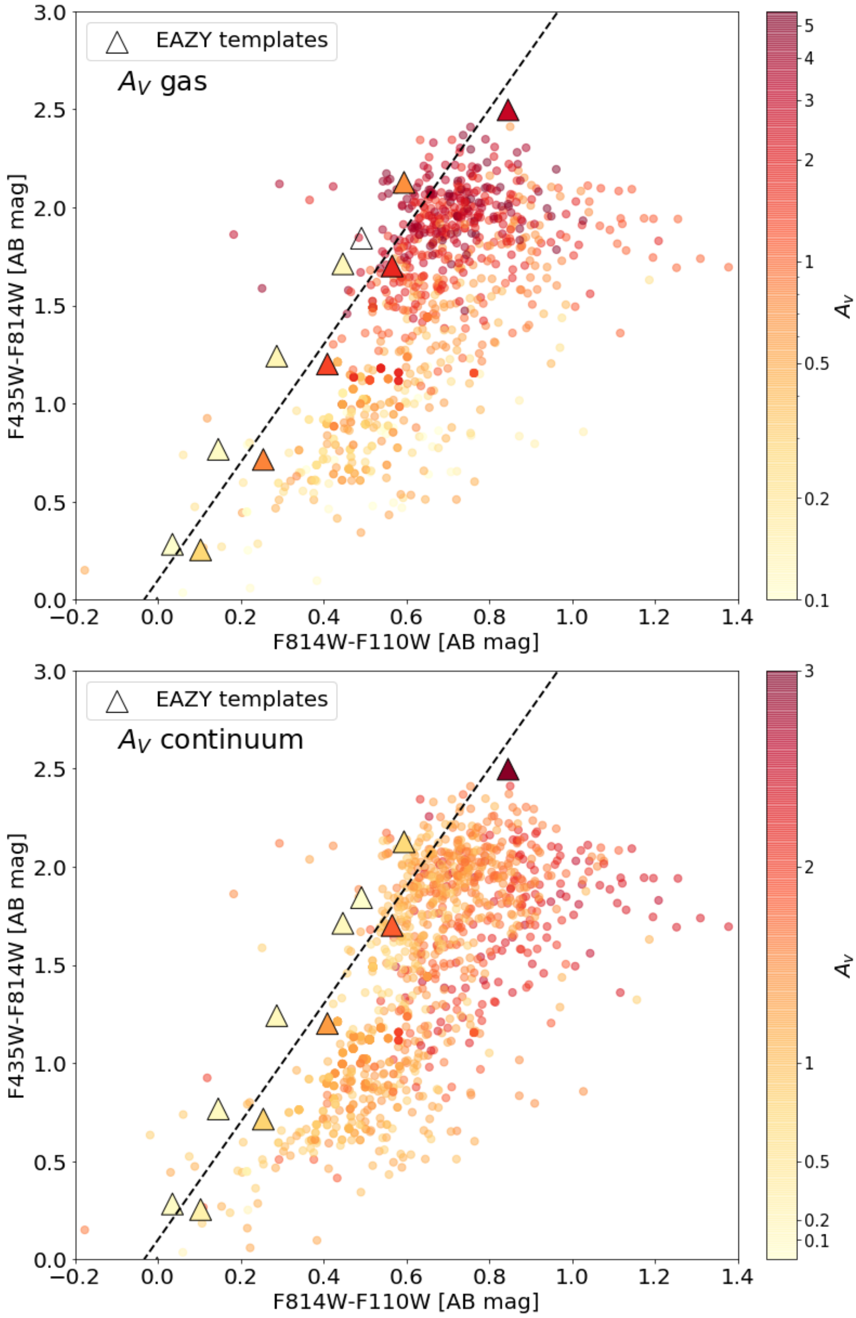

Figure 4.9: Spatially resolved *UVJ* diagrams of NGC6786, colour-coded according to the A_V inferred from the nebular lines (top panel) and the continuum (bottom panel). The dashed black line separates quiescent from SF bins according to the EAZY templates, which are colour-coded in A_V too.

in A_V continuum. Figure 4.10 confirms this trend, containing most yellow points to the left of the solid black line. As for the blue points, this indicates that A_V continuum is consistently larger than $A_{V,gas}$, and that we will find few additionally-obscured BCs in the bulge of NGC6786, that make it necessary to account for an extra term of attenuation.

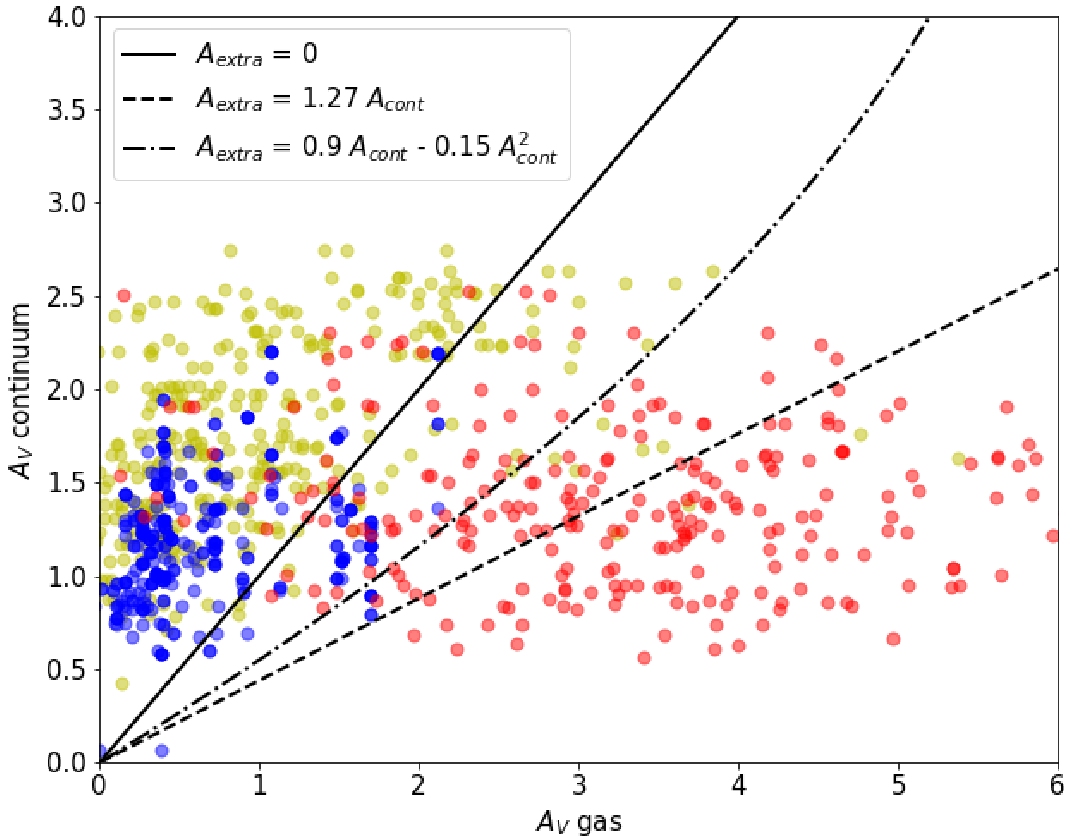

Figure 4.10: Scatter plot of $A_{V,gas}$ versus A_V continuum for the NGC6786 bins specified in Figures 4.7 and 4.8. The black lines represent the same as in Figures 4.5 and 4.6.

With this analysis we test that the location in the *UVJ* relates to direct extinction measurements, and these diagrams can prove to be useful not only to separate between quiescent and SF galaxies, but to study different levels of extinction. At the same time, we have connected this study with the comparison between A_V continuum and A_V gas. Both works seem to agree and point towards the need to account for extra attenuation in dusty regions surrounding birth clouds.

4.4 EAZY versus Prospector

The first comparison between EAZY and Prospector as SED-fitting codes for modelling our targets is done on the galaxy IRASF10038-3338. This galaxy is very well sampled with imaging in the following filters: F435W, FR656N (targeting Hα), F673N, F814W, FR914M, F110W, F130N and F132N (targeting Paβ). The RGB image of this galaxy can be seen in Figure 4.11.

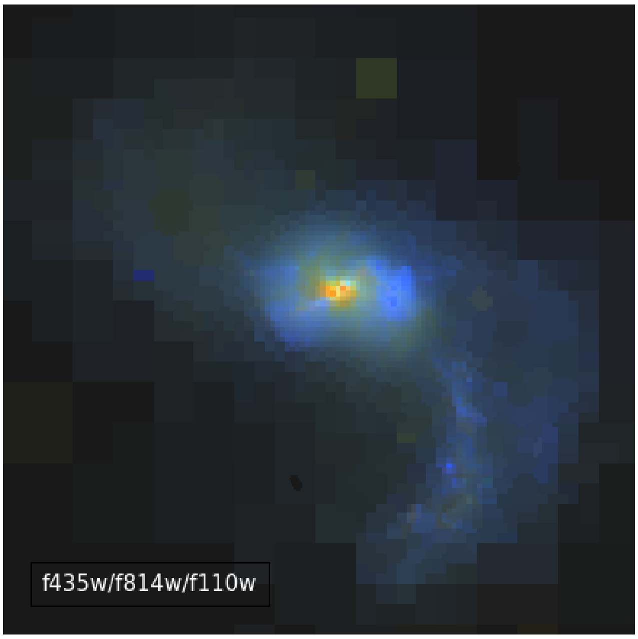

Figure 4.11: RBG image of the galaxy IRASF10038-3338.

4.4.1 Parametric SFH

After matching all PSFs to the F110W image, and binning the images with our Voronoi code, we run Prospector and EAZY and compare the outputs. For this, we obtain various physical properties of the galaxy: the visual extinction A_V (Figure 4.12), the stellar mass density (SMD, Figure 4.13), the star formation rate density (SFRD, Figure 4.14) and the specific star formation rate (sSFR, Figure 4.15). These quantities are either direct outputs from both the Prospector and EAZY fittings, or calculated from other output quantities.

This first study of the comparison between the two methods is done by running Prospector with a parametric star formation history (SFH). As we have mentioned in the previous chapter, this modelling of the SFH might be insufficient for our sample, and in the next section we will see the results if we instead use a non-parametric SFH when running the Prospector SED-fitting technique. EAZY on the other hand, has only one setting, which could be thought of as an in-between state among the parametric and non-parametric SFHs that are implemented in Prospector.

First of all, we do a visual inspection of the Prospector and EAZY differences. The first physical property that we study is the continuum extinction A_V, since it is related to the extinction maps that we obtain with the Paβ/Hα decrement. The continuum A_V is a direct output of EAZY and Prospector. Figure 4.12 shows the result. We observe that the extinction increases towards the centre of the galaxy, where more dust is located, and in one of the spiral arms. The outskirts and rest of the galaxy appear to have very low extinction and have A_V in the interval (0,0.6), whereas the highly obscured regions surpass A_V=1. Prospector seems to derive higher A_V values than EAZY in the outskirts of the galaxy.

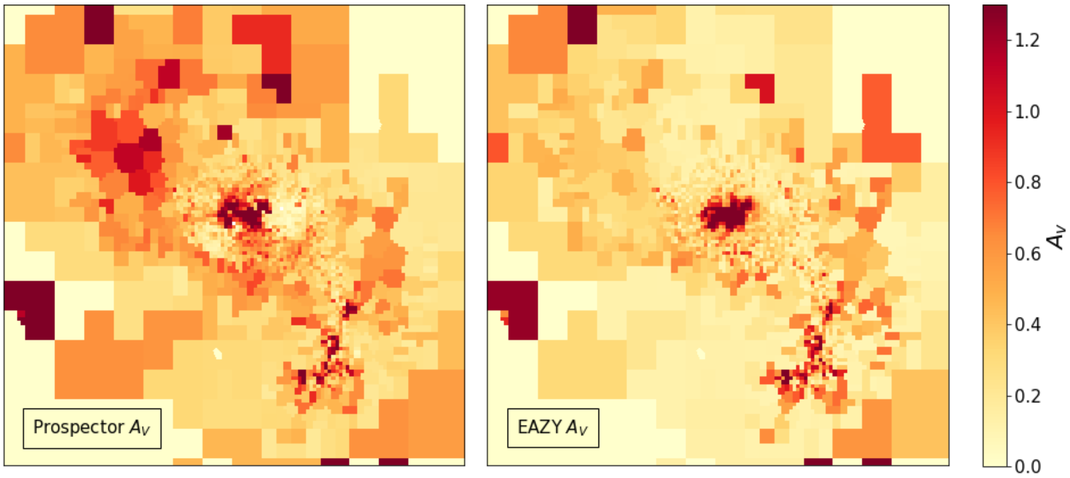

Figure 4.12: Comparison between the visual extinction (A_V) obtained with Prospector (left) and EAZY (right) for IRASF10038-3338.

Next, we calculate the Stellar Mass Density (SMD). The direct output from EAZY that we use for this is the mass-to-luminosity ratio M/L_V, as well as the luminosity L_V. By multiplying these two quantities we obtain the stellar mass M (in solar masses). To calculate the stellar mass density, we need to divide M by the physical area of each Voronoi bin. Our binning code outputs the area in pixels for each bin. We convert the area from pixels squared to parsec squared (pc^2) by using `WMAP9` (Hinshaw *et al.*, 2013) cosmological parameters[1] from the package `astropy.cosmology`. From the HST handbooks we learn that the WFC3 IR plate scale is 0.13 arcsec/pixel and after drizzling our pixels are resampled to 0.1" in the infrared mosaics. We calculate the conversion between arcmin and kiloparsec at the redshift (z) of the galaxy with `WMAP9.kpc_proper_per_arcmin(z)`. Finally, we can multiply this number by the 0.1 arcsec/pixel plate scale and the area of each bin (in pixels), and then convert to pc^2. By dividing the fitted stellar mass by this final area in pc^2 at each bin, we obtain a stellar mass density map of IRASF10038-3338.

[1] $H_0 = 69.32$ km s^{-1} Mpc^{-1}, Ω_M=0.287, Ω_Λ=0.712.

Figure 4.13 shows the result for the SMD obtained with EAZY and Prospector. The agreement between both fitting methods is very noticeable. We can see that the majority of mass is distributed in the centre of the galaxy. Since A_V is also higher in this part of the galaxy, this result suggests that the star formation (SF) is higher in the bulge, whereas it decreases in the outskirts of the galaxy. This agrees with having more stellar mass towards the centre of the source.

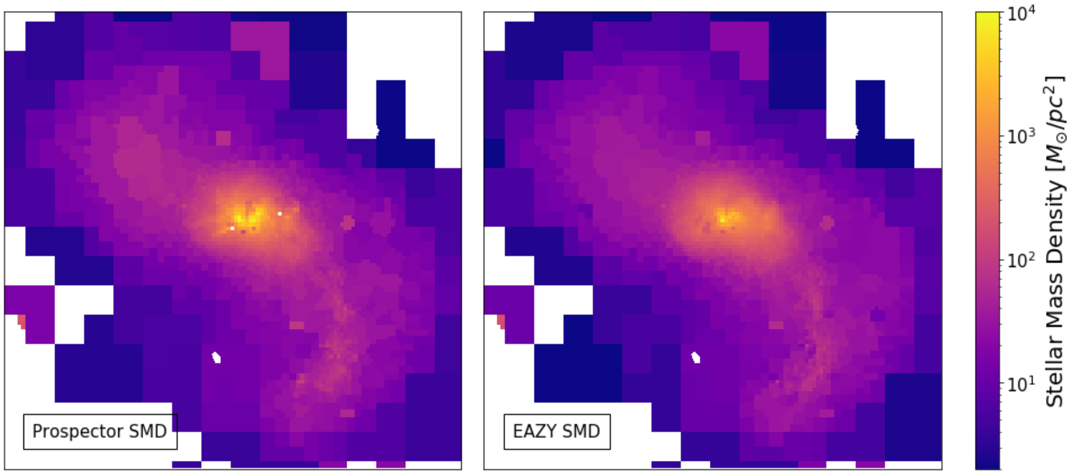

Figure 4.13: Comparison between the stellar mass density (SMD) obtained with Prospector (left) and EAZY (right) for IRASF10038-3338.

After studying the stellar mass density, we can also derive the star formation rate density (SFRD). EAZY outputs the SFR in units of solar masses per year. To calculate the SFRD we follow the same calculations as for the SMD, and divide the SFR by the area in parsecs squared. The resulting SFRD map can be seen in Figure 4.14. Again, visually both EAZY and Prospector derived SFRDs coincide fairly well. Following the previous discussion, if the centre of the galaxy is more dusty and has higher stellar mass density compared to the outskirts, we expect to find large SFRD within the bulge, and Figure 4.14 confirms this idea. The maximum SFRD is reached in the centre, with values of SFRD $\sim 10 M_\odot$/yr/kpc^2. We can see that Prospector and EAZY show differences of one or two orders of magnitude in the SFRD of the outskirts, where the SFRD is much lower, in particular for EAZY.

Finally, with the SFR and the stellar mass, we can calculate the specific star formation rate (sSFR=SFR/M), which we can see in Figure 4.15. The sSFR map follows the trend of the previous plots, with higher sSFR in the centre and the spiral arm, and very low values elsewhere. Besides agreeing in bright spots in the centre and one of the spiral arms, there seems to be high discrepancy in the rest of the galaxy with EAZY versus Prospector.

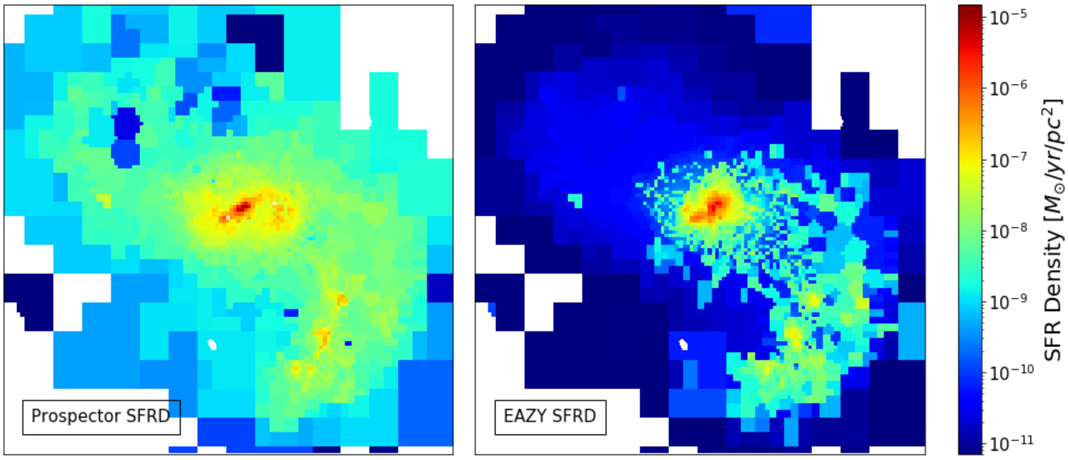

Figure 4.14: Comparison between the star formation rate density (SFRD) obtained with Prospector (left) and EAZY (right) for IRASF10038-3338.

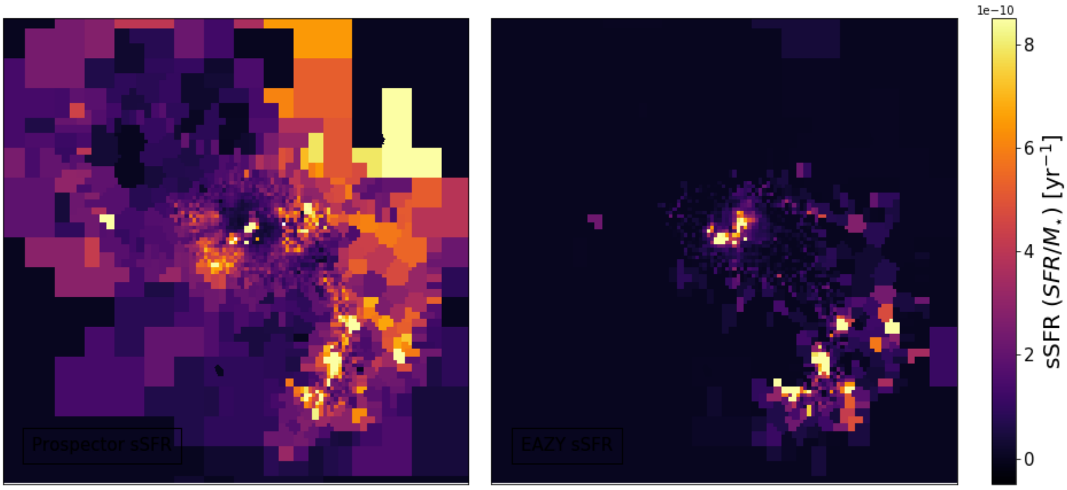

Figure 4.15: Comparison between the specific star formation rate (sSFR) obtained with Prospector (left) and EAZY (right) for IRASF10038-3338.

Now that we have visually inspected the differences between EAZY and Prospector, we can quantify them by plotting each physical property derived with Prospector versus with EAZY (Figure 4.16). We also calculate the median of the ratio EAZY/Prospector for each quantity, as well as the standard deviation σ, which can be seen in Table 4.1.

In the various scatter plots from Figure 4.16, we can see that Prospector consistently overestimates the parameters derived with EAZY. If we focus on the A_V plot (upper left), we see that there is particular discrepancy for low continuum A_V. This relates to Figure 4.12, where we can see that in the outskirts of the galaxy, EAZY derives low visual extinction, whereas Prospector gives consistently higher values. The sSFR (lower right) seems to have the highest dispersion and worst Prospector versus EAZY correspondence. Again, if we look at Figure 4.15, we see that the sSFR for the outskirts is highly overestimated with Prospector versus the EAZY result. The locus of points that are furthest from the 1:1 trend correspond to these outskirts' bins. This also happens with the SFRD (lower left), as we can see in Figure 4.14. A look at Table 4.1 confirms these large discrepancies. We see that σ for the ratio EAZY/Prospector with parametric SFH is 11×10^7 for the SFRD and 19×10^7 for the sSFR. A good agreement from Prospector and EAZY is reached when deriving the SMD, as we already pointed out looking at Figure 4.13. The stellar mass therefore seems to be the most robust quantity to systematic differences in the modelling, since it has the smallest scattering and best agreement between Prospector and EAZY.

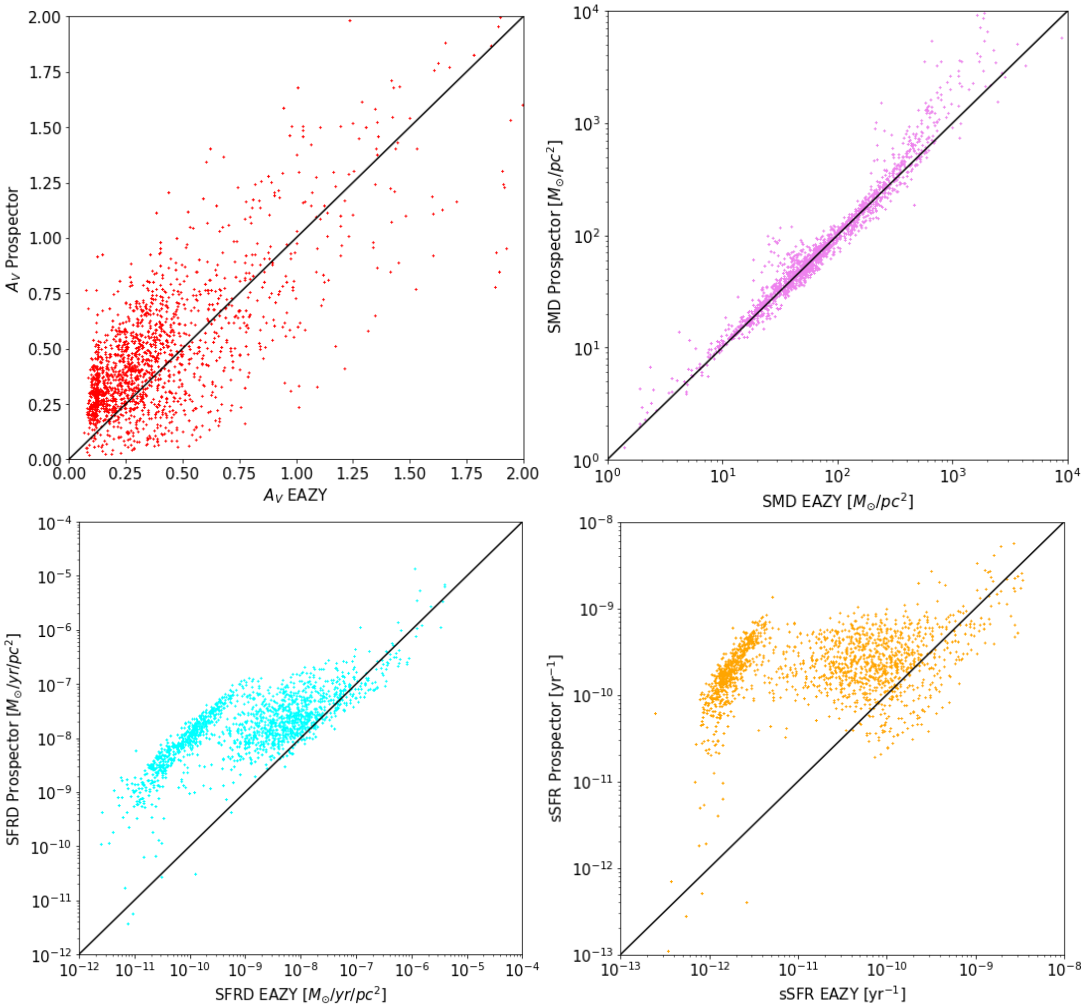

Figure 4.16: Scatter plots showing the relation between the derived quantities with the parametric SFH run of Prospector versus EAZY. The solid black line shows the 1:1 relation between each parameter.

4.4.2 Non-Parametric SFH

After the comparison between EAZY and the Prospector parametric SFH, we can now conduct the same study but running Prospector with a non-parametric SFH. As we have previously mentioned, non-parametric SFH are much more flexible and could be potentially preferable for our sample, since parametric SFH such as exponentially declining models do not allow events like merger driven starbursts. On the other hand, non-parametric SFH models could handle that quite trivially, by having a tau model everywhere in the galaxy except in the burst in star formation that happens due to a merger.

We derive the same physical properties of IRASF10038-3338 as with the previous setting. The calculations to obtain the stellar mass density (SMD), the star formation rate density (SFRD) and the specific star formation rate (sSFR) are the same as for the parametric SFH run. Figure 4.17 shows all the results. We can see that we obtain almost the same results as for the parametric SFH run of Prospector (at least visually). Both EAZY and Prospector achieve similar results. The centre of the galaxy reaches higher values of SMD and SFRD for Prospector than for EAZY, whereas the A_V and sSFR appear to be higher for EAZY. Overall, once again these two fitting schemes seem consistent, at least in the visual inspection.

Now we perform a quantitative analysis between Prospector, with a non-parametric SFH, and EAZY. Figure 4.18 shows the different scatter plots for the physical properties derived with both methods. The results are quite similar to those shown in Figure 4.16, for the parametric SFH run of Prospector. All panels indicate that Prospector systematically overestimates all quantities, when compared to EAZY. A_V and SMD appear as the better matching properties, whereas SFRD and sSFR show considerable discrepancy and dispersion.

To further the quantitative analysis between the different fitting techniques, we calculate the median and dispersion for each quantity ratio, where the ratio is between the EAZY derived parameter and the Prospector one. To also study the difference between the parametric and non-parametric SFH run of Prospector, we investigate the ratio between the two. Table 4.1 shows these results.

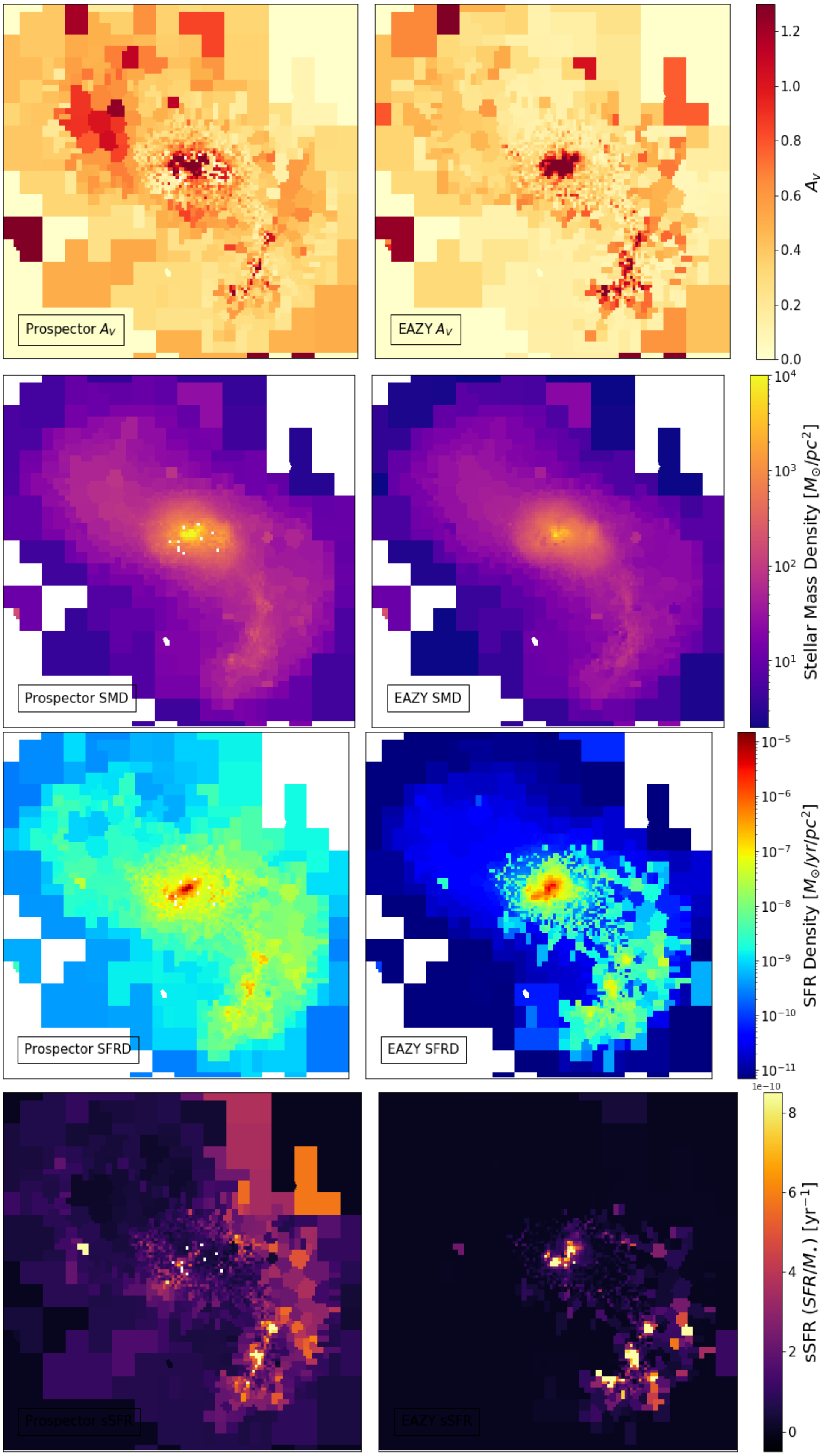

Figure 4.17: Comparison between various derived physical properties obtained with the non-parametric SFH Prospector (left) versus EAZY (right) for IRASF10038-3338.

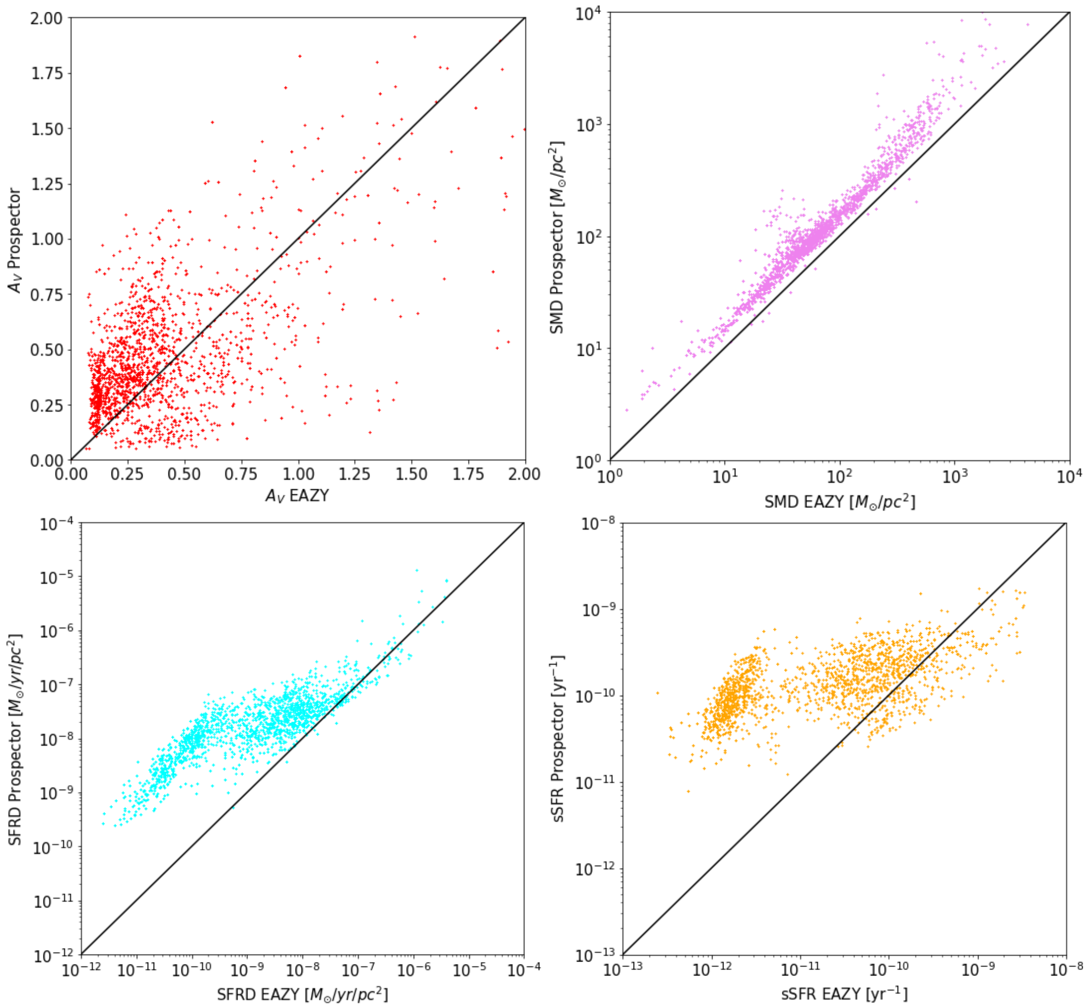

Figure 4.18: Scatter plots showing the relation between the derived quantities with the non-parametric SFH run of Prospector versus EAZY. The solid black line shows the 1:1 relation between each parameter.

	EAZY/P_{PSFH}		EAZY/P_{NPSFH}		P_{PSFH}/P_{NPSFH}	
	median	σ	median	σ	median	σ
A_V	0.57	0.52	0.63	1.09	1.10	0.43
SMD	0.90	0.19	0.61	0.16	0.70	0.22
SFRD	0.015	11e7	0.016	0.22	0.98	0.66
sSFR	0.016	19e7	0.0255	0.50	1.50	1.15

Table 4.1: Values of the median and sigma of different ratios for various derived physical properties using distinct SED-fitting schemes. P_{PSFH} and P_{NPSFH} represent the parametric and non-parametric SFH runs of Prospector, respectively.

Table 4.1 confirms what we have seen in Figures 4.16 and 4.18. Prospector systematically overestimates all properties with respect to EAZY. Looking at the median ratios that compare both SED-fitting methods, we see that the best match is obtained for A_V and SMD. With the parametric SFH (P$_{PSFH}$ hereafter), the A_V Prospector value is 75% higher than for EAZY, whereas for the non-parametric SFH (P$_{NPSFH}$ hereafter), it is only 58% higher. For the stellar mass density (SMD), we obtain better EAZY-Prospector correspondence with P$_{PSFH}$ than with P$_{NPSFH}$. We can also observe that the dispersion for both of these quantities, A_V and SMD, are quite low, with values as small as 0.1 for the P$_{NPSFH}$ case. A very distinct scenario can be found when comparing EAZY and Prospector derivations of the SFRD and sSFR. The median ratios are very similar, around 0.01 for SFRD and 0.02 for sSFR, both for P$_{PSFH}$ and P$_{NPSFH}$. Here we find the biggest difference between P$_{PSFH}$ and P$_{NPSFH}$. For sSFR for example, the P$_{PSFH}$ σ is 19×10^7, whereas for P$_{NPSFH}$ is only 0.5. We also confirm this discrepancy when looking at the last two columns of the table, and seeing that for sSFR, the P$_{PSFH}$ median is 50% higher than for P$_{NPSFH}$, and the deviation is the highest between these two runs of Prospector for all physical properties. Focusing on these last two columns, we see that the best match is obtained for SFRD, with the P$_{NPSFH}$ median being only 2% higher than the P$_{NPSFH}$ median value. These results suggest that both ways of running Prospector match to a good measure, and the quantity that differs the most is the sSFR.

For a given set of observations with a modest S/N, if you try to model the stellar populations, two of the parameters that are most degenerate generally speaking are age and reddening. If one of our fitting methods infers less dust, the reddening would then be attributed to age, so this method would predict much older stellar populations. Given other properties being equal, if we have a high age for a given SED, the SFR would be lower than for younger populations. Therefore, if a model infers less dust, we obtain older age and low SFR. Our plots show that the stellar mass estimates are quite robust and independent of the modelling. Therefore, for a given stellar mass, if we calculate low SFR then the sSFR will also be lower. All this discussion can explain the differences we see between both Prospector runs and the EAZY fitting, particularly in the outskirts of the SFRD and sSFR maps. If for some reason EAZY is biased at "low" S/N (of the outskirts, compared to the high S/N in the centre), it could be favouring older stellar populations at the expense of lower dust (we also see lower continuum A_V inferred by EAZY), therefore giving low SFR and sSFR, particularly in the outskirts. This can explain the results we obtain in our study, and would imply that the Prospector estimates are more likely to be correct.

The results from both Prospector runs on the first target - IRASF10038-3338 - suggest that EAZY and Prospector do not match to a good measure so that EAZY can substitute the Prospector modelling. EAZY and Prospector only appear to match significantly in the bulge of the galaxy. Prospector consistently predicts higher values for all quantities when compared with EAZY. On top of this, Prospector can provide trustworthy uncertainties of the derived physical properties, but with a substantial computational cost. EAZY runs in a matter of seconds/minutes for each galaxy, whereas Prospector can take around a week per galaxy.

4.5 Photometry at Different Scales

So far in this work, we have been taking advantage of the high spatial resolution of our photometric measurements to improve our understanding of dust in galaxies. In this last section we want to study how the resolution of our observations affects our results. and how we can use the well-resolved galaxies here to better interpret measurements at higher redshifts where the galaxies will be only marginally or completely unresolved. With our sample we are able to examine the spatial distribution of different derived physical properties. Some of these properties add up linearly, such as the star formation rate (SFR), so that if we want to calculate the total SFR of the whole galaxy we just need to sum the SFR derived for each bin. This is also the case for the stellar mass (SM hereafter). These two quantities are vital to our understanding of galaxy formation and evolution, hence the importance of obtaining accurate determinations for both.

To quantify the impact of having spatially resolved photometry, we will simulate a mock photometric catalogue. The idea is that common photometric catalogues, such as COSMOS (Laigle *et al.*, 2016), have one integrated flux measurement per available band per galaxy, instead of having a full spatial distribution of the flux for each filter as we have. To achieve this, for every galaxy of our sample, we integrate the fluxes of all bins for each available filter. We also sum the errors (propagating accordingly). The result is one flux measurement per observed band per galaxy, such as for a photometric catalogue. Then we feed this measurement into EAZY[2] to derive the stellar

[2]EAZY was developed with this use in mind.

mass and the SFR of the whole galaxy. After this, we can compare these values with the spatially resolved ones, derived by applying EAZY on all bins instead of just one integrated measurement.

We start this study with the NGC1482 galaxy. If we fit with EAZY the spatially resolved flux measurements, and then sum the SFR and SM of all bins, we obtain $M_{sr} = 2.1 \times 10^{10} M_{\odot}$ and $SFR_{sr} = 1.3 M_{\odot}/yr$, where sr stands for "spatially resolved". If we instead consider only one measurement per available filter (therefore we use as subscript "1"), and fit EAZY to it, the derived physical properties are $M_1 = 1.3 \times 10^{10} M_{\odot}$ and $SFR_1 = 1.8 M_{\odot}/yr$. We can see that for NGC1482, taking one single measurement overestimates the SFR by 33% and underestimates the stellar mass by 66%, compared to having spatially resolved measurements.

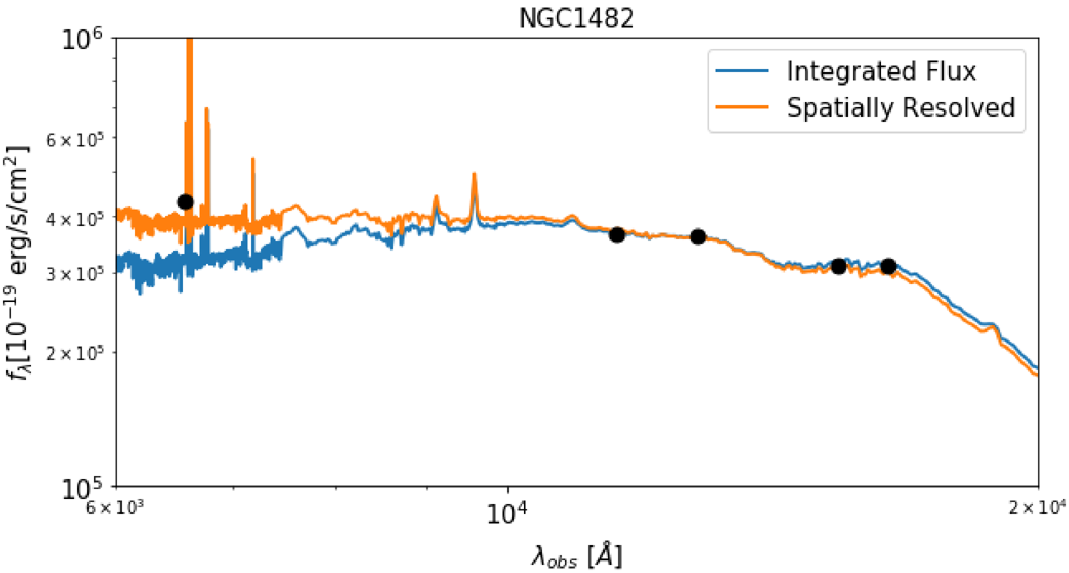

Figure 4.19: Fitted SEDs for NGC1482. The orange and blue SEDs show the fitting done on the spatially resolved and unresolved cases respectively. The black points depict the measurements.

We can also compare the fitted output SED for one measurement versus the summed SED of all bins. Figure 4.19 shows this comparison. The blue curve is for the integrated single measurement, whereas the orange SED is the sum of the fit for all bins. Our measurements that are fitted are shown as solid black points in Figure 4.19. Around these points we can see that both SEDs match in spectral features such as absorption and emission lines, but differ in integrated luminosity. The orange curve, corresponding to the resolved flux measurements, appears to be brighter until $\lambda_{obs} \sim 1.4\mu$m, where the blue SED surpasses it. These variances in the SEDs lead to different derived values for the stellar mass and the SFR of the galaxy.

We now seek to extend this study to our full catalogue. We follow the same procedure as for NGC1482, and use EAZY to obtain the SM and SFR for both photometric types of measuring. Table 4.2 shows the results. It also includes the ratio between the properties derived for each type of measuring, to be able to compare them quantitatively.

Galaxy	M_{sr}	SFR_{sr}	M_1	SFR_1	$\frac{M_{sr}}{M_1}$	$\frac{SFR_{sr}}{SFR_1}$
arp220	6.0×10^{10}	2.0	7.3×10^{10}	6.5	0.8	0.3
eso338-ig004	2.4×10^{9}	2.2	8.7×10^{8}	3.2	2.7	0.7
eso550-ig025	7.9×10^{10}	13.3	7.6×10^{10}	22.6	1.0	0.6
irasf10038-3338	3.5×10^{10}	4.7	3.1×10^{10}	2.5	1.1	1.9
iras03582+6012	5.5×10^{10}	6.5	5.2×10^{10}	2.1	1.1	3.2
iras05223+1908	4.5×10^{11}	27.3	4.5×10^{11}	48.2	1.0	0.6
iras08355-4944	1.5×10^{11}	22.0	9.0×10^{10}	19.6	1.6	1.1
iras12116-5615	1.8×10^{12}	106.7	7.7×10^{11}	104.1	2.3	1.0
iras13120-5453	4.4×10^{11}	36.1	2.0×10^{11}	0.4	2.2	92.3
iras18090+0130	3.6×10^{11}	26.7	3.6×10^{11}	96.0	1.0	0.3
iras23436+5257	1.2×10^{11}	14.5	9.5×10^{10}	10.1	1.3	1.4
irasf16164-0746	3.0×10^{10}	4.5	2.8×10^{10}	4.5	1.1	1.0
irasf16399-0937	1.5×10^{11}	11.6	9.1×10^{10}	11.7	1.6	1.0
mcg-02-01-051	3.3×10^{10}	14.2	2.4×10^{10}	14.7	1.4	1.0
mcg+00-29-023	5.4×10^{10}	14.3	9.5×10^{9}	38.6	5.7	0.4
mcg+12-02-001	4.4×10^{10}	6.6	1.9×10^{10}	23.0	2.3	0.3
ngc0253	6.0×10^{9}	0.1	1.0×10^{10}	0.0	0.6	20.0
ngc1140	1.1×10^{9}	1.0	1.7×10^{9}	1.1	0.6	1.0
ngc1396	4.1×10^{8}	0.0	1.2×10^{8}	0.0	3.5	149.3
ngc1482	2.1×10^{10}	1.3	1.3×10^{10}	1.8	1.7	0.8
ngc1614	3.9×10^{10}	13.3	1.7×10^{10}	13.5	2.4	1.0
ngc2146	1.9×10^{10}	0.7	1.2×10^{10}	0.2	1.5	4.0
ngc2551	1.5×10^{10}	1.3	2.7×10^{09}	11.4	5.5	0.1
ngc2623	2.5×10^{10}	2.4	2.2×10^{10}	6.1	1.2	0.4
ngc2681	1.0×10^{9}	2.0	7.8×10^{8}	2.5	1.3	0.8
ngc2841	1.1×10^{10}	0.1	1.3×10^{10}	0.3	0.9	0.3
ngc2985	1.4×10^{10}	2.5	4.1×10^{9}	7.5	3.3	0.3
ngc3358	4.3×10^{10}	12.6	4.5×10^{11}	0.3	0.1	47.1
ngc3738	7.0×10^{7}	0.0	7.3×10^{7}	0.0	1.0	43.4
ngc4038	1.8×10^{10}	3.0	4.3×10^{9}	8.0	4.1	0.4
ngc4214	2.3×10^{8}	0.1	1.8×10^{8}	0.2	1.3	0.6
ngc5128	5.5×10^{10}	0.8	2.4×10^{10}	1.6	2.2	0.5

Galaxy	M_{sr}	SFR_{sr}	M_1	SFR_1	$\frac{M_{sr}}{M_1}$	$\frac{SFR_{sr}}{SFR_1}$
ngc5256	6.3×10^{10}	20.5	6.2×10^{10}	23.9	1.0	0.9
ngc5331	1.2×10^{11}	9.9	1.0×10^{11}	7.5	1.1	1.3
ngc6090	3.7×10^{10}	15.7	3.0×10^{10}	19.8	1.2	0.8
ngc6217	7.9×10^{9}	2.1	7.1×10^{9}	2.8	1.1	0.7
ngc6240	2.0×10^{11}	28.7	1.6×10^{11}	50.6	1.3	0.6
ngc6670	7.6×10^{10}	12.7	4.5×10^{10}	29.1	1.7	0.4
ngc6690	4.6×10^{8}	0.1	2.0×10^{8}	0.2	2.3	0.4
ngc6786	1.0×10^{11}	22.3	1.3×10^{11}	11.1	0.8	2.0
ngc6951	2.7×10^{10}	1.9	6.4×10^{10}	0.0	0.4	117.6
ngc7090	3.3×10^{9}	0.5	2.6×10^{9}	0.0	1.3	117.3
ngc7592	2.7×10^{10}	19.1	1.4×10^{10}	47.1	2.0	0.4
pgc4798	4.8×10^{10}	17.3	6.7×10^{10}	0.8	0.7	20.9
sdss-j110501.98	2.4×10^{10}	12.5	3.1×10^{10}	6.1	0.8	2.0
sdss-j172823.84	8.3×10^{9}	4.2	2.0×10^{10}	7.3	0.4	0.6
sdss220141.64	6.3×10^{10}	7.0	1.3×10^{10}	0.1	4.7	114.9
ugc5626	3.9×10^{8}	0.4	1.6×10^{9}	0.0	0.2	487.6
vv340a	1.4×10^{11}	14.7	9.8×10^{10}	16.4	1.4	0.9

Table 4.2: Values for stellar masses (in units of solar masses) and SFR (in solar masses per year) for all galaxies in our survey. These were derived by fitting the spatially resolved images (subscript sr) versus a mock photometric catalogue (subscript 1). The last two columns show the ratio between them.

Analysing Table 4.2, we see noticeable agreement for some galaxies. One of these is IRASF16164-0746, for which $M_{sr} = 3.03 \times 10^{10} M_{\odot}$ and $SFR_{sr} = 4.48 M_{\odot}/yr$, whereas $M_1 = 2.83 \times 10^{10} M_{\odot}$ and $SFR_1 = 4.52 M_{\odot}/yr$. Therefore, taking one photometric measurement alone of the galaxy yields only a 7% lower stellar mass and overestimates the SFR just by 1%. For this galaxy, we can see that the SEDs for both measuring techniques match considerably well (top panel in Figure 4.20). Another example of matching derived physical properties is galaxy NGC5256. The corresponding ratios are M_{sr}/M_1=1.02 and SFR_{sr}/SFR_1=0.86. The lower panel of Figure 4.20 shows how well both SEDs match, as we expected since the ratios are very close to 1.

On the other hand, Table 4.2 mostly shows considerable discrepancy between both photometric measuring techniques. Take for example galaxy NGC3358, which for a non-resolved photometric catalogue would appear to have a stellar mass of $M_1 = 4.51 \times 10^{10} M_{\odot}$, whereas with our measurements it yields $M_{sr} = 4.27 \times 10^{10} M_{\odot}$. The resolved case derives only 9% of the mass from

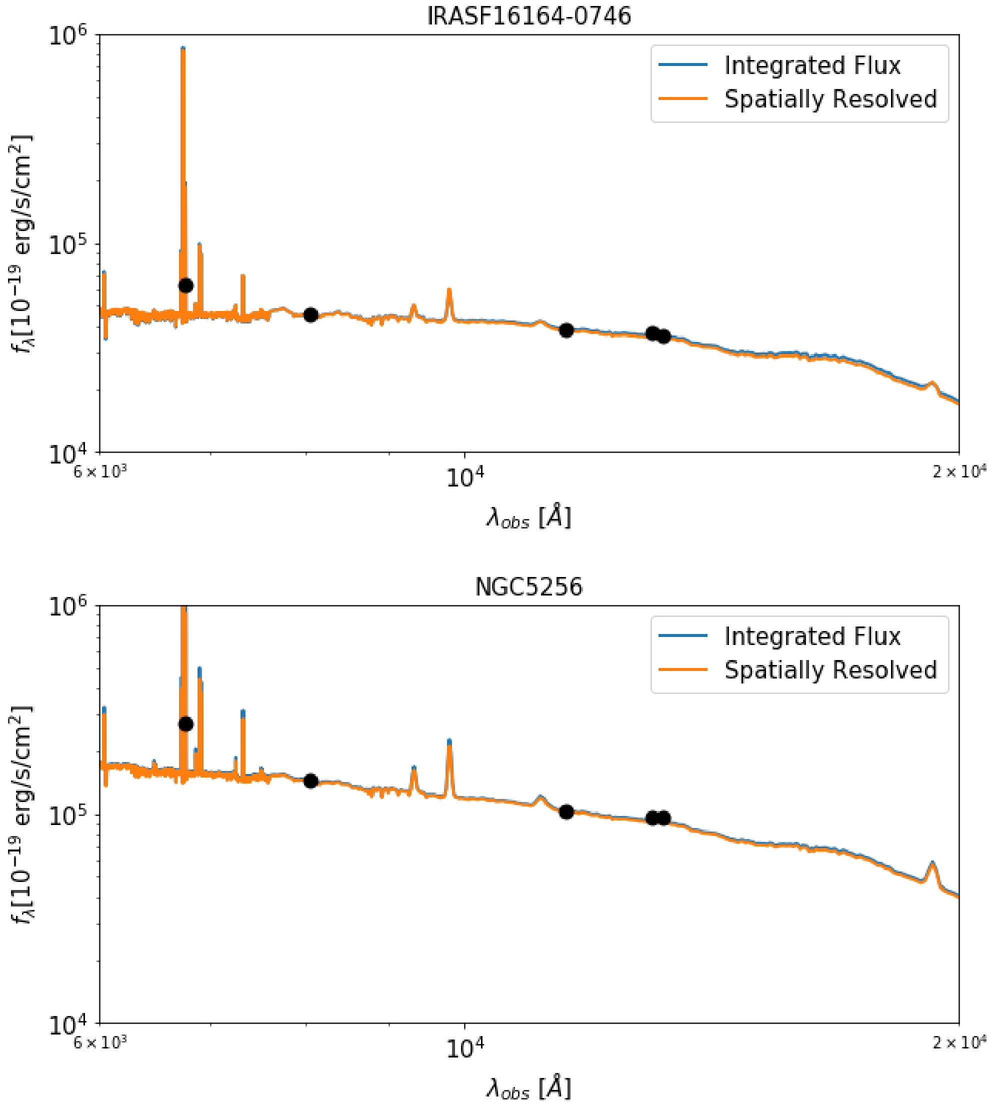

Figure 4.20: Fitted SEDs for multiple galaxies. The blue SED shows the fitting done on one measurement for the whole galaxy, whereas the orange curve represents the spatially resolved SED fit. The black points depict the measurements for both cases.

the non-resolved photometry. The star formation rate discrepancy is even larger, with a ratio of SFR_{sr}/SFR_1=47.12. As expected, the SEDs for this galaxy do not agree well, as we can see in the top panel of Figure 4.21. The lower panel shows NGC6951. From the SEDs alone, we expect very different derived physical parameters, since the curves do not match. If we look at Table 4.2, we find M_{sr}/M_1=0.42 and SFR_{sr}/SFR_1=117.63, which reflect the great discrepancy that we anticipated.

The rest of the SED comparisons for the whole sample can be found in the Appendix (section 8.2). Even though the ratios vary considerably from galaxy

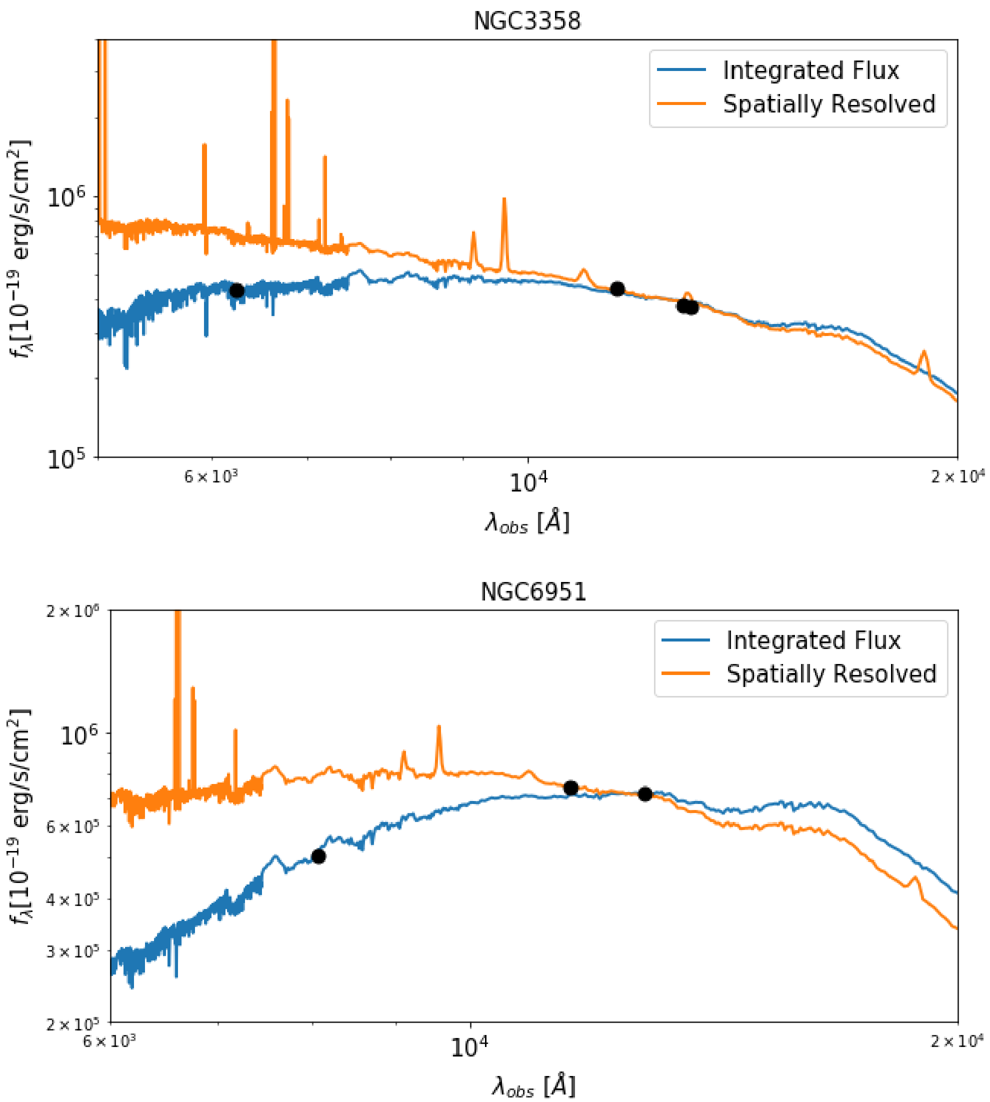

Figure 4.21: Fitted SEDs for multiple galaxies. The blue SED shows the non-resolved photometric case and the orange the resolved one. The black points depict the measurements for both cases.

to galaxy, we want to calculate the median and standard deviation, to get an idea of how the different photometric measurements would affect our survey. For the stellar mass, we obtain a median ratio of $[M_{sr}/M_1]_{median}$=1.27 and $\sigma_M = 1.23$. For the SFR we get $[SFR_{sr}/SFR_1]_{median}$=0.90 and $\sigma_{SFR} = 75.95$. This means that, on average, non-resolved SFRs vary quite significantly, while stellar mass estimates agree better with the resolved case. From the median calculations we see that the resolved photometry obtains 27% higher stellar mass than the non-resolved. On the other hand, non-resolved photometry overestimates the SFR in 10% with respect to the spatially resolved measurements. The standard deviation gives us an idea of how wide the distribution of discrepancies is. We see that for SM it is quite small, only 1.23. On the contrary, the ratios for SFR span a wide range in our galaxies, therefore $\sigma_{SFR} = 75.95$.

To generalise the tabulated entries, we can explore how the ratios between masses and SFRs vary in a relative sense, for the spatially resolved and unresolved cases. We present these results on Figure 4.22. On the left panel we can see that the spatially resolved case marginally predicts higher stellar masses than the non-resolved case, with the ratio being seemingly independent of the stellar mass. The ratios are relatively tightly scattered within 0.5 dex, with a very low density of outliers beyond that. The right panel presents the same comparison for the SFRs, however now the spatially resolved case appears to predict consistently lower SFRs compared to the non-resolved case at all values of SFR. The scatter of the points has increased by a factor of 3 compared to the distribution of the stellar mass ratios, and has also gained a significant number of outliers where the spatially resolved case predicts SFRs 100 times larger than the non-resolved scenario.

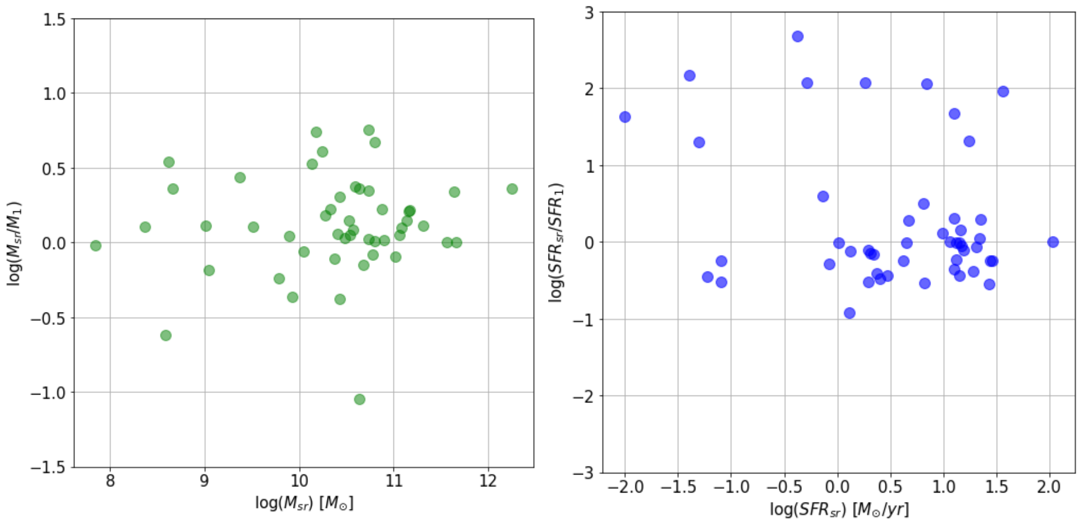

Figure 4.22: Plot of the ratios between masses and SFRs for the spatially resolved and unresolved cases, as a function of M and SFR for the resolved case.

We can also display how the SFR depends on the stellar mass. Figure 4.23 shows the SFR versus the mass, obtained for the spatially resolved measurements. The solid black line represents the main sequence (MS), as calculated in Whitaker *et al.*, 2012, for a redshift of 0.02, which is the median of our sample. The grey shaded region surrounding the solid black line shows the same calculation performed with the minimum and maximum redshifts of our sample instead. The dashed black lines correspond to 3 times above and below the main sequence. These limits are supposed to separate starbursts (3 times above the MS) and quiescent galaxies (3 times below) from the MS galaxies. We can see that a high number of our galaxies are undergoing starbursts, most likely driven by mergers, since we can see paired galaxies in our HST images. Only two galaxies appear to be quiescent as inferred from the SFR and M of the EAZY fitting, the rest are contained within the main sequence or above. This is also what we would expect for the GOALS sample selection criteria. If we instead use the non-resolved SFR and M to construct this plot, Figure 4.23 would appear essentially unchanged, however the points would be more scattered.

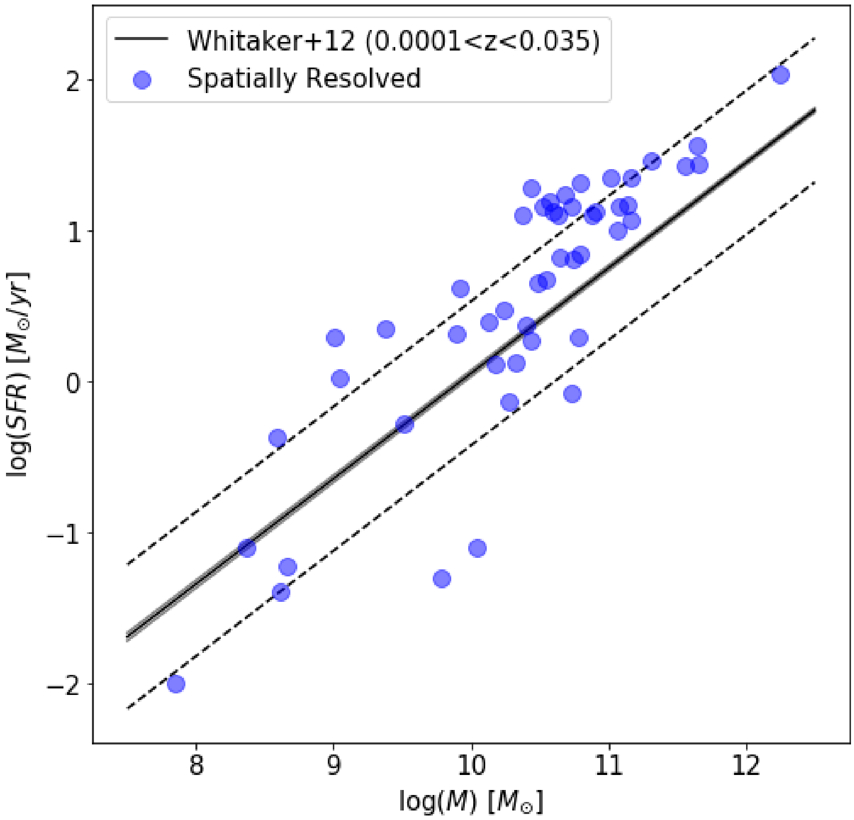

Figure 4.23: Position of the Dusty Cosmos sample relative to the Main Sequence of star formation.

Now we can perform a final check on our SFR estimates. First, we compare values inferred by EAZY to what we can consider as the "true" SFR, that we compute from the total infrared luminosity (L_{IR}) that is available for galaxies in the GOALS sample as seen in Table 2.1. We convert the L_{IR} to SFR by multiplying it by a factor of 10^{-10} [$M_\odot$ yr^1 $L_\odot^{-1}$] (Kennicutt, 1998), and also apply a 1.8 correction factor to our EAZY SFRs in order to account for the difference in the IMF. We present the resultant plot on the left panel of Figure 4.24. It appears that the two will generally fall on the 1:1 relation, thus confirming that EAZY SFR estimates are robust and compare well to the SFR obtained from the unobscured part of the spectrum.

We can also infer the SFR from the emission lines. In order to do so we use the following equation:

$$\mathrm{SFR}[\mathrm{M_{\odot}yr^{-1}}] = 7.9 \times 10^{-42}\, \mathrm{L(H\alpha)}\, [\mathrm{erg\,s^{-1}}] \tag{4.1}$$

which allows us to estimate SFR directly from the Hα luminosity (Kennicutt, 1998). We can also infer the SFR from the L(Paβ) instead, however, in this case we would need to factor in the intrinsic ratio between the two lines - 17.56 - thus obtaining:

$$\mathrm{SFR}[\mathrm{M_{\odot}yr^{-1}}] = 7.9 \times 10^{-42} \times\ 17.56 \times \mathrm{L(Pa\beta)}\, [\mathrm{erg\,s^{-1}}]. \tag{4.2}$$

The results of these calculations can be found on Figure 4.24 in the middle and right panels. We seem to consistently underestimate the SFR with both emission lines, and this effect is more strongly pronounced in the case of Hα. This could be explained by the fact that the Hα emission is bluer than the Paβ line and is thus more affected by dust extinction, leading to lower predicted SFRs.

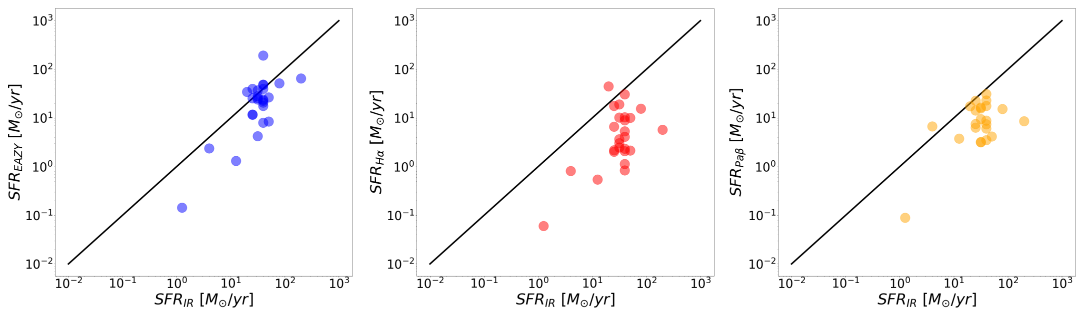

Figure 4.24: SFR scatter plots inferred with different methods.

The results obtained in this last study suggest that observing our sample with spatially resolved photometry yields considerably different derived physical properties - in this case the stellar mass and SFR - compared to non-resolved photometric observations.

5 Future Perspectives

Our high-resolution observations have a lot of potential for further studies. As an example, here we introduce two lines of research that could profit from our sample:

1. We could degrade the resolution and the signal-to-noise ratio of our images to simulate observations of high redshift galaxies. We could thus test the reliability of the dust screen model employed in most SED-fitting codes used to recover the intrinsic stellar population properties.

2. Current cosmological simulations are starting to resolve scales where the dust and stars geometry is crucial for determining the light emergence from galaxies. To link the simulations to real observations, mock HST images are created assuming certain reddening laws. To create these mock images, one must make assumptions about feedback and its impact on dust and gas. We currently have poor knowledge on how this feedback affects the interstellar medium of galaxies. The Hα/Paβ extinction maps that we have obtained, can provide direct constraints on such cosmological models.

In addition to our current sample, further observations of new targets would enrich the archival Hα+Paβ dataset for nearby galaxies, making it more valuable for comparative studies across infrared luminosities, morphological types, star-formation histories and more.

6 Conclusions

In this work, we have used hydrogen recombination lines to derive extinction maps with resolution $\sim$50 pc for a large sample of nearby star-forming galaxies. Our data was obtained with the Hubble Space Telescope, targeting the Hα and Paβ emission lines. We have tested the ability of the Hα/Paβ ratio to trace the obscuration of gas in galaxies. Other extinction derivation methods, such as SED-fitting, fail to produce robust results at high redshifts. On the contrary, the use of recombination lines could work well for galaxies at high redshift, providing reliable constraints of the dust obscuration in these distant systems. From the extinction maps that we derive in this work, we learn that most of our galaxies are undergoing mergers, visible in the bright Hα and Paβ emissions. Additionally, they have high dust content, particularly in the centre of each galaxy.

We have been able to infer the extinction from the nebular lines and from the overall continuum shape. This allows us to test whether the diffuse interstellar medium is the only source of extinction in our galaxies. First, we investigate this for a single object (NGC1482) where we see the need to account for extra attenuation due to birth clouds. When we extend our study to the whole sample, we obtain the same result. In order to provide a better prescription of the dust content in galaxies, one must acknowledge and include the attenuation from birth clouds as well as the diffuse ISM.

In our analysis, we have also confirmed that the location on a *UVJ* diagram relates to direct extinction measurements. The *UVJ* diagram proved to be valuable to study different levels of extinction, as well as separating star-forming from quiescent galaxies. At the same time, we have connected this study with the comparison between A_V continuum and A_V gas. Both works seem to agree and point towards the need to account for extra attenuation in dusty regions surrounding birth clouds.

Parallel to our study, a team from Tufts University in Boston has been running the SED-fitting code Prospector to derive physical parameters of the sample. We have compared their results to EAZY, a different method to model SEDs of galaxies. The results of the comparison on a first target - IRASF10038-3338 - indicate that the match is not substantial so that EAZY can substitute the Prospector modelling. Prospector consistently predicts higher values for all quantities when compared with EAZY. On top of this, Prospector can provide trustworthy uncertainties of the derived local physical properties.

As a final investigation, we have studied how the resolution of observations affects the derived physical properties. Common photometric catalogues provide one flux measurement per band per target, whereas we have full spatially-resolved flux measurements for each filter and galaxy. Our results suggest that the resolution has a significant impact on the estimated galaxy properties. For our sample with spatially-resolved photometry, we derive considerably different physical properties compared to non-resolved photometric observations. This could have significant repercussions on current research in extragalactic astronomy, since it suggests that the stellar mass and SFR estimates in large surveys could be unreliable and far from the actual values.

Bibliography 7

Anders, P. and U. Fritze-v. Alvensleben (Apr. 2003). „Spectral and photometric evolution of young stellar populations: The impact of gaseous emission at various metallicities“. In: *Astronomy and Astrophysics* 401, pp. 1063–1070. arXiv: astro-ph/0302146 [astro-ph].

Armus, L., J. M. Mazzarella, A. S. Evans, *et al.* (June 2009). „GOALS: The Great Observatories All-Sky LIRG Survey“. In: *The Publications of the Astronomical Society of the Pacific* 121.880, p. 559. arXiv: 0904.4498 [astro-ph.CO].

Astropy Collaboration, A. M. Price-Whelan, B. M. Sipőcz, *et al.* (Sept. 2018). „The Astropy Project: Building an Open-science Project and Status of the v2.0 Core Package“. In: *Astronomical Journal* 156.3, 123, p. 123. arXiv: 1801.02634 [astro-ph.IM].

Astropy Collaboration, Thomas P. Robitaille, Erik J. Tollerud, *et al.* (Oct. 2013). „Astropy: A community Python package for astronomy“. In: *Astronomy & Astrophysics* 558, A33, A33. arXiv: 1307.6212 [astro-ph.IM].

Atek, H., B. Siana, C. Scarlata, *et al.* (Dec. 2011). „Very Strong Emission-line Galaxies in the WFC3 Infrared Spectroscopic Parallel Survey and Implications for High-redshift Galaxies“. In: *The Astrophysical Journal* 743.2, 121, p. 121. arXiv: 1109.0639 [astro-ph.CO].

Bianchi, Luciana, Geoffrey C. Clayton, Ralph C. Bohlin, J. B. Hutchings, and Philip Massey (Nov. 1996). „Ultraviolet Extinction by Interstellar Dust in External Galaxies: M31“. In: *The Astrophysical Journal* 471, p. 203.

Bohr, Niels (1913). „On the Constitution of Atoms and Molecules, Part I“. In: *Philosophical Magazine* 26 (151), pp. 1–24.

Boroson, T. (June 1981). „The distribution of luminosity in spiral galaxies.“ In: *Astrophysical Journal, Suppl. Ser.* 46, pp. 177–209.

Brammer, G. B., K. E. Whitaker, P. G. van Dokkum, *et al.* (Nov. 2009). „The Dead Sequence: A Clear Bimodality in Galaxy Colors from z = 0 to z = 2.5“. In: *ApJ Letters* 706.1, pp. L173–L177. arXiv: 0910.2227 [astro-ph.CO].

Brammer, Gabriel B., Pieter G. van Dokkum, and Paolo Coppi (Oct. 2008). „EAZY: A Fast, Public Photometric Redshift Code“. In: *The Astrophysical Journal* 686.2, pp. 1503–1513. arXiv: 0807.1533 [astro-ph].

Calzetti, D., R. C. Kennicutt, C. W. Engelbracht, *et al.* (Sept. 2007). „The Calibration of Mid-Infrared Star Formation Rate Indicators“. In: *The Astrophysical Journal* 666.2, pp. 870–895. arXiv: 0705.3377 [astro-ph].

Calzetti, D., S. -Y. Wu, S. Hong, *et al.* (May 2010). „The Calibration of Monochromatic Far-Infrared Star Formation Rate Indicators“. In: *The Astrophysical Journal* 714.2, pp. 1256–1279. arXiv: 1003.0961 [astro-ph.CO].

Calzetti, Daniela (Jan. 1997). „Reddening and Star Formation in Starburst Galaxies“. In: 113, pp. 162–184. arXiv: astro-ph/9610184 [astro-ph].

Calzetti, Daniela (2013). „Star Formation Rate Indicators“. In: *Secular Evolution of Galaxies*. Ed. by Jesús Falcón-Barroso and Johan H. Knapen, p. 419.

Calzetti, Daniela, Lee Armus, Ralph C. Bohlin, Anne L. Kinney, Jan Koornneef, and Thaisa Storchi-Bergmann (Apr. 2000). „The Dust Content and Opacity of Actively Star-forming Galaxies“. In: *The Astrophysical Journal* 533.2, pp. 682–695. arXiv: astro-ph/9911459 [astro-ph].

Calzetti, Daniela, Anne L. Kinney, and Thaisa Storchi-Bergmann (July 1994). „Dust Extinction of the Stellar Continua in Starburst Galaxies: The Ultraviolet and Optical Extinction Law“. In: *The Astrophysical Journal* 429, p. 582.

Cappellari, Michele and Yannick Copin (June 2003). „Adaptive spatial binning of integral-field spectroscopic data using Voronoi tessellations“. In: *Monthly Notices of the Royal Astronomical Society* 342.2, pp. 345–354. arXiv: astro-ph/0302262 [astro-ph].

Cardelli, J. A., G. C. Clayton, and J. S. Mathis (Dec. 1989). „The relationship between IR, optical, and UV extinction.“ In: *Interstellar Dust*. Ed. by Louis J. Allamandola and A. G. G. M. Tielens. Vol. 135. IAU Symposium, pp. 5–10.

Chevallard, Jacopo, Emma Curtis-Lake, Stéphane Charlot, *et al.* (Feb. 2019). „Simulating and interpreting deep observations in the Hubble Ultra Deep Field with the JWST/NIRSpec low-resolution ‘prism’“. In: *Monthly Notices of the Royal Astronomical Society* 483.2, pp. 2621–2640. arXiv: 1711.07481 [astro-ph.GA].

Ciesla, L., D. Elbaz, and J. Fensch (Dec. 2017). „The SFR-M_* main sequence archetypal star-formation history and analytical models“. In: *Astronomy & Astrophysics* 608, A41, A41. arXiv: 1706.08531 [astro-ph.GA].

Conroy, Charlie (Aug. 2013). „Modeling the Panchromatic Spectral Energy Distributions of Galaxies“. In: *Annual Review of Astronomy and Astrophysics* 51.1, pp. 393–455. arXiv: 1301.7095 [astro-ph.CO].

Conroy, Charlie, Genevieve J. Graves, and Pieter G. van Dokkum (Jan. 2014). „Early-type Galaxy Archeology: Ages, Abundance Ratios, and Effective Temperatures from Full-spectrum Fitting“. In: *The Astrophysical Journal* 780.1, 33, p. 33. arXiv: 1303.6629 [astro-ph.CO].

Conroy, Charlie and James E. Gunn (Apr. 2010). „The Propagation of Uncertainties in Stellar Population Synthesis Modeling. III. Model Calibration, Comparison, and Evaluation“. In: *The Astrophysical Journal* 712.2, pp. 833–857. arXiv: 0911.3151 [astro-ph.CO].

Conroy, Charlie, James E. Gunn, and Martin White (July 2009). „The Propagation of Uncertainties in Stellar Population Synthesis Modeling. I. The Relevance of Uncertain Aspects of Stellar Evolution and the Initial Mass Function to the Derived Physical Properties of Galaxies“. In: *The Astrophysical Journal* 699.1, pp. 486–506. arXiv: 0809.4261 [astro-ph].

De Marchi, Guido and Nino Panagia (Nov. 2014). „The extinction law inside the 30 Doradus nebula“. In: *Monthly Notices of the Royal Astronomical Society* 445.1, pp. 93–106. arXiv: 1408.4786 [astro-ph.SR].

Draine, B. T. (2009). „Interstellar Dust Models and Evolutionary Implications“. In: *Cosmic Dust - Near and Far*. Ed. by T. Henning, E. Grün, and J. Steinacker. Vol. 414. Astronomical Society of the Pacific Conference Series, p. 453.

Dumas, G., E. Schinnerer, F. S. Tabatabaei, R. Beck, T. Velusamy, and E. Murphy (Feb. 2011). „The Local Radio-IR Relation in M51“. In: *The Astronomical Journal* 141.2, 41, p. 41. arXiv: 1012.0212 [astro-ph.CO].

Fang, Jerome J., S. M. Faber, David C. Koo, *et al.* (May 2018). „Demographics of Star-forming Galaxies since z 2.5. I. The UVJ Diagram in CANDELS“. In: *The Astrophysical Journal* 858.2, 100, p. 100. arXiv: 1710.05489 [astro-ph.GA].

Ferland, G. J., K. T. Korista, D. A. Verner, J. W. Ferguson, J. B. Kingdon, and E. M. Verner (July 1998). „CLOUDY 90: Numerical Simulation of Plasmas and Their Spectra“. In: *The Publications of the Astronomical Society of the Pacific* 110.749, pp. 761–778.

Fitzpatrick, Edward L. (Jan. 1999). „Correcting for the Effects of Interstellar Extinction“. In: *The Publications of the Astronomical Society of the Pacific* 111.755, pp. 63–75. arXiv: astro-ph/9809387 [astro-ph].

Gao, Jian, Aigen Li, and B. W. Jiang (Oct. 2013). „Modeling the infrared extinction toward the galactic center“. In: *Earth, Planets, and Space* 65.10, pp. 1127–1132. arXiv: 1305.7137 [astro-ph.GA].

Gordon, Karl D., Geoffrey C. Clayton, K. A. Misselt, Arlo U. Land olt, and Michael J. Wolff (Sept. 2003). „A Quantitative Comparison of the Small Magellanic Cloud, Large Magellanic Cloud, and Milky Way Ultraviolet to Near-

Infrared Extinction Curves". In: *The Astrophysical Journal* 594.1, pp. 279–293. arXiv: astro-ph/0305257 [astro-ph].

Graham, James R., D. P. Carico, K. Matthews, G. Neugebauer, B. T. Soifer, and T. D. Wilson (May 1990). „The Double Nucleus of ARP 220 Unveiled". In: *Astrophysical Journal Letters* 354, p. L5.

Greener, Michael J., Alfonso Aragón-Salamanca, Michael R. Merrifield, *et al.* (May 2020). „SDSS-IV MaNGA: spatially resolved dust attenuation in spiral galaxies". In: *accepted for publication in Monthly Notices of the Royal Astronomical Society*. arXiv: 2005.02772 [astro-ph.GA].

Grogin, Norman A., Dale D. Kocevski, S. M. Faber, *et al.* (Dec. 2011). „CANDELS: The Cosmic Assembly Near-infrared Deep Extragalactic Legacy Survey". In: *The Astrophysical Journal Supplement Series* 197.2, 35, p. 35. arXiv: 1105.3753 [astro-ph.CO].

Groves, Brent A., Michael A. Dopita, and Ralph S. Sutherland (July 2004). „Dusty, Radiation Pressure-Dominated Photoionization. II. Multiwavelength Emission Line Diagnostics for Narrow-Line Regions". In: *The Astrophysical Journal Supplement Series,* 153.1, pp. 75–91. arXiv: astro-ph/0404176 [astro-ph].

Hinshaw, G., D. Larson, E. Komatsu, *et al.* (Oct. 2013). „Nine-year Wilkinson Microwave Anisotropy Probe (WMAP) Observations: Cosmological Parameter Results". In: *The Astrophysical Journal Supplement* 208.2, 19, p. 19. arXiv: 1212.5226 [astro-ph.CO].

Hirashita, Hiroyuki (May 2012). „Dust growth in the interstellar medium: how do accretion and coagulation interplay?" In: *Monthly Notices of the Royal Astronomical Society* 422.2, pp. 1263–1271. arXiv: 1202.1345 [astro-ph.GA].

Hopkins, A. M., A. J. Connolly, D. B. Haarsma, and L. E. Cram (July 2001). „Toward a Resolution of the Discrepancy between Different Estimators of Star Formation Rate". In: *Astronomical Journal* 122.1, pp. 288–296. arXiv: astro-ph/0103253 [astro-ph].

Johnson, Ben and Joel Leja (Dec. 2017). *Bd-J/Prospector: Initial Release*. Version v0.1.

Kennicutt Robert C., Jr. (Jan. 1998). „Star Formation in Galaxies Along the Hubble Sequence". In: *Annual Review of Astronomy and Astrophysics* 36, pp. 189–232. arXiv: astro-ph/9807187 [astro-ph].

Kennicutt, R. C., D. Calzetti, G. Aniano, *et al.* (Dec. 2011). „KINGFISH—Key Insights on Nearby Galaxies: A Far-Infrared Survey with Herschel: Survey Description and Image Atlas". In: *Publications of the Astronomical Society of the Pacific* 123.910, p. 1347. arXiv: 1111.4438 [astro-ph.CO].

Kewley, Lisa J., Margaret J. Geller, Rolf A. Jansen, and Michael A. Dopita (Dec. 2002). „The Hα and Infrared Star Formation Rates for the Nearby Field Galaxy Survey“. In: *Astronomical Journal* 124.6, pp. 3135–3143. arXiv: astro-ph/0208508 [astro-ph].

Kewley, Lisa J., David C. Nicholls, and Ralph S. Sutherland (Aug. 2019). „Understanding Galaxy Evolution Through Emission Lines“. In: *Annual Review of Astronomy and Astrophysics* 57, pp. 511–570. arXiv: 1910.09730 [astro-ph.GA].

Koekemoer, Anton M., S. M. Faber, Henry C. Ferguson, *et al.* (Dec. 2011). „CANDELS: The Cosmic Assembly Near-infrared Deep Extragalactic Legacy Survey—The Hubble Space Telescope Observations, Imaging Data Products, and Mosaics“. In: *The Astrophysical Journal Supplement Series* 197.2, 36, p. 36. arXiv: 1105.3754 [astro-ph.CO].

Laigle, C., H. J. McCracken, O. Ilbert, *et al.* (June 2016). „The COSMOS2015 Catalog: Exploring the 1 < z < 6 Universe with Half a Million Galaxies“. In: *The Astrophysical Journal Supplement Series* 224.2, 24, p. 24. arXiv: 1604.02350 [astro-ph.GA].

Lawrence, A., S. J. Warren, O. Almaini, *et al.* (Aug. 2007). „The UKIRT Infrared Deep Sky Survey (UKIDSS)“. In: *Monthly Notices of the Royal Astronomical Society* 379.4, pp. 1599–1617. arXiv: astro-ph/0604426 [astro-ph].

Leja, Joel, Benjamin D. Johnson, Charlie Conroy, Pieter G. van Dokkum, and Nell Byler (Mar. 2017). „Deriving Physical Properties from Broadband Photometry with Prospector: Description of the Model and a Demonstration of its Accuracy Using 129 Galaxies in the Local Universe“. In: *The Astrophysical Journal* 837.2, 170, p. 170. arXiv: 1609.09073 [astro-ph.GA].

Liu, Guilin, Daniela Calzetti, Sungryong Hong, Bradley Whitmore, Rupali Chandar, Robert W. O’Connell, William P. Blair, Seth H. Cohen, Jay A. Frogel, and Hwihyun Kim (Dec. 2013). „Extinction and Dust Geometry in M83 H II Regions: An Hubble Space Telescope/WFC3 Study“. In: *ApJ Letters* 778.2, L41, p. L41. arXiv: 1311.0871 [astro-ph.CO].

Lupton, Robert, Michael R. Blanton, George Fekete, David W. Hogg, Wil O’Mullane, Alex Szalay, and Nicholas Wherry (Feb. 2004). „Preparing Red-Green-Blue Images from CCD Data“. In: *The Publications of the Astronomical Society of the Pacific* 116.816, pp. 133–137. arXiv: astro-ph/0312483 [astro-ph].

Madau, Piero and Mark Dickinson (Aug. 2014). „Cosmic Star-Formation History“. In: *Annual Review of Astronomy and Astrophysics* 52, pp. 415–486. arXiv: 1403.0007 [astro-ph.CO].

Man, Allison and Sirio Belli (Sept. 2018). „Star formation quenching in massive galaxies“. In: *Nature Astronomy* 2, pp. 695–697. arXiv: `1809.00722 [astro-ph.GA]`.

Marchesini, Danilo, Adam Muzzin, Mauro Stefanon, *et al.* (Oct. 2014). „The Progenitors of Local Ultra-massive Galaxies Across Cosmic Time: From Dusty Star-bursting to Quiescent Stellar Populations“. In: *The Astrophysical Journal* 794.1, 65, p. 65. arXiv: `1402.0003 [astro-ph.GA]`.

McCracken, H. J., B. Milvang-Jensen, J. Dunlop, *et al.* (Aug. 2012). „UltraVISTA: a new ultra-deep near-infrared survey in COSMOS“. In: *Astronomy & Astrophysics* 544, A156, A156. arXiv: `1204.6586 [astro-ph.CO]`.

McLure, R. J., L. Pentericci, A. Cimatti, *et al.* (Sept. 2018). „The VANDELS ESO public spectroscopic survey“. In: *Monthly Notices of the Royal Astronomical Society* 479.1, pp. 25–42. arXiv: `1803.07414 [astro-ph.GA]`.

Momcheva, Ivelina G., Janice C. Lee, Chun Ly, Samir Salim, Daniel A. Dale, Masami Ouchi, Rose Finn, and Yoshiaki Ono (Feb. 2013). „Nebular Attenuation in Hα-selected Star-forming Galaxies at z = 0.8 from the NewHα Survey“. In: *The Astronomical Journal* 145.2, 47, p. 47. arXiv: `1207.5479 [astro-ph.CO]`.

Mortlock, Alice, Ross J. McLure, Rebecca A. A. Bowler, Derek J. McLeod, Esther Mármol-Queraltó, Shaghayegh Parsa, James S. Dunlop, and Victoria A. Bruce (Feb. 2017). „Characterizing the evolving K -band luminosity function using the UltraVISTA, CANDELS and HUDF surveys“. In: *Monthly Notices of the Royal Astronomical Society* 465.1, pp. 672–687. arXiv: `1610.06574 [astro-ph.GA]`.

Muzzin, Adam, Danilo Marchesini, Mauro Stefanon, *et al.* (Nov. 2013). „The Evolution of the Stellar Mass Functions of Star-forming and Quiescent Galaxies to z = 4 from the COSMOS/UltraVISTA Survey“. In: *The Astrophysical Journal* 777.1, 18, p. 18. arXiv: `1303.4409 [astro-ph.CO]`.

Neugebauer, G., H. J. Habing, R. van Duinen, *et al.* (Mar. 1984). „The Infrared Astronomical Satellite (IRAS) mission.“ In: *ApJ Letters* 278, pp. L1–L6.

Oesch, P. A., G. Brammer, P. G. van Dokkum, *et al.* (Mar. 2016). „A Remarkably Luminous Galaxy at z=11.1 Measured with Hubble Space Telescope Grism Spectroscopy“. In: *The Astrophysical Journal* 819.2, 129, p. 129. arXiv: `1603.00461 [astro-ph.GA]`.

Osterbrock, Donald E. (1989). *Astrophysics of gaseous nebulae and active galactic nuclei*. Sausalito CA 94965: University Science Books.

Pang, Xiaoying, Anna Pasquali, and Eva K. Grebel (Oct. 2011). „A Two-dimensional Map of the Color Excess in NGC 3603“. In: *Astronomical Journal* 142.4, 132, p. 132. arXiv: `1108.2032 [astro-ph.GA]`.

Patel, S. G., B. P. Holden, D. D. Kelson, M. Franx, A. van der Wel, and G. D. Illingworth (July 2011). „The UVJ Selection of Quiescent and Star Forming Galaxies: Separating Early and Late-Type Galaxies and Isolating Edge-on Spirals“. In: *Galaxy Formation*, P59.

Patel, S. G., B. P. Holden, D. D. Kelson, M. Franx, A. van der Wel, and G. D. Illingworth (Mar. 2012). „The UVJ Selection of Quiescent and Star Forming Galaxies: Separating Early and Late-Type Galaxies and Isolating Edge-on Spirals“. In: *The Astrophysical Journal* 748.2, p. L27.

Rodrigo, Carlos, Enrique Solano, and Amelia Bayo (Oct. 2012). *SVO Filter Profile Service Version 1.0*. IVOA Working Draft 15 October 2012.

Rosa-González, Daniel, Elena Terlevich, and Roberto Terlevich (May 2002). „An empirical calibration of star formation rate estimators“. In: *Monthly Notices of the Royal Astronomical Society* 332.2, pp. 283–295. arXiv: `astro-ph/0112556 [astro-ph]`.

Sanders, D. B. and I. F. Mirabel (Jan. 1996). „Luminous Infrared Galaxies“. In: *Annual Review of Astronomy and Astrophysics* 34, p. 749.

Schaerer, D. and S. de Barros (June 2010). „On the physical properties of $z \approx 6$-8 galaxies“. In: *Astronomy and Astrophysics* 515, A73, A73. arXiv: `1002.1090 [astro-ph.CO]`.

Schinnerer, Eva, Sharon E. Meidt, Jérôme Pety, *et al.* (Dec. 2013). „The PdBI Arcsecond Whirlpool Survey (PAWS). I. A Cloud-scale/Multi-wavelength View of the Interstellar Medium in a Grand-design Spiral Galaxy“. In: *The Astrophysical Journal* 779.1, 42, p. 42. arXiv: `1304.1801 [astro-ph.CO]`.

Skelton, Rosalind E., Katherine E. Whitaker, Ivelina G. Momcheva, *et al.* (Oct. 2014). „3D-HST WFC3-selected Photometric Catalogs in the Five CANDELS/3D-HST Fields: Photometry, Photometric Redshifts, and Stellar Masses“. In: *The Astrophysical Journal Supplement Series* 214.2, 24, p. 24. arXiv: `1403.3689 [astro-ph.GA]`.

Soifer, B. T., G. Neugebauer, and J. R. Houck (Jan. 1987). „The IRAS view of the extragalactic sky.“ In: *Annual Review of Astronomy and Astrophysics* 25, pp. 187–230.

Spitler, Lee R., Caroline M. S. Straatman, Ivo Labbé, *et al.* (June 2014). „Exploring the $z = 3$-4 Massive Galaxy Population with ZFOURGE: The Prevalence of Dusty and Quiescent Galaxies“. In: *ApJ Letters* 787.2, L36, p. L36. arXiv: `1405.1048 [astro-ph.GA]`.

Springel, Volker, Simon D. M. White, Adrian Jenkins, *et al.* (June 2005). „Simulations of the formation, evolution and clustering of galaxies and quasars“. In: *Nature* 435.7042, pp. 629–636. arXiv: astro-ph/0504097 [astro-ph].

STScI Development Team (Mar. 2013). *pysynphot: Synthetic photometry software package*. ascl: 1303.023.

Sullivan, Mark, Bahram Mobasher, Ben Chan, Lawrence Cram, Richard Ellis, Marie Treyer, and Andrew Hopkins (Sept. 2001). „A Comparison of Independent Star Formation Diagnostics for an Ultraviolet-selected Sample of Nearby Galaxies“. In: *The Astrophysical Journal* 558.1, pp. 72–80. arXiv: astro-ph/0104425 [astro-ph].

Wang, Z., G. G. Fazio, M. L. N. Ashby, J. -S. Huang, M. A. Pahre, H. A. Smith, S. P. Willner, W. J. Forrest, J. L. Pipher, and J. A. Surace (Sept. 2004). „The Off-Nuclear Starbursts in NGC 4038/4039 (The Antennae Galaxies)“. In: *The Astrophysical Journal Supplement Series* 154.1, pp. 193–198. arXiv: astro-ph/0406276 [astro-ph].

Whitaker, Katherine E., Pieter G. van Dokkum, Gabriel Brammer, and Marijn Franx (Aug. 2012). „The Star Formation Mass Sequence Out to z = 2.5“. In: *The Astrophysical Journal Letters* 754.2, L29, p. L29. arXiv: 1205.0547 [astro-ph.CO].

Williams, Rik J., Ryan F. Quadri, Marijn Franx, Pieter van Dokkum, and Ivo Labbé (Feb. 2009). „Detection of Quiescent Galaxies in a Bicolor Sequence from Z = 0-2“. In: *The Astrophysical Journal* 691.2, pp. 1879–1895. arXiv: 0806.0625 [astro-ph].

Williams, Robert E., Brett Blacker, Mark Dickinson, *et al.* (Oct. 1996). „The Hubble Deep Field: Observations, Data Reduction, and Galaxy Photometry“. In: *Astronomical Journal* 112, p. 1335. arXiv: astro-ph/9607174 [astro-ph].

Wu, Po-Feng, Arjen van der Wel, Anna Gallazzi, *et al.* (Mar. 2018). „Stellar Populations of over 1000 z 0.8 Galaxies from LEGA-C: Ages and Star Formation Histories from D_n4000 and Hδ“. In: *The Astrophysical Journal* 855.2, 85, p. 85. arXiv: 1802.06799 [astro-ph.GA].

Wuyts, Stijn, Natascha M. Förster Schreiber, Erica J. Nelson, *et al.* (Dec. 2013). „A CANDELS-3D-HST synergy: Resolved Star Formation Patterns at 0.7 < z < 1.5“. In: *The Astrophysical Journal* 779.2, 135, p. 135. arXiv: 1310.5702 [astro-ph.CO].

Wuyts, Stijn, Ivo Labbé, Marijn Franx, *et al.* (Jan. 2007). „What Do We Learn from IRAC Observations of Galaxies at $2 \leq z \leq 3.5$?“. In: *The Astrophysical Journal* 655.1, pp. 51–65. arXiv: astro-ph/0609548 [astro-ph].

8 Appendix

8.1 Image Results

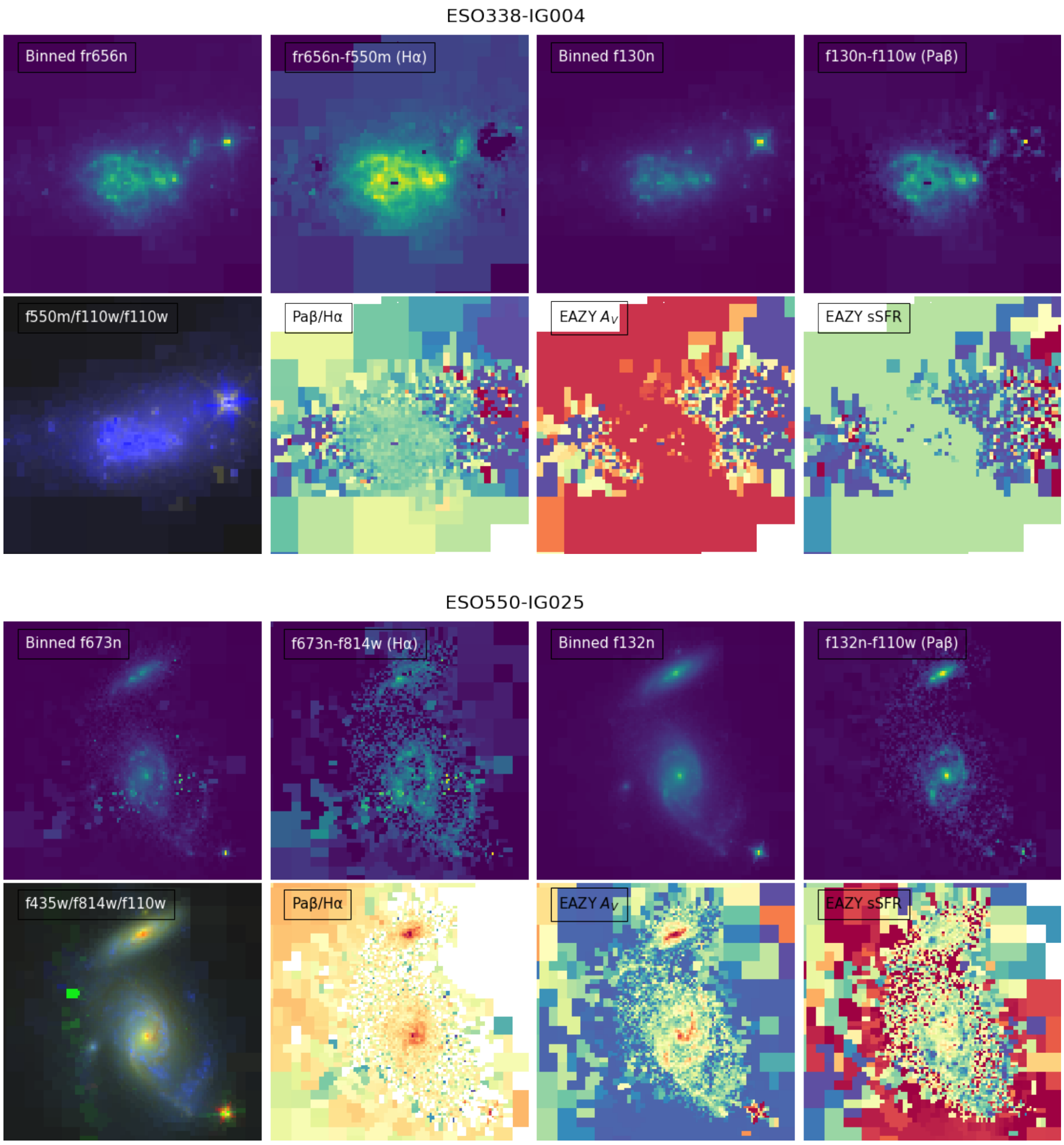

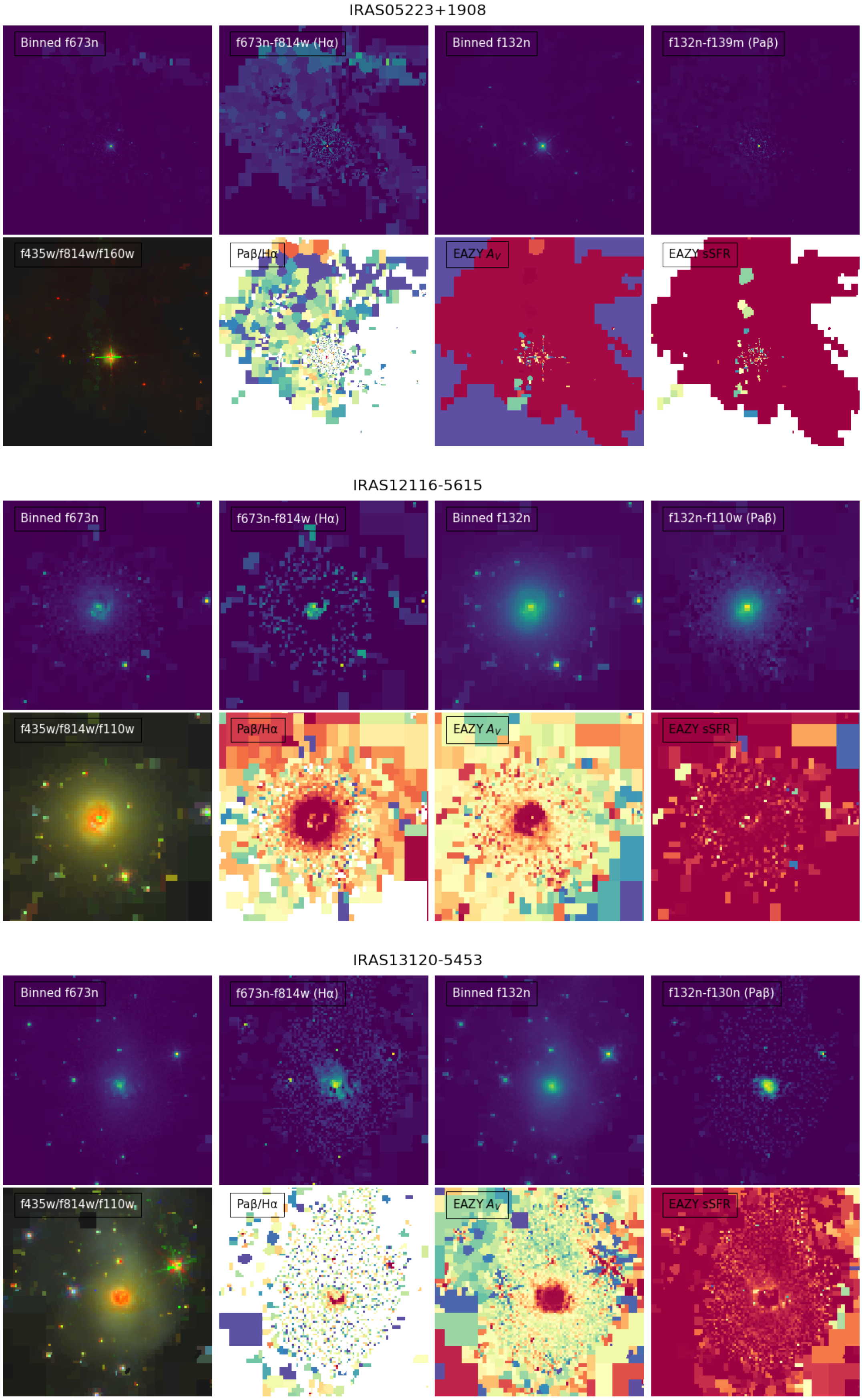
IRAS05223+1908
Binned f673n
f673n-f814w (Hα)
Binned f132n
f132n-f139m (Paβ)
f435w/f814w/f160w
Paβ/Hα
EAZY A_V
EAZY sSFR
IRAS12116-5615
Binned f673n
f673n-f814w (Hα)
Binned f132n
f132n-f110w (Paβ)
f435w/f814w/f110w
Paβ/Hα
EAZY A_V
EAZY sSFR
IRAS13120-5453
Binned f673n
f673n-f814w (Hα)
Binned f132n
f132n-f130n (Paβ)
f435w/f814w/f110w
Paβ/Hα
EAZY A_V
EAZY sSFR

IRAS18090+0130

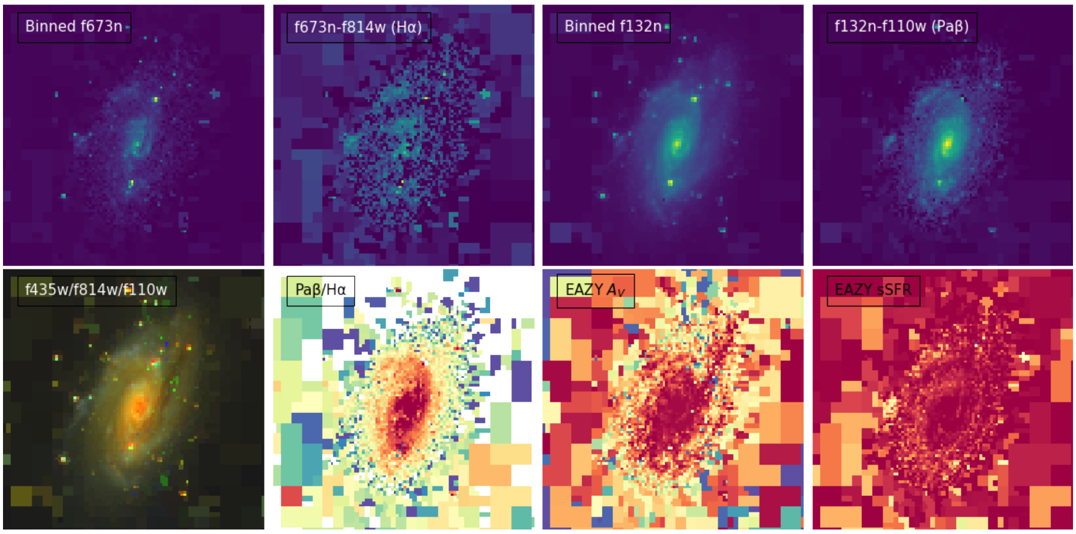

IRAS23436+5257

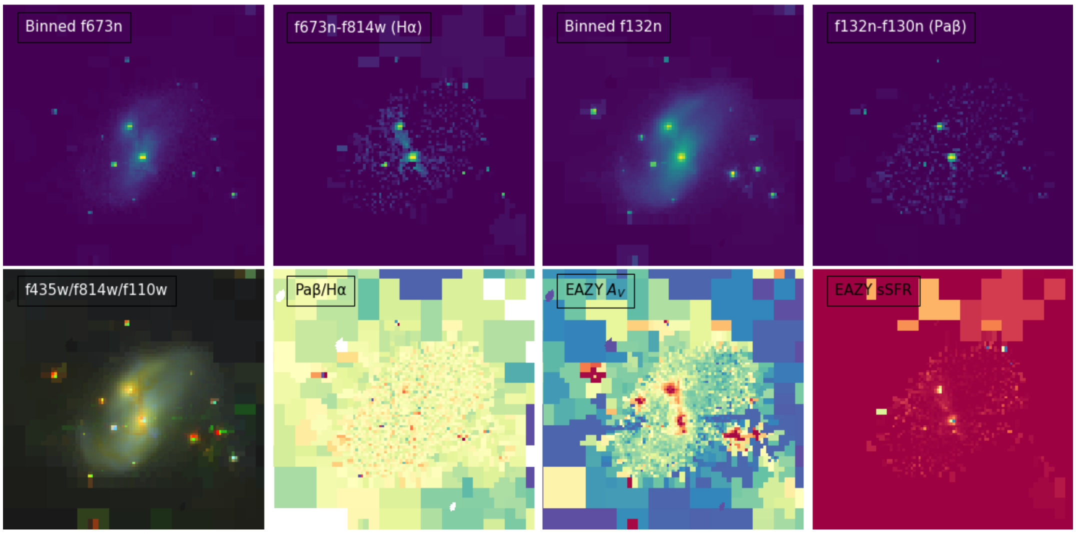

IRASF16164-0746

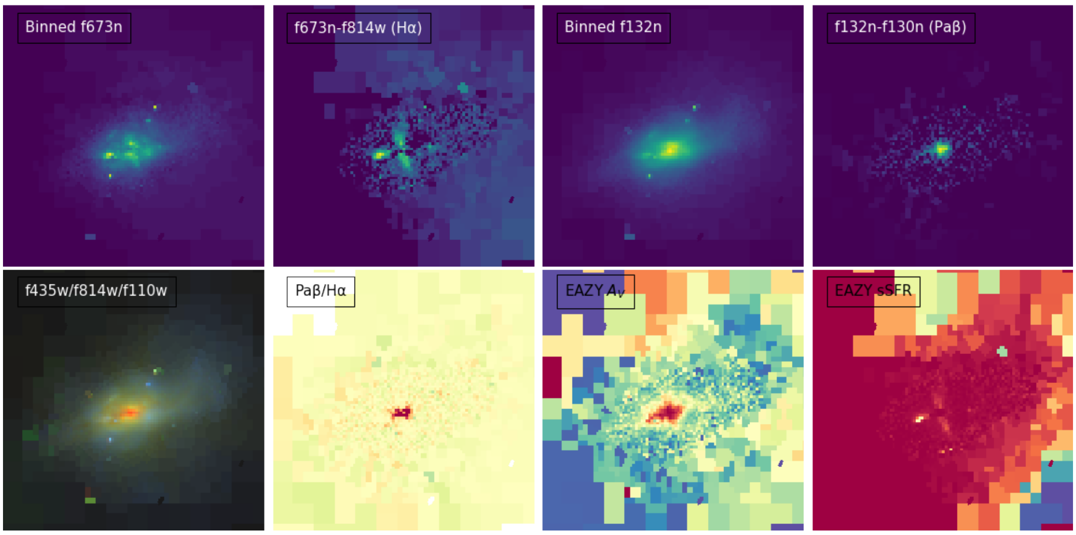

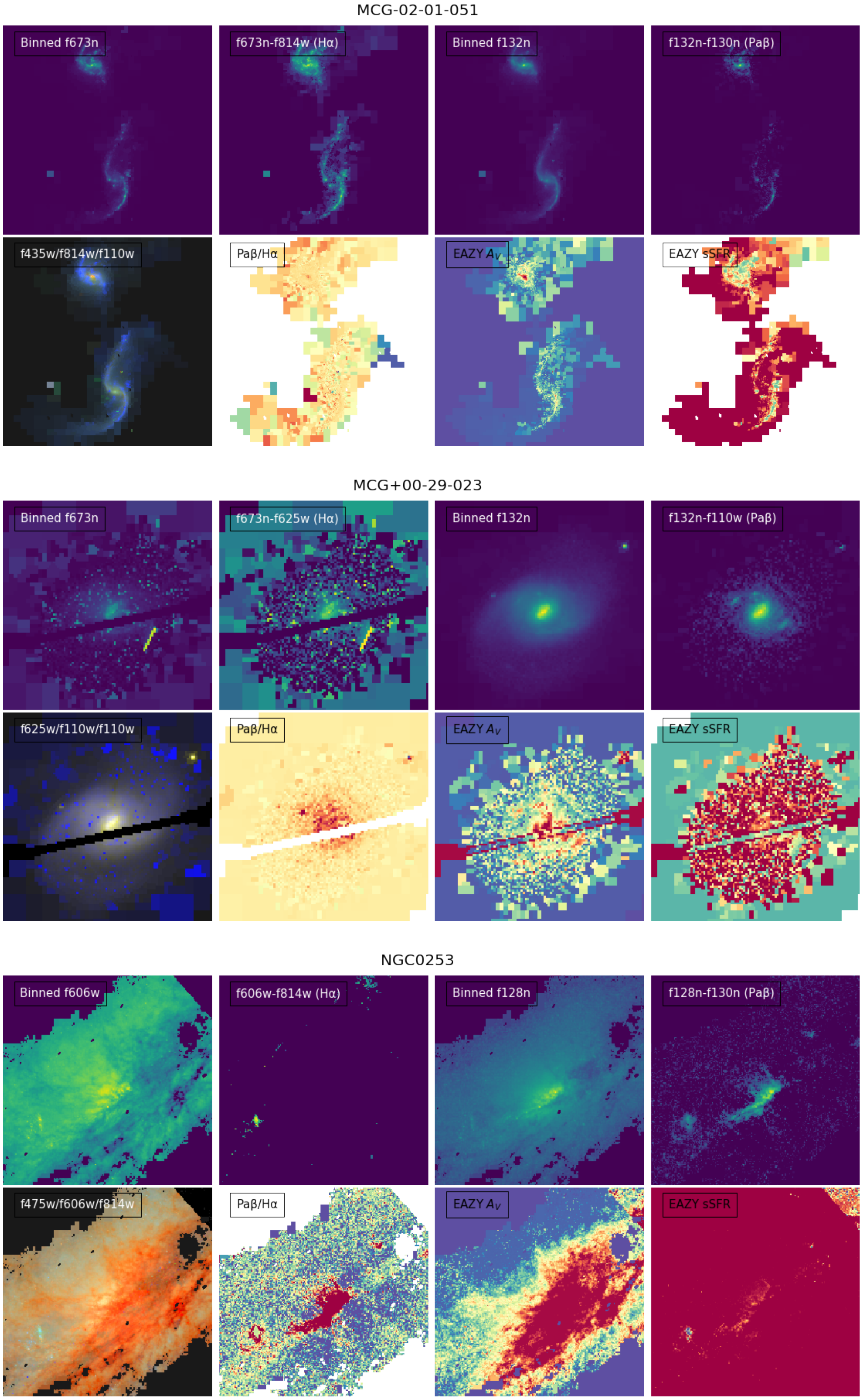
MCG-02-01-051
Binned f673n
f673n-f814w (Hα)
Binned f132n
f132n-f130n (Paβ)
f435w/f814w/f110w
Paβ/Hα
EAZY A_V
EAZY sSFR
MCG+00-29-023
Binned f673n
f673n-f625w (Hα)
Binned f132n
f132n-f110w (Paβ)
f625w/f110w/f110w
Paβ/Hα
EAZY A_V
EAZY sSFR
NGC0253
Binned f606w
f606w-f814w (Hα)
Binned f128n
f128n-f130n (Paβ)
f475w/f606w/f814w
Paβ/Hα
EAZY A_V
EAZY sSFR

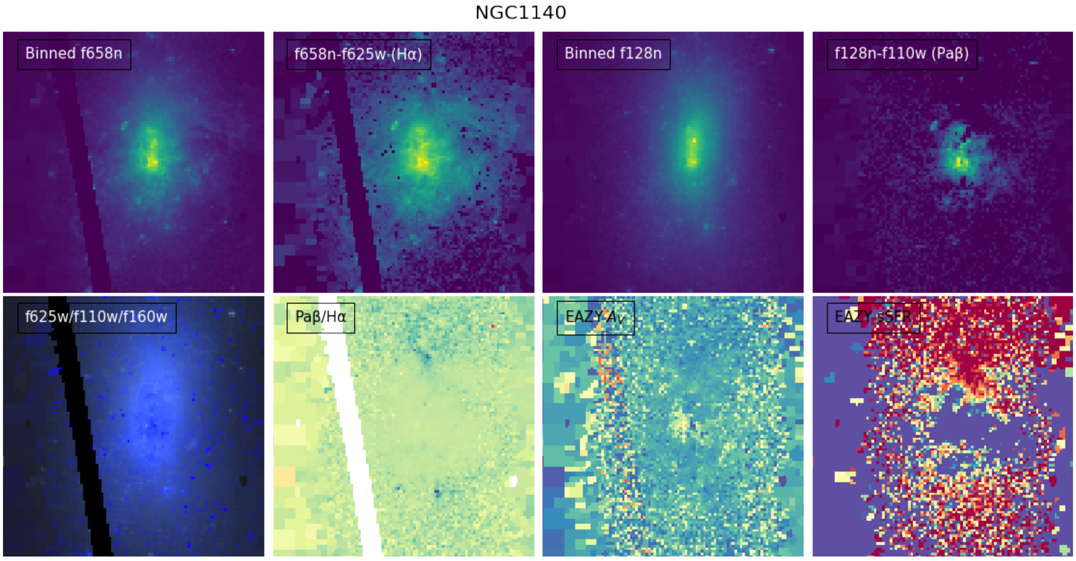
NGC1140
Binned f658n
f658n-f625w (Hα)
Binned f128n
f128n-f110w (Paβ)
f625w/f110w/f160w
Paβ/Hα
EAZY A_V
EAZY sSFR

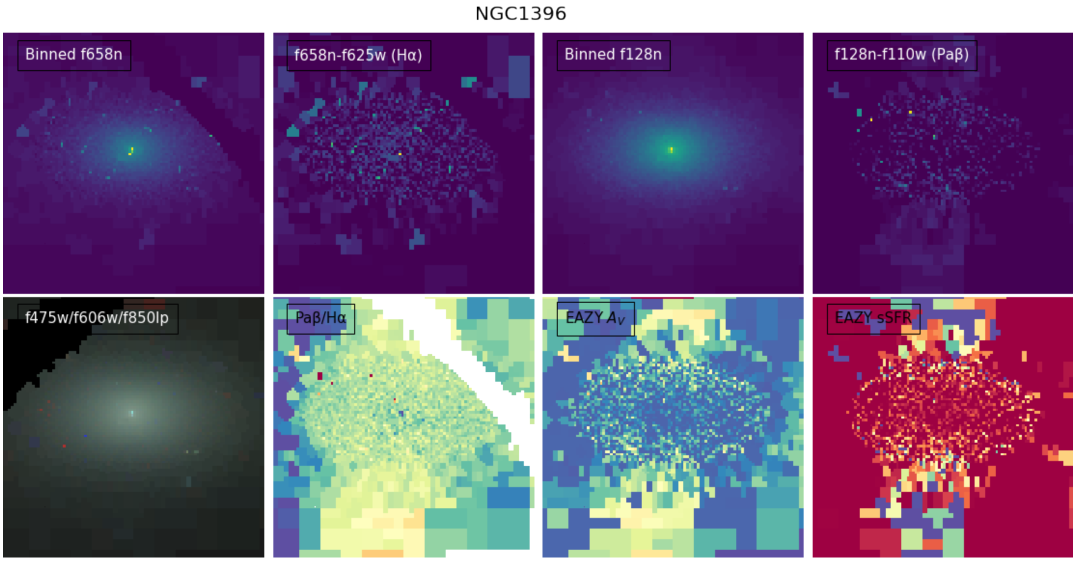
NGC1396
Binned f658n
f658n-f625w (Hα)
Binned f128n
f128n-f110w (Paβ)
f475w/f606w/f850lp
Paβ/Hα
EAZY A_V
EAZY sSFR

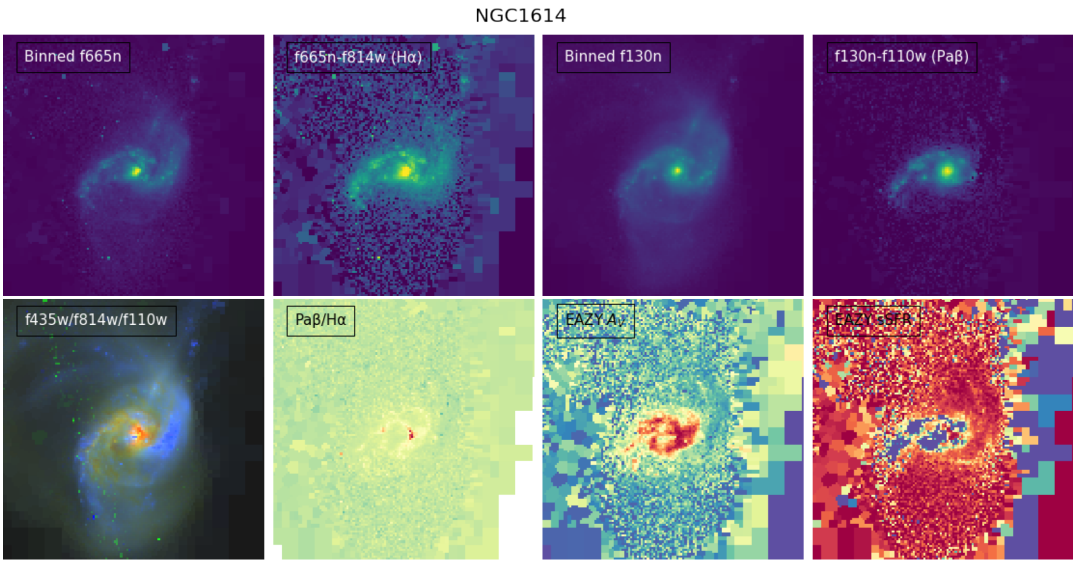
NGC1614
Binned f665n
f665n-f814w (Hα)
Binned f130n
f130n-f110w (Paβ)
f435w/f814w/f110w
Paβ/Hα
EAZY A_V
EAZY sSFR

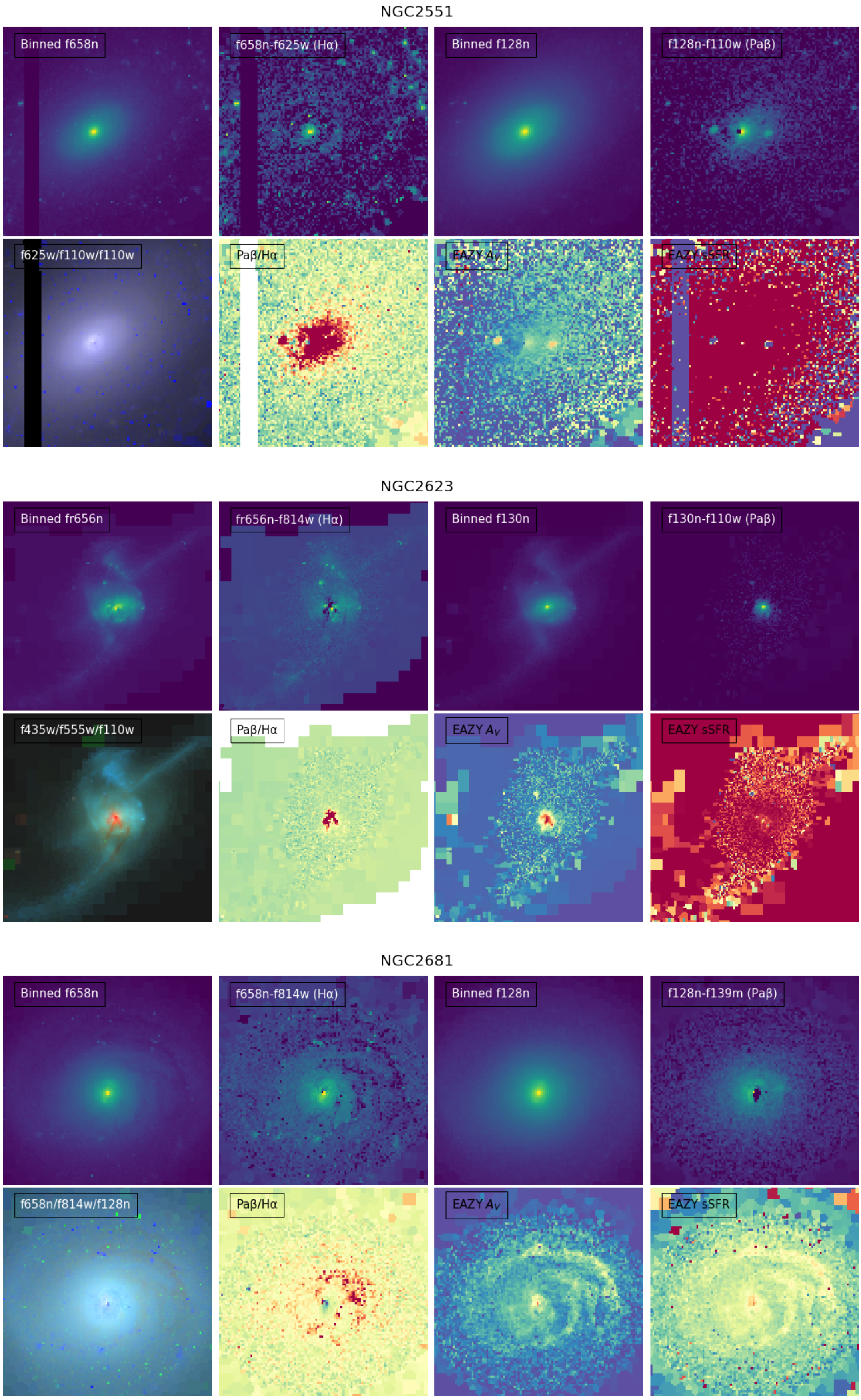
NGC2551
Binned f658n
f658n-f625w (Hα)
Binned f128n
f128n-f110w (Paβ)
f625w/f110w/f110w
Paβ/Hα
EAZY A_V
EAZY sSFR
NGC2623
Binned fr656n
fr656n-f814w (Hα)
Binned f130n
f130n-f110w (Paβ)
f435w/f555w/f110w
Paβ/Hα
EAZY A_V
EAZY sSFR
NGC2681
Binned f658n
f658n-f814w (Hα)
Binned f128n
f128n-f139m (Paβ)
f658n/f814w/f128n
Paβ/Hα
EAZY A_V
EAZY sSFR

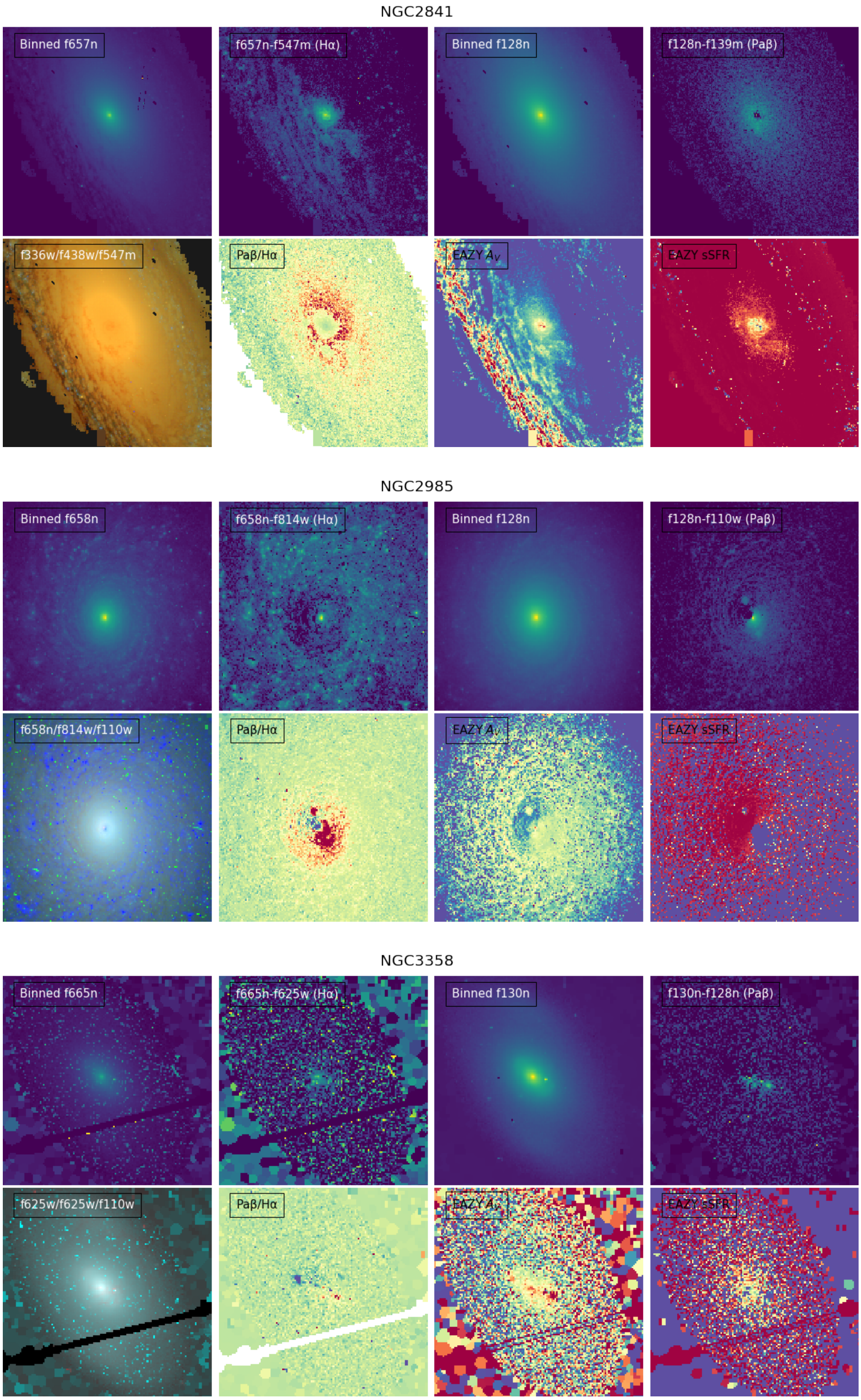

NGC2841
Binned f657n
f657n-f547m (Hα)
Binned f128n
f128n-f139m (Paβ)
f336w/f438w/f547m
Paβ/Hα
EAZY A_V
EAZY sSFR
NGC2985
Binned f658n
f658n-f814w (Hα)
Binned f128n
f128n-f110w (Paβ)
f658n/f814w/f110w
Paβ/Hα
EAZY A_V
EAZY sSFR
NGC3358
Binned f665n
f665n-f625w (Hα)
Binned f130n
f130n-f128n (Paβ)
f625w/f625w/f110w
Paβ/Hα
EAZY A_V
EAZY sSFR

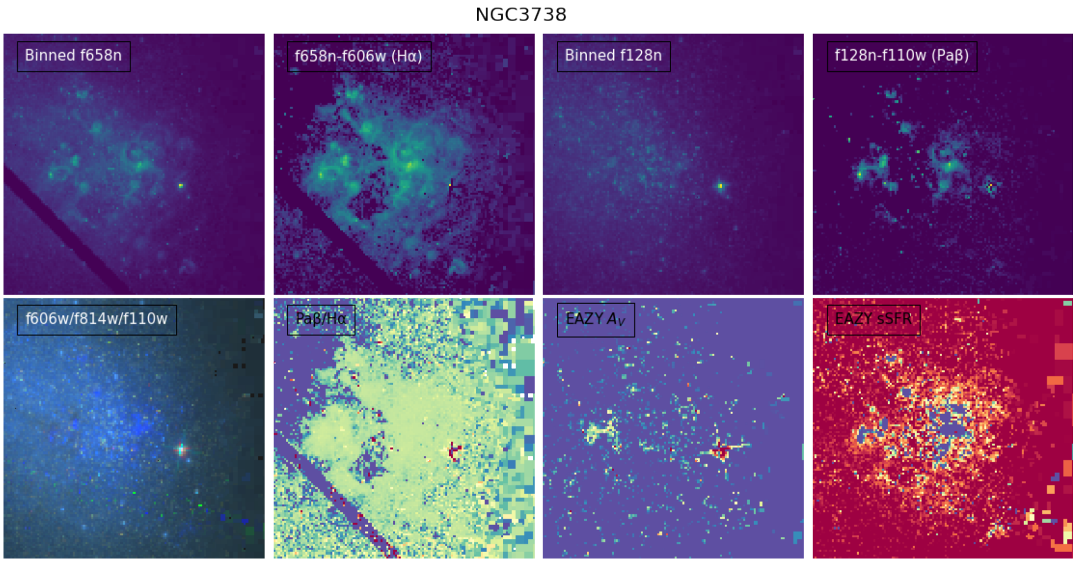
NGC3738
Binned f658n
f658n-f606w (Hα)
Binned f128n
f128n-f110w (Paβ)
f606w/f814w/f110w
Paβ/Hα
EAZY A_V
EAZY sSFR

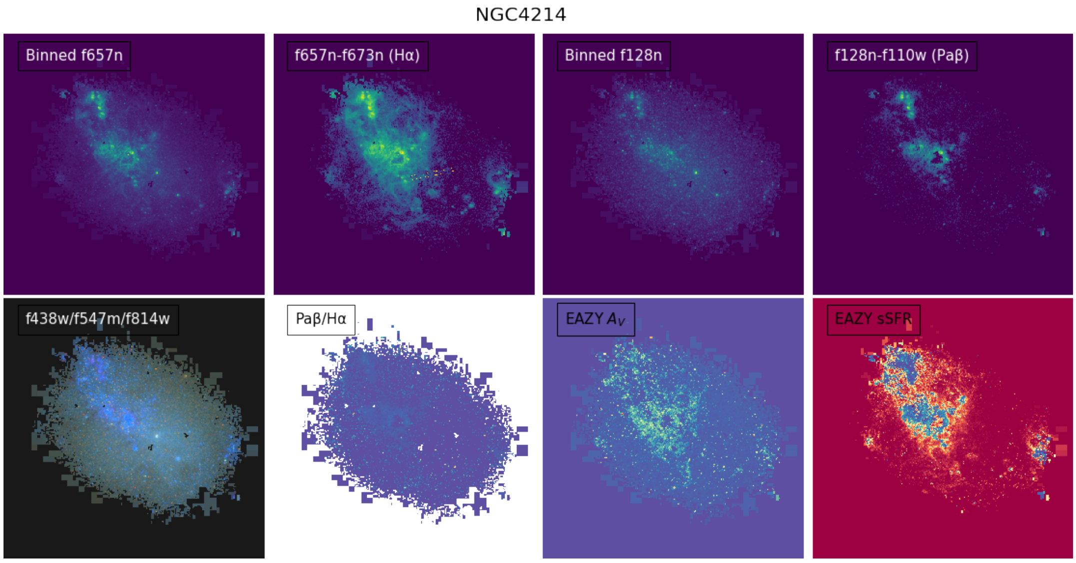
NGC4214
Binned f657n
f657n-f673n (Hα)
Binned f128n
f128n-f110w (Paβ)
f438w/f547m/f814w
Paβ/Hα
EAZY A_V
EAZY sSFR

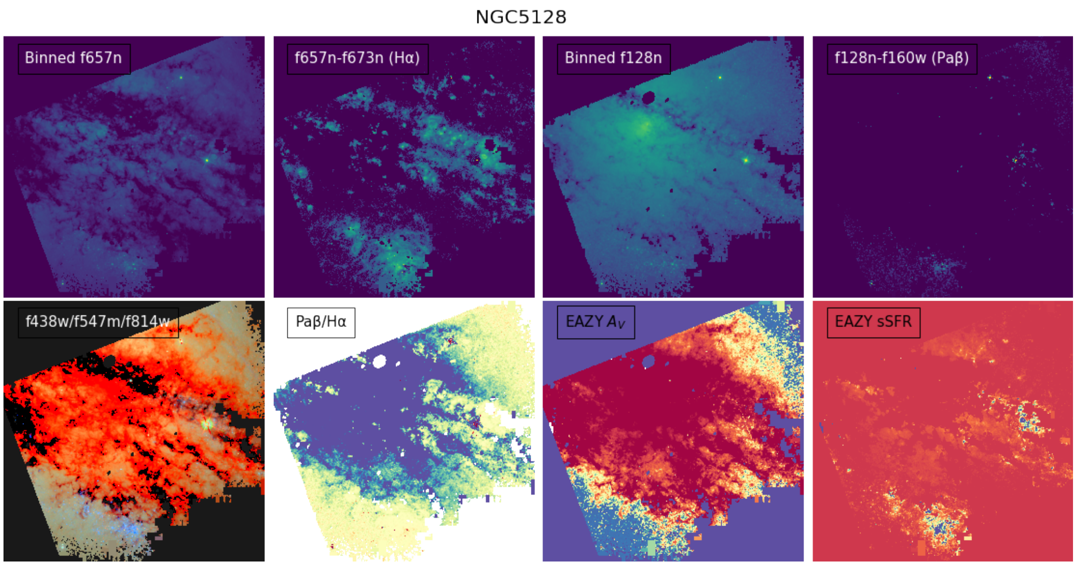
NGC5128
Binned f657n
f657n-f673n (Hα)
Binned f128n
f128n-f160w (Paβ)
f438w/f547m/f814w
Paβ/Hα
EAZY A_V
EAZY sSFR

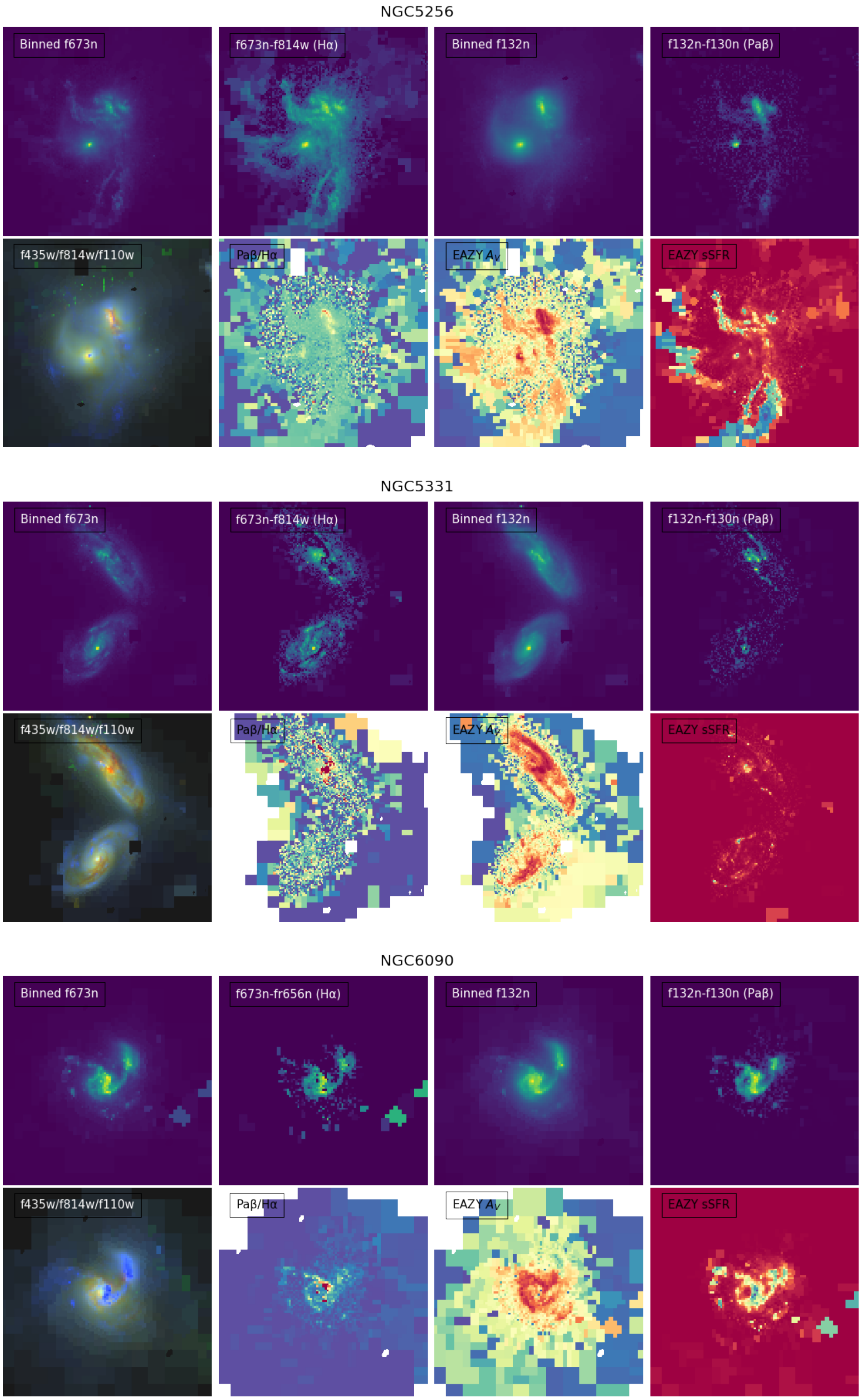
NGC5256
Binned f673n
f673n-f814w (Hα)
Binned f132n
f132n-f130n (Paβ)
f435w/f814w/f110w
Paβ/Hα
EAZY A_V
EAZY sSFR
NGC5331
Binned f673n
f673n-f814w (Hα)
Binned f132n
f132n-f130n (Paβ)
f435w/f814w/f110w
Paβ/Hα
EAZY A_V
EAZY sSFR
NGC6090
Binned f673n
f673n-fr656n (Hα)
Binned f132n
f132n-f130n (Paβ)
f435w/f814w/f110w
Paβ/Hα
EAZY A_V
EAZY sSFR

NGC6217

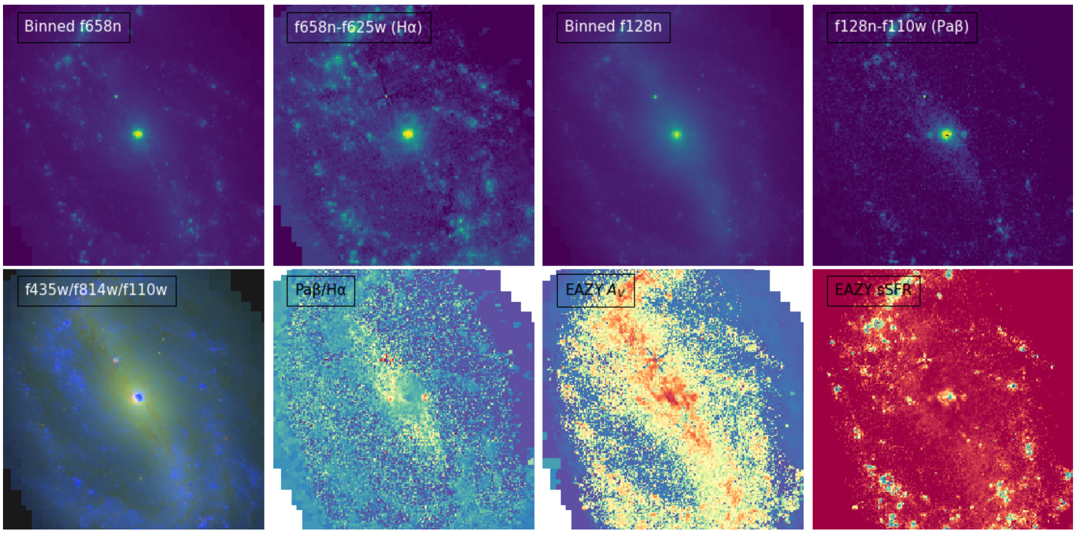

NGC6240

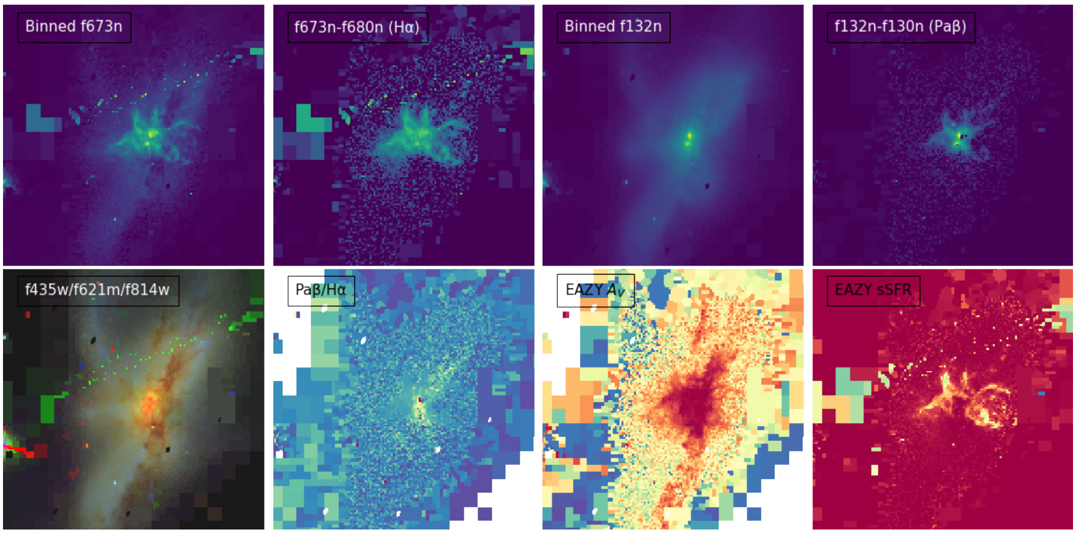

NGC6670

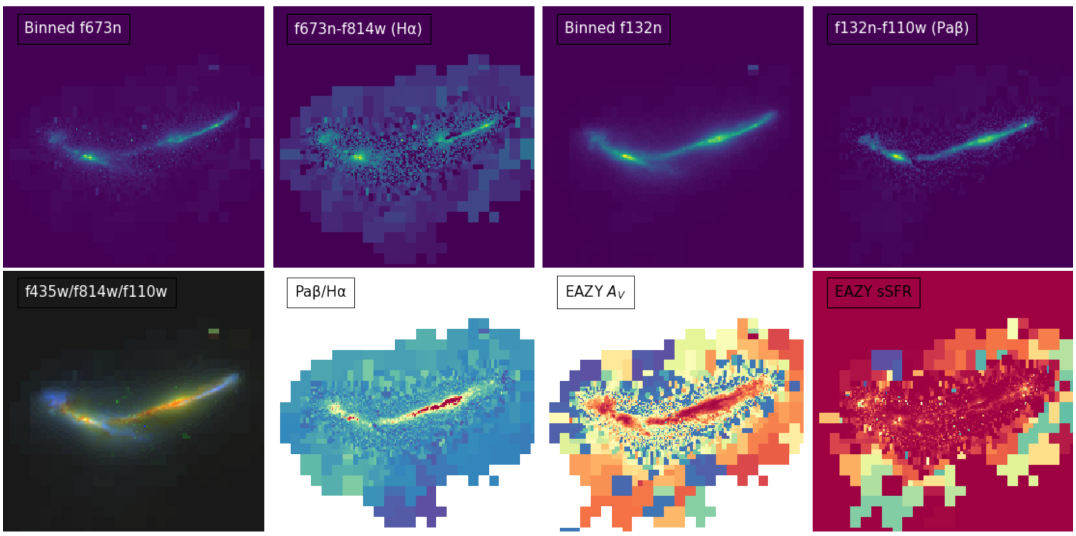

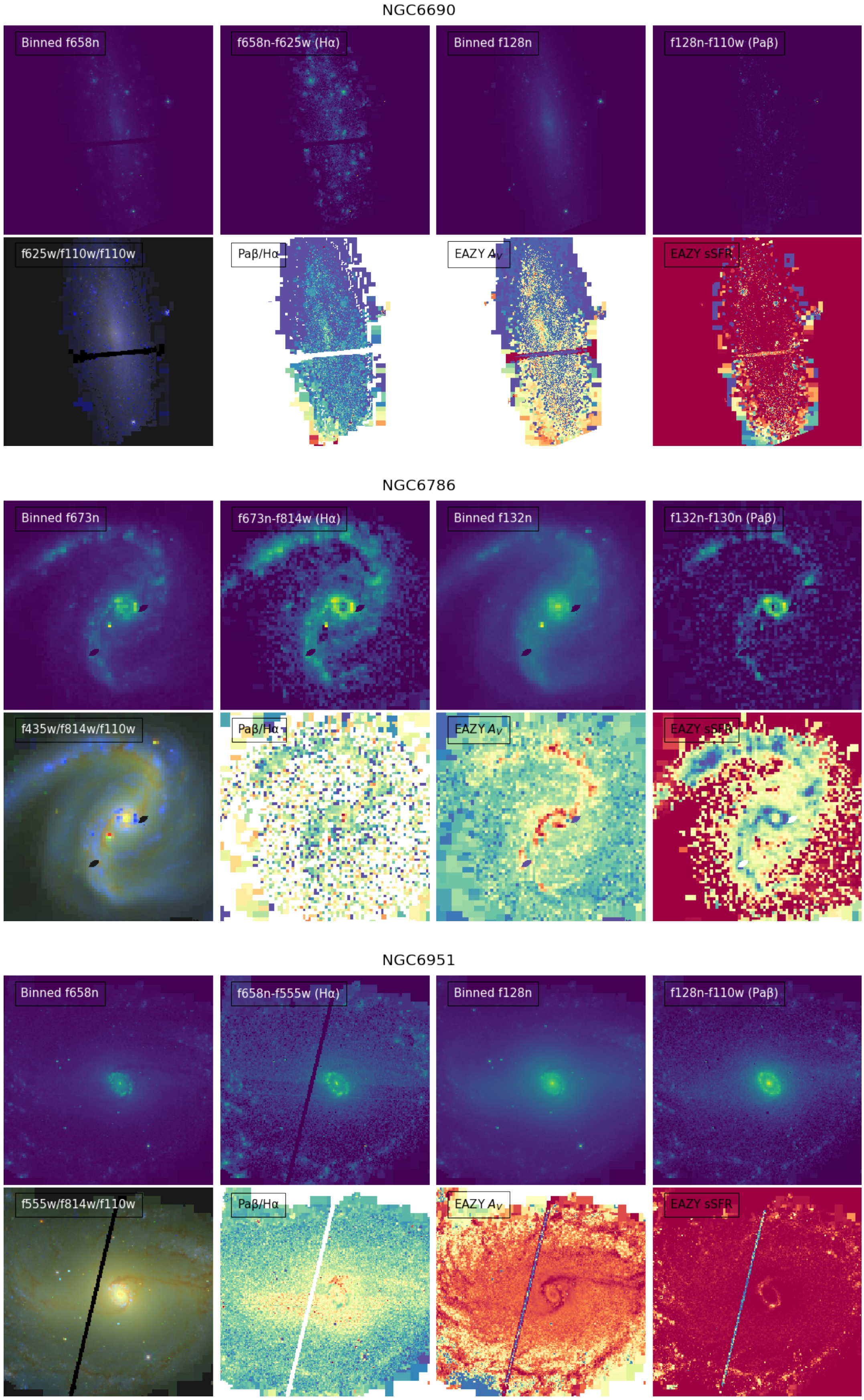
NGC6690
Binned f658n
f658n-f625w (Hα)
Binned f128n
f128n-f110w (Paβ)
f625w/f110w/f110w
Paβ/Hα
EAZY A_V
EAZY sSFR
NGC6786
Binned f673n
f673n-f814w (Hα)
Binned f132n
f132n-f130n (Paβ)
f435w/f814w/f110w
Paβ/Hα
EAZY A_V
EAZY sSFR
NGC6951
Binned f658n
f658n-f555w (Hα)
Binned f128n
f128n-f110w (Paβ)
f555w/f814w/f110w
Paβ/Hα
EAZY A_V
EAZY sSFR

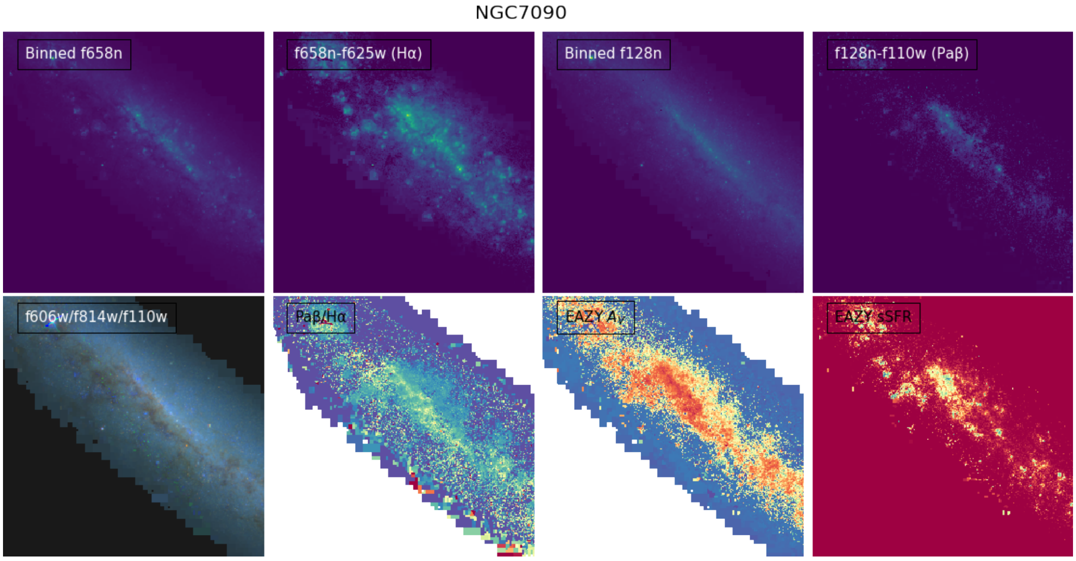
NGC7090
Binned f658n
f658n-f625w (Hα)
Binned f128n
f128n-f110w (Paβ)
f606w/f814w/f110w
Paβ/Hα
EAZY A_V
EAZY sSFR

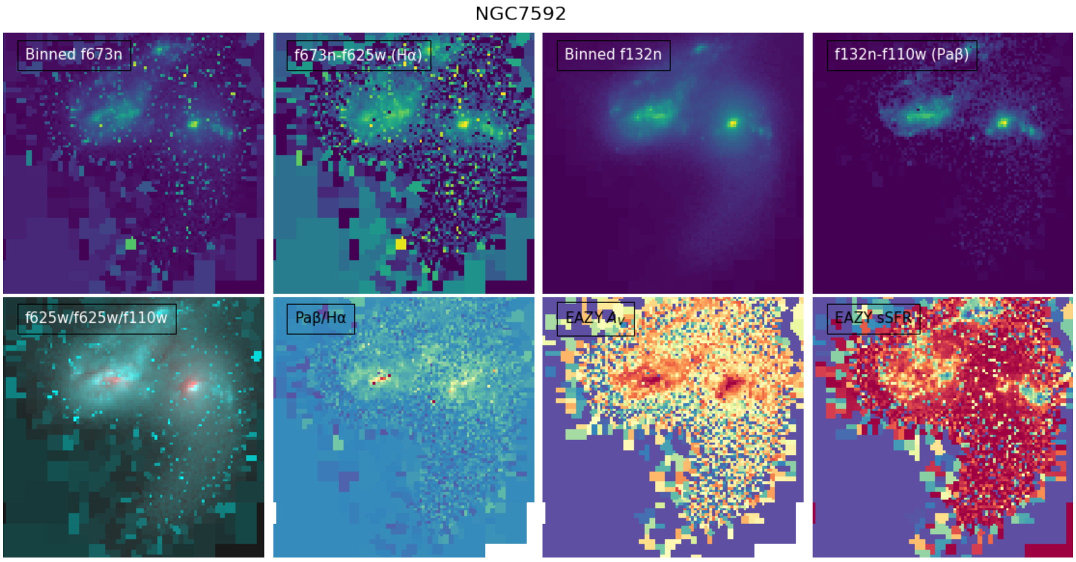
NGC7592
Binned f673n
f673n-f625w (Hα)
Binned f132n
f132n-f110w (Paβ)
f625w/f625w/f110w
Paβ/Hα
EAZY A_V
EAZY sSFR

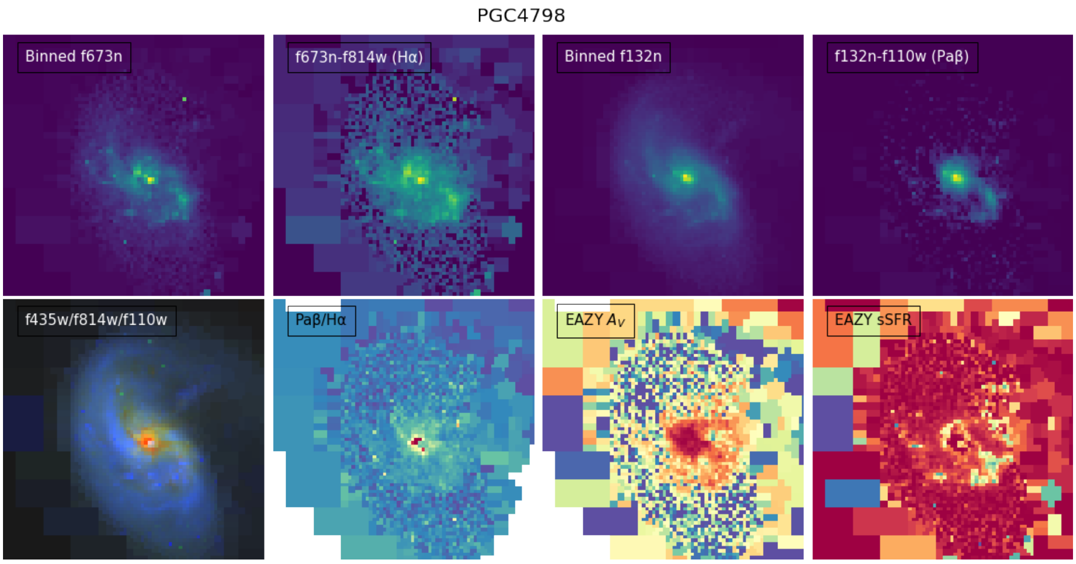
PGC4798
Binned f673n
f673n-f814w (Hα)
Binned f132n
f132n-f110w (Paβ)
f435w/f814w/f110w
Paβ/Hα
EAZY A_V
EAZY sSFR

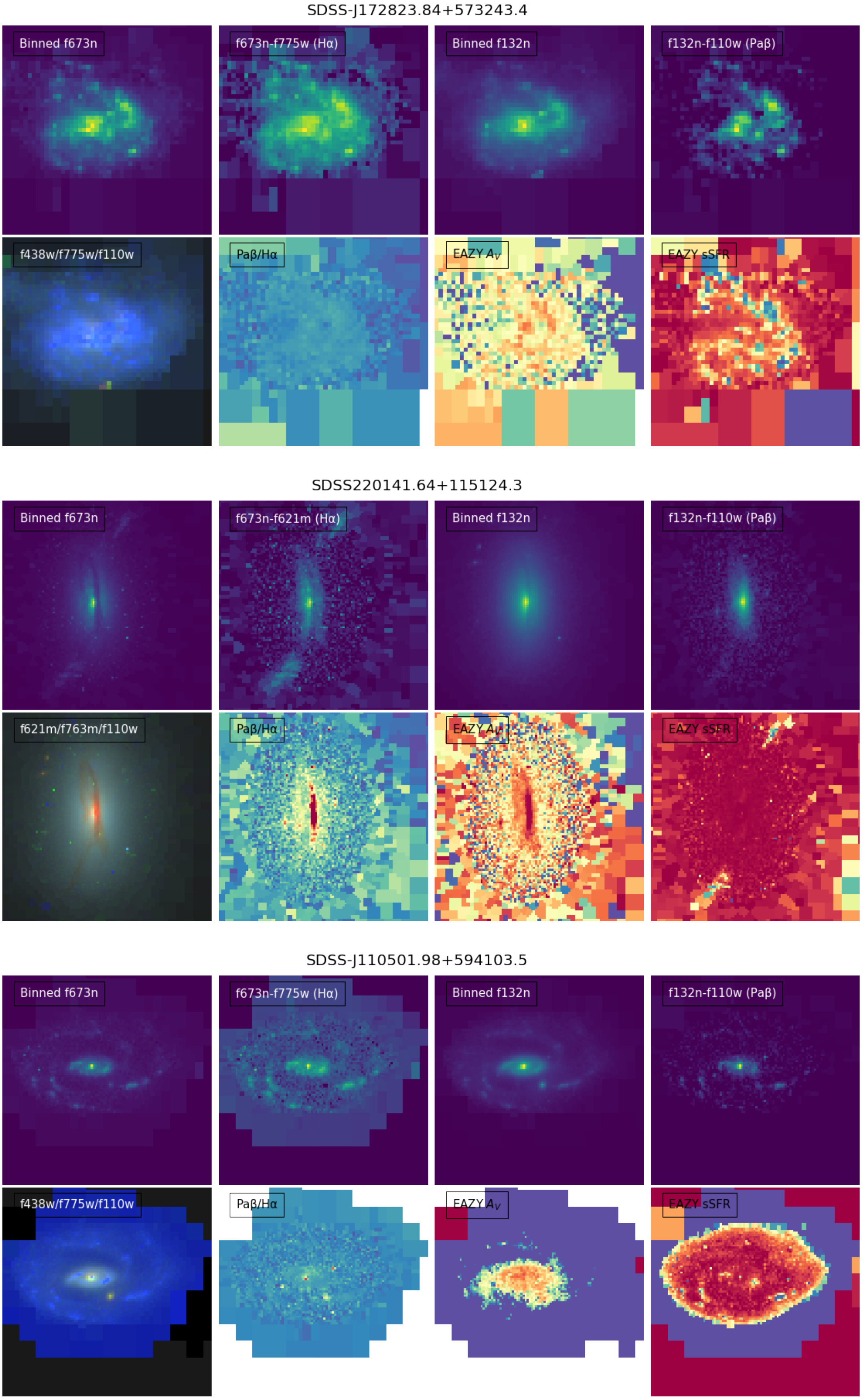
SDSS-J172823.84+573243.4
Binned f673n
f673n-f775w (Hα)
Binned f132n
f132n-f110w (Paβ)
f438w/f775w/f110w
Paβ/Hα
EAZY A_V
EAZY sSFR
SDSS220141.64+115124.3
Binned f673n
f673n-f621m (Hα)
Binned f132n
f132n-f110w (Paβ)
f621m/f763m/f110w
Paβ/Hα
EAZY A_V
EAZY sSFR
SDSS-J110501.98+594103.5
Binned f673n
f673n-f775w (Hα)
Binned f132n
f132n-f110w (Paβ)
f438w/f775w/f110w
Paβ/Hα
EAZY A_V
EAZY sSFR

UGC5626

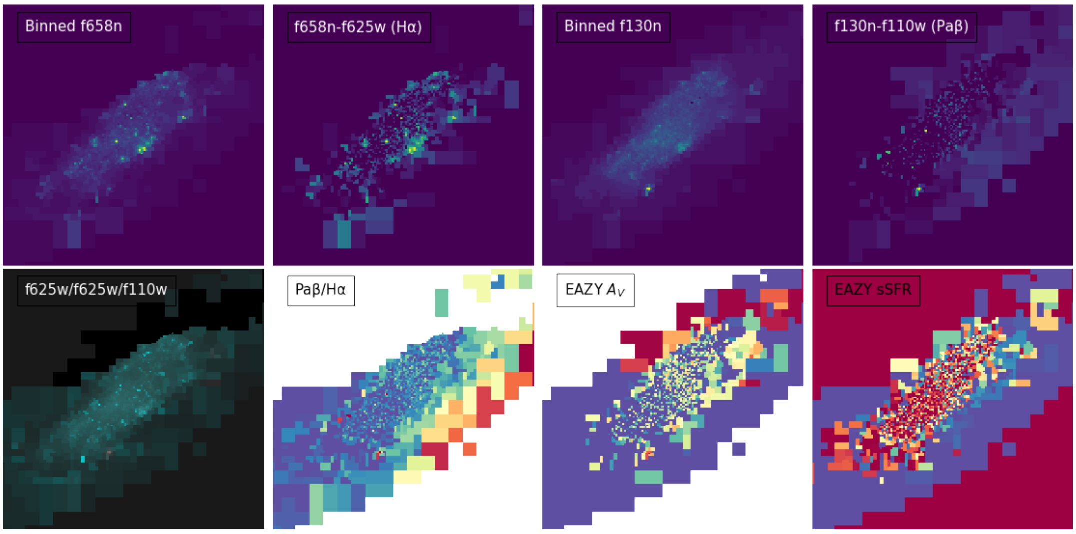

VV340A

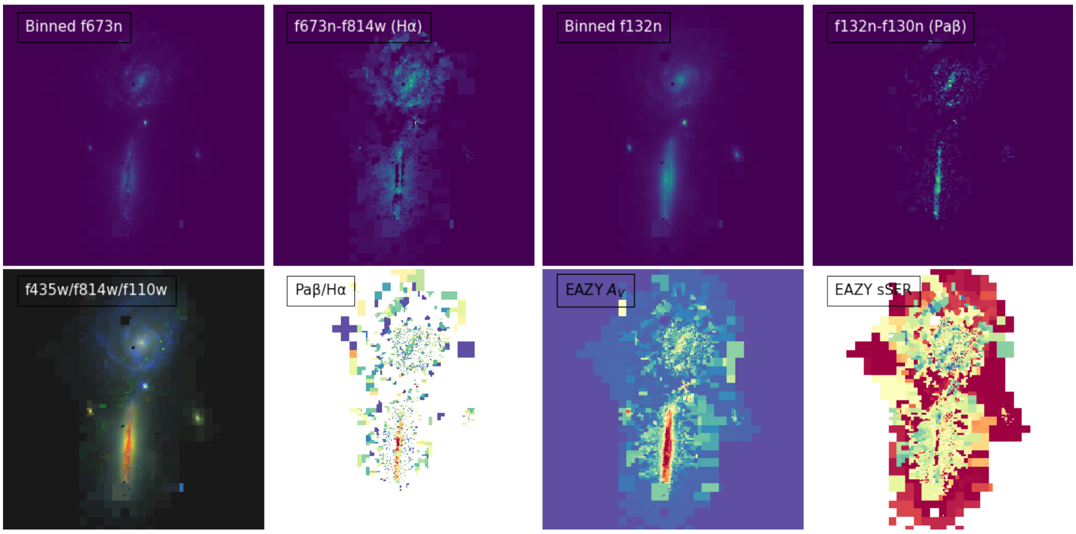

IRAS03582+6012

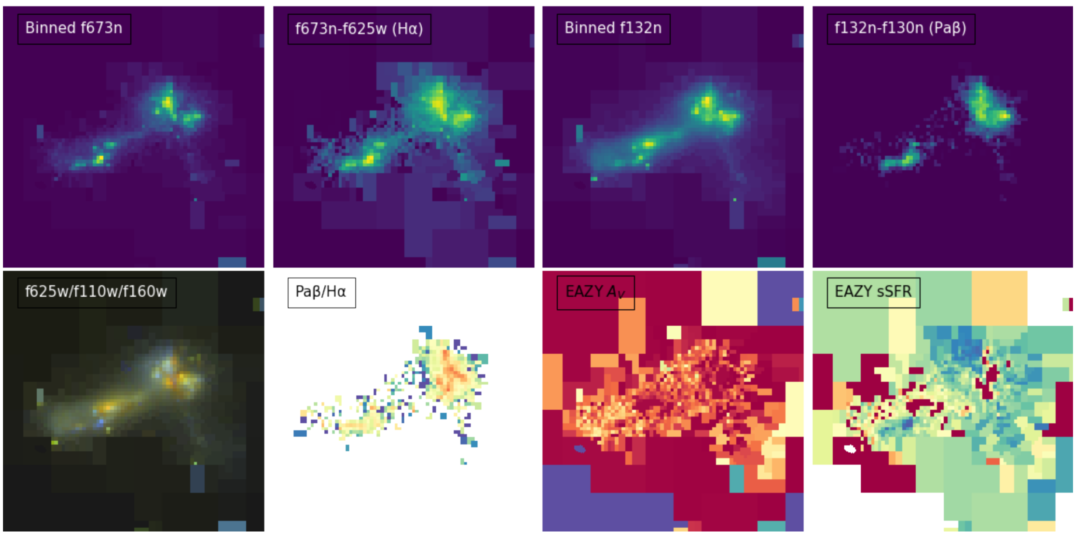

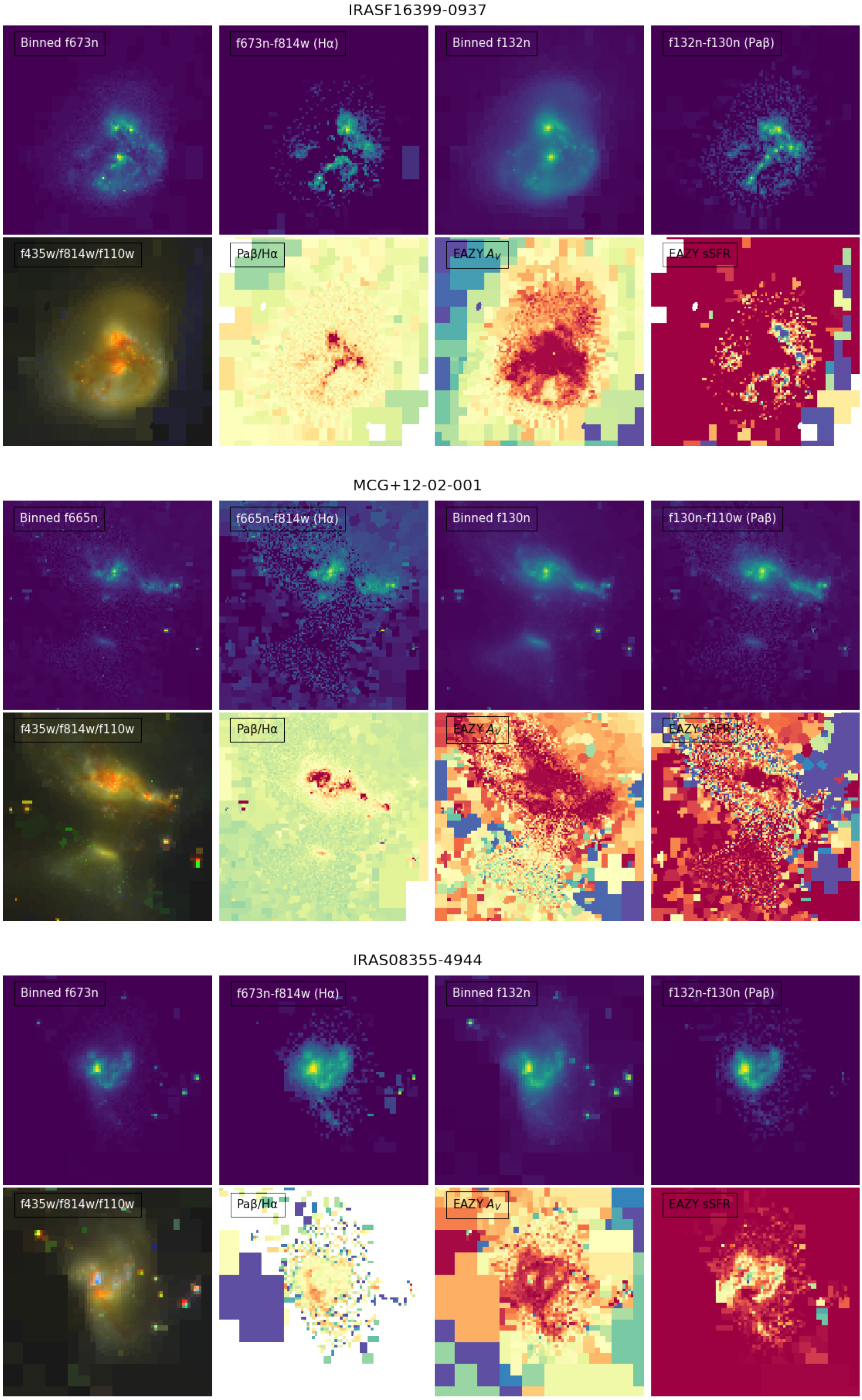

IRASF16399-0937
Binned f673n
f673n-f814w (Hα)
Binned f132n
f132n-f130n (Paβ)
f435w/f814w/f110w
Paβ/Hα
EAZY A_V
EAZY sSFR
MCG+12-02-001
Binned f665n
f665n-f814w (Hα)
Binned f130n
f130n-f110w (Paβ)
f435w/f814w/f110w
Paβ/Hα
EAZY A_V
EAZY sSFR
IRAS08355-4944
Binned f673n
f673n-f814w (Hα)
Binned f132n
f132n-f130n (Paβ)
f435w/f814w/f110w
Paβ/Hα
EAZY A_V
EAZY sSFR

8.2 SEDs from EAZY fitting

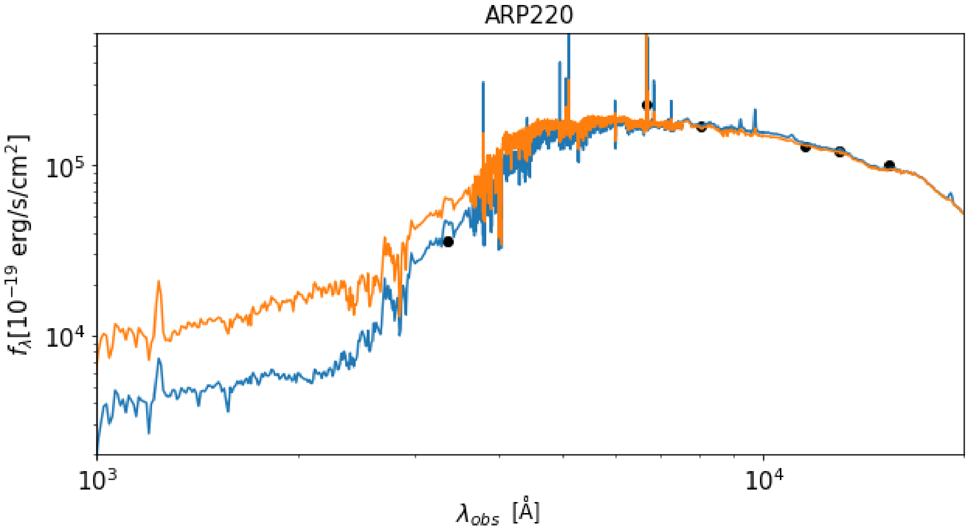

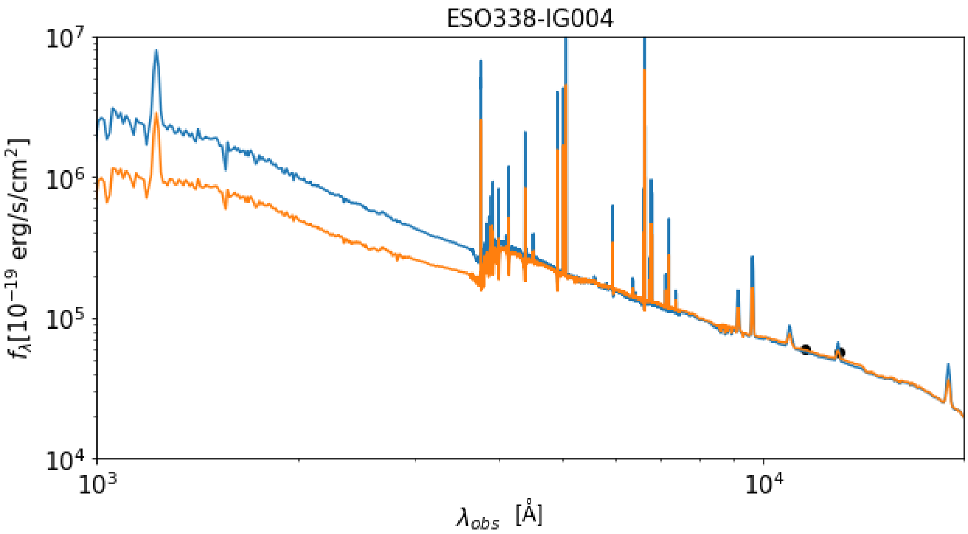

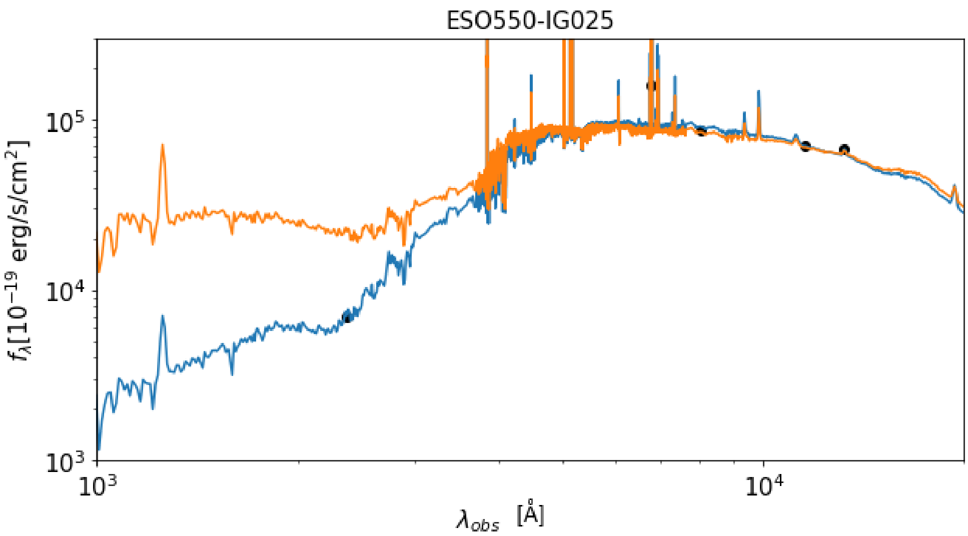

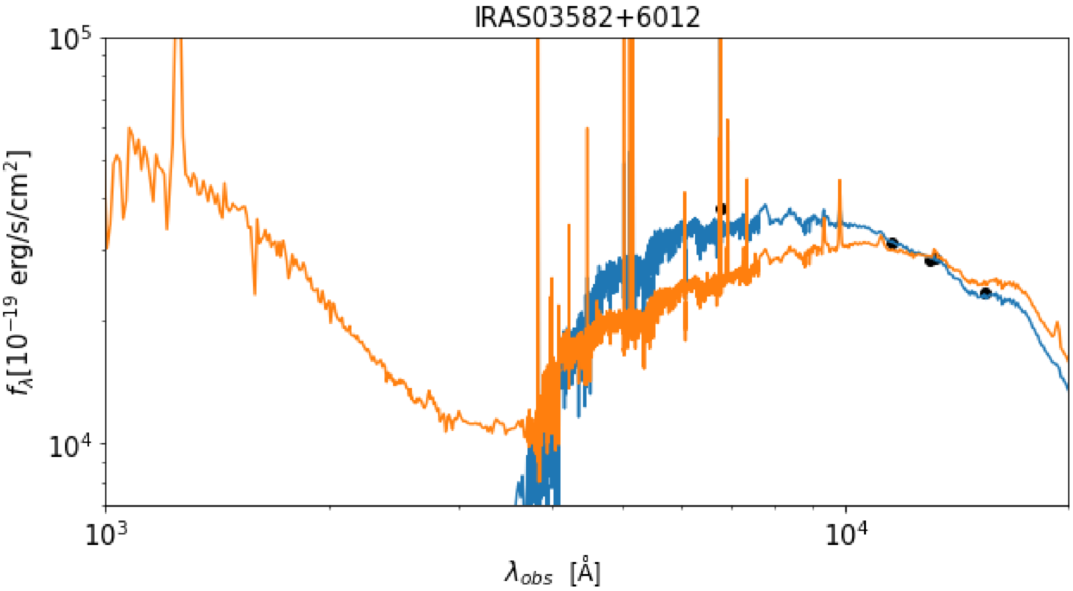
IRAS03582+6012
10^5
10^4
$f_\lambda[10^{-19}$ erg/s/cm$^2]$
10^3
10^4
λ_{obs} [Å]

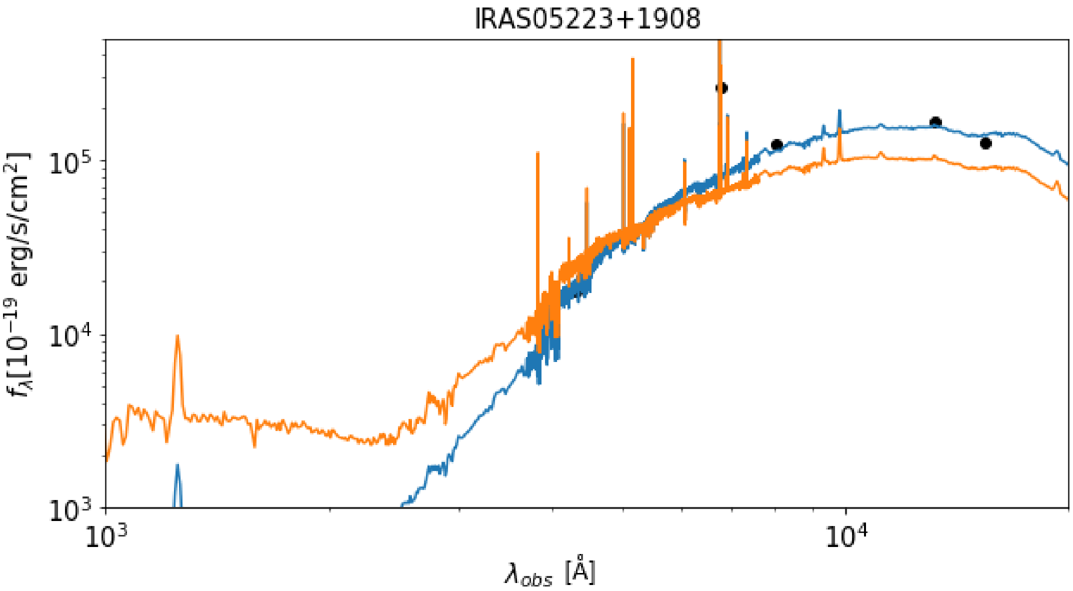
IRAS05223+1908
10^5
10^4
10^3
$f_\lambda[10^{-19}$ erg/s/cm$^2]$
10^3
10^4
λ_{obs} [Å]

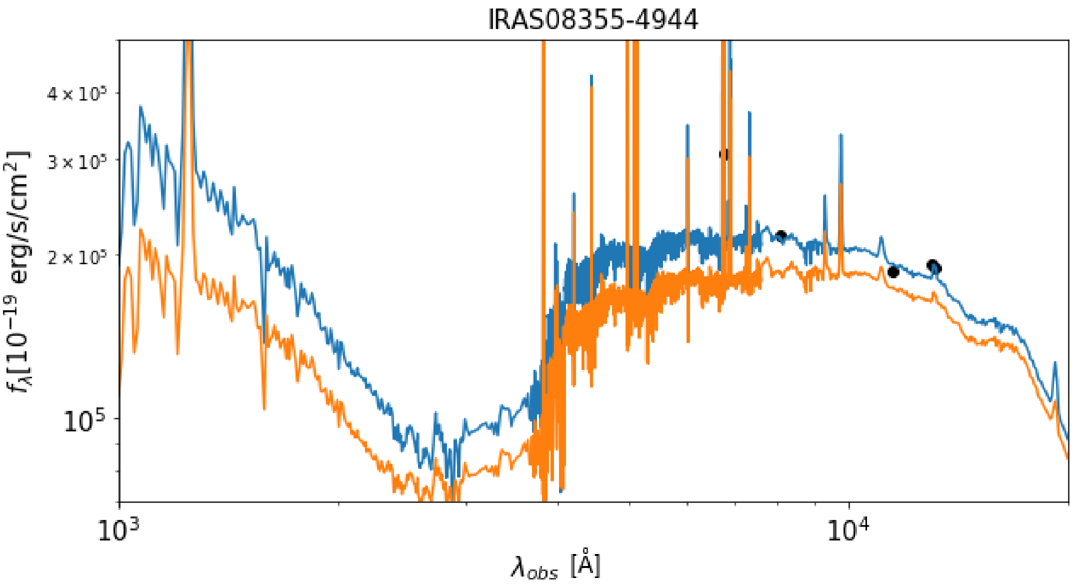
IRAS08355-4944
4×10^5
3×10^5
2×10^5
10^5
$f_\lambda[10^{-19}$ erg/s/cm$^2]$
10^3
10^4
λ_{obs} [Å]

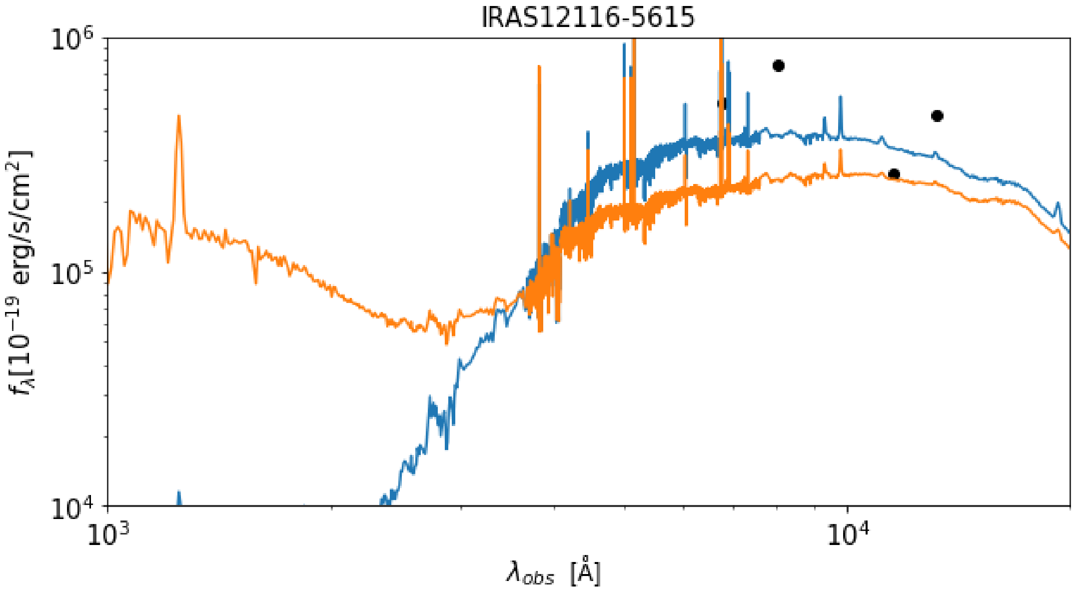
IRAS12116-5615
10^6
10^5
10^4
$f_\lambda [10^{-19}$ erg/s/cm$^2]$
10^3
10^4
λ_{obs} [Å]

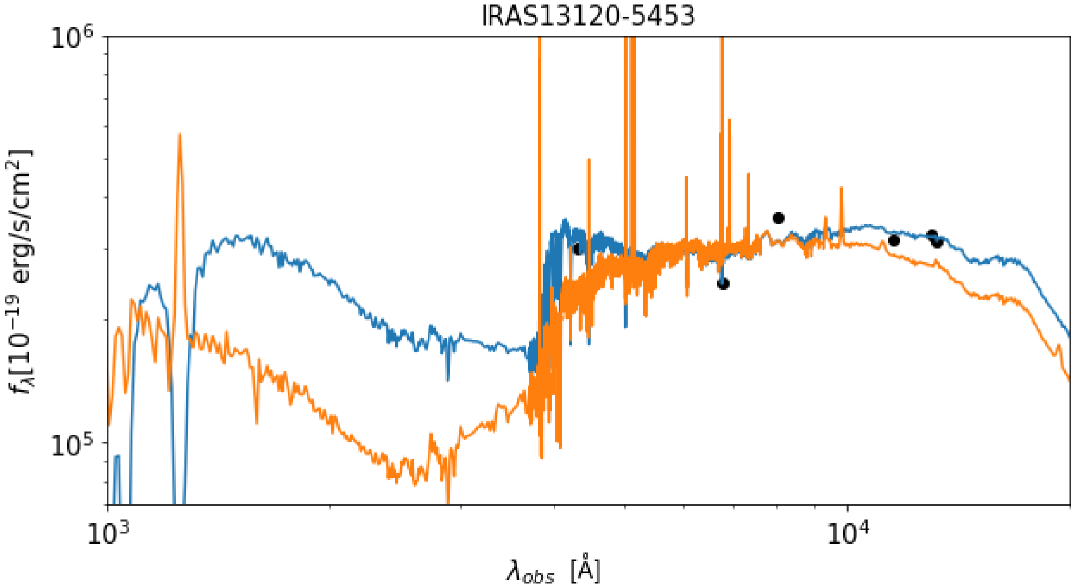
IRAS13120-5453
10^6
10^5
$f_\lambda [10^{-19}$ erg/s/cm$^2]$
10^3
10^4
λ_{obs} [Å]

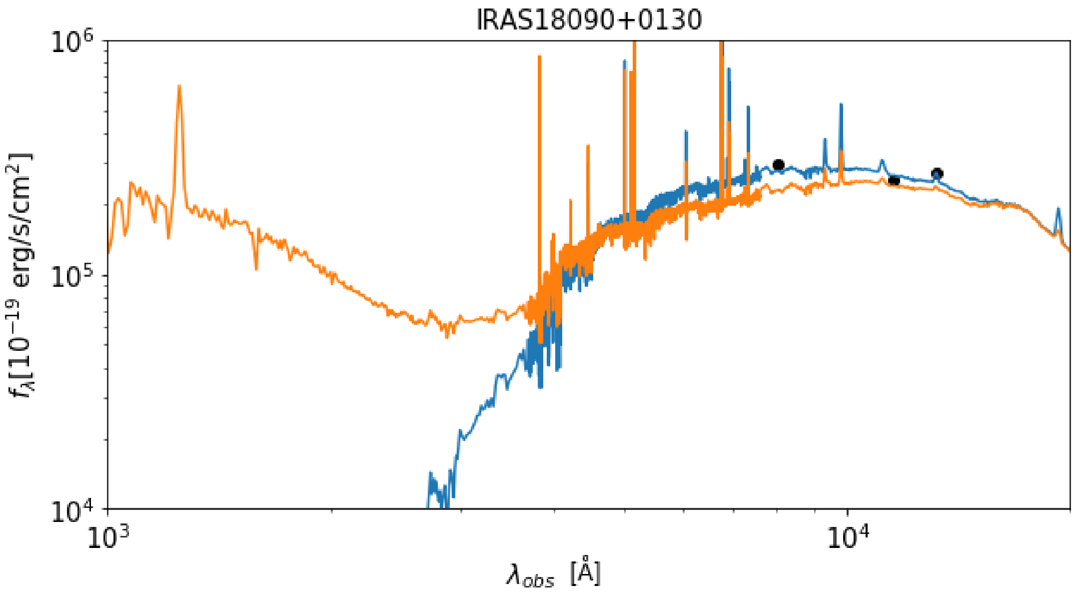
IRAS18090+0130
10^6
10^5
10^4
$f_\lambda [10^{-19}$ erg/s/cm$^2]$
10^3
10^4
λ_{obs} [Å]

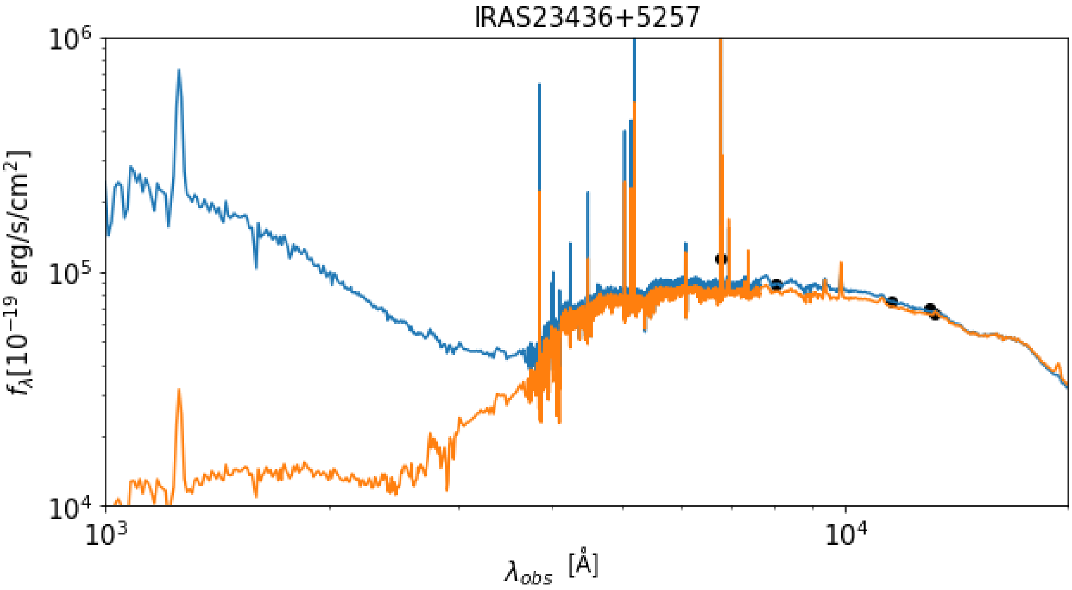
IRAS23436+5257
10^6
10^5
10^4
$f_\lambda[10^{-19}$ erg/s/cm$^2]$
10^3
10^4
λ_{obs} [Å]

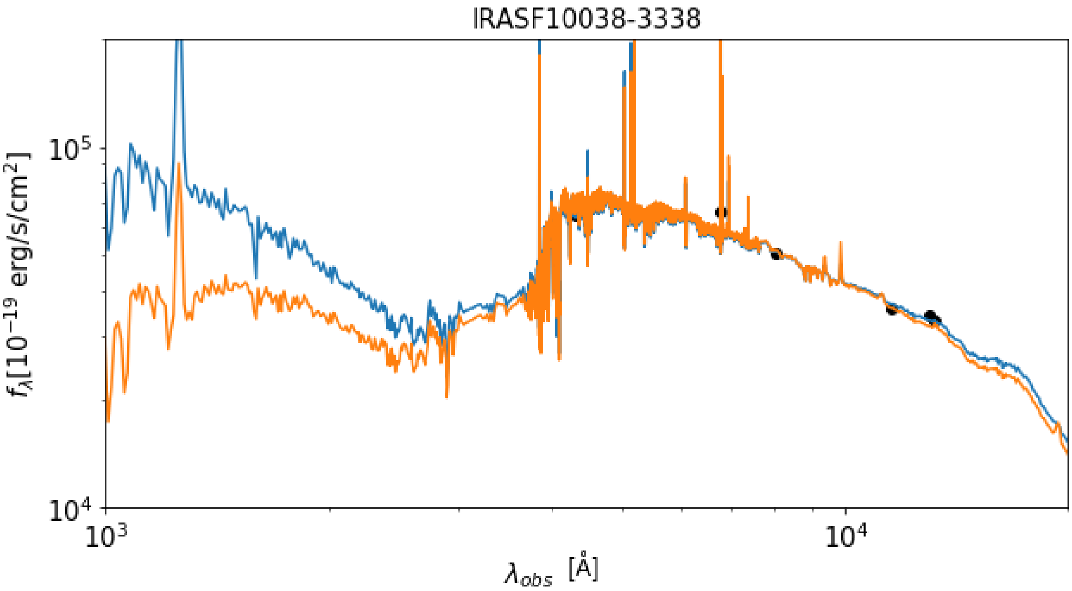
IRASF10038-3338
10^5
10^4
$f_\lambda[10^{-19}$ erg/s/cm$^2]$
10^3
10^4
λ_{obs} [Å]

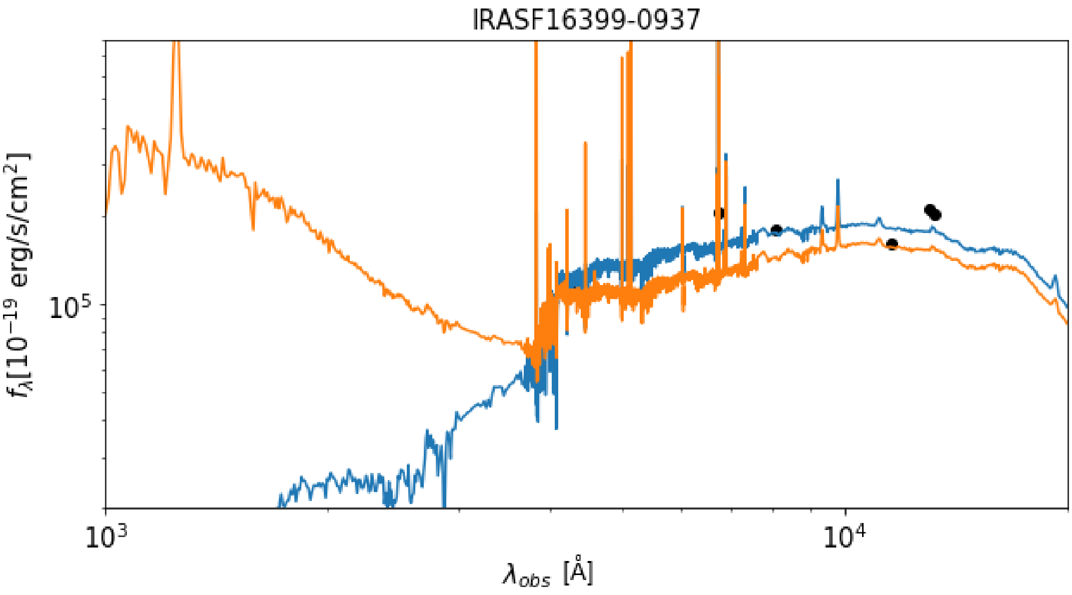
IRASF16399-0937
10^5
$f_\lambda[10^{-19}$ erg/s/cm$^2]$
10^3
10^4
λ_{obs} [Å]

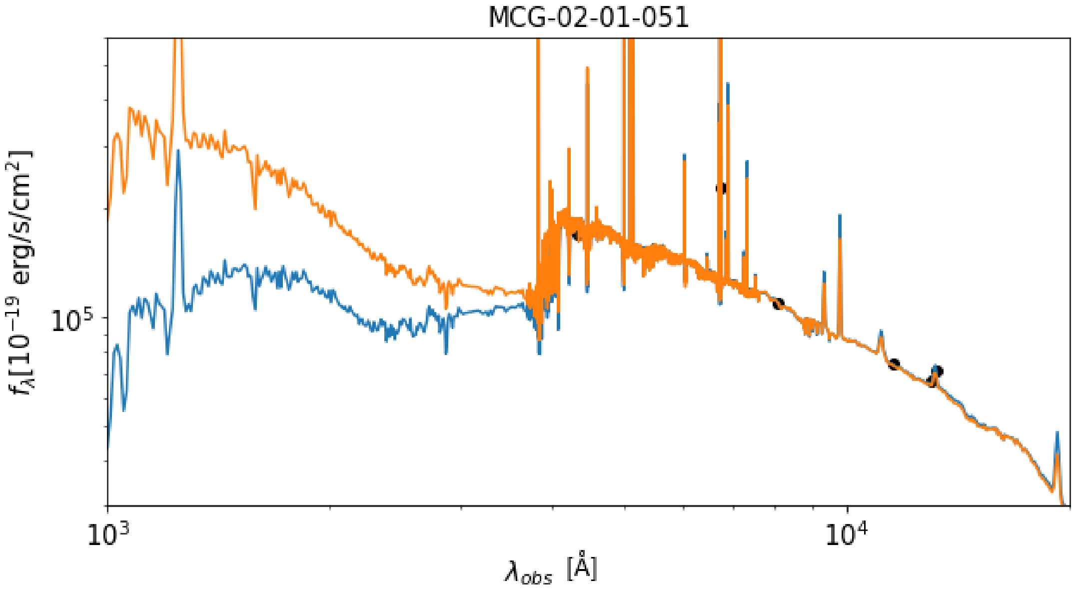
MCG-02-01-051
$f_\lambda[10^{-19}$ erg/s/cm$^2]$
10^5
10^3
10^4
λ_{obs} [Å]

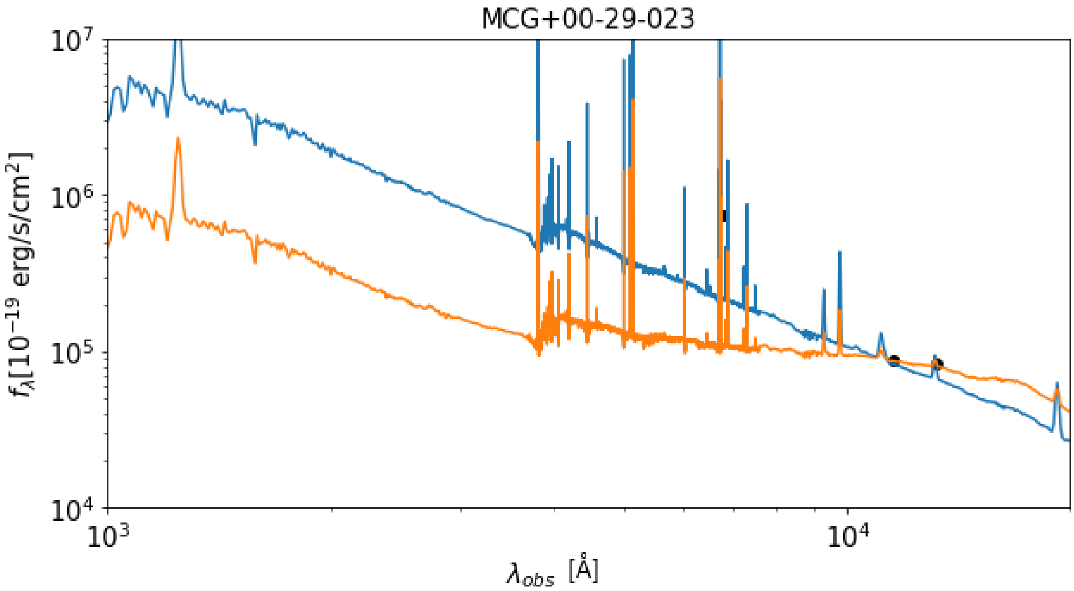
MCG+00-29-023
$f_\lambda[10^{-19}$ erg/s/cm$^2]$
10^7
10^6
10^5
10^4
10^3
10^4
λ_{obs} [Å]

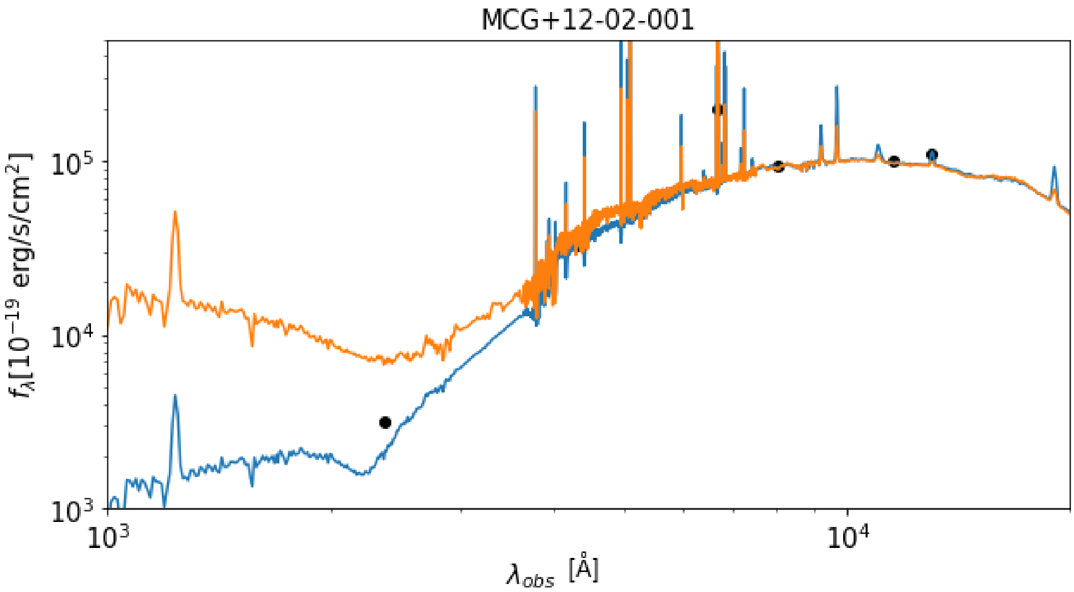
MCG+12-02-001
$f_\lambda[10^{-19}$ erg/s/cm$^2]$
10^5
10^4
10^3
10^3
10^4
λ_{obs} [Å]

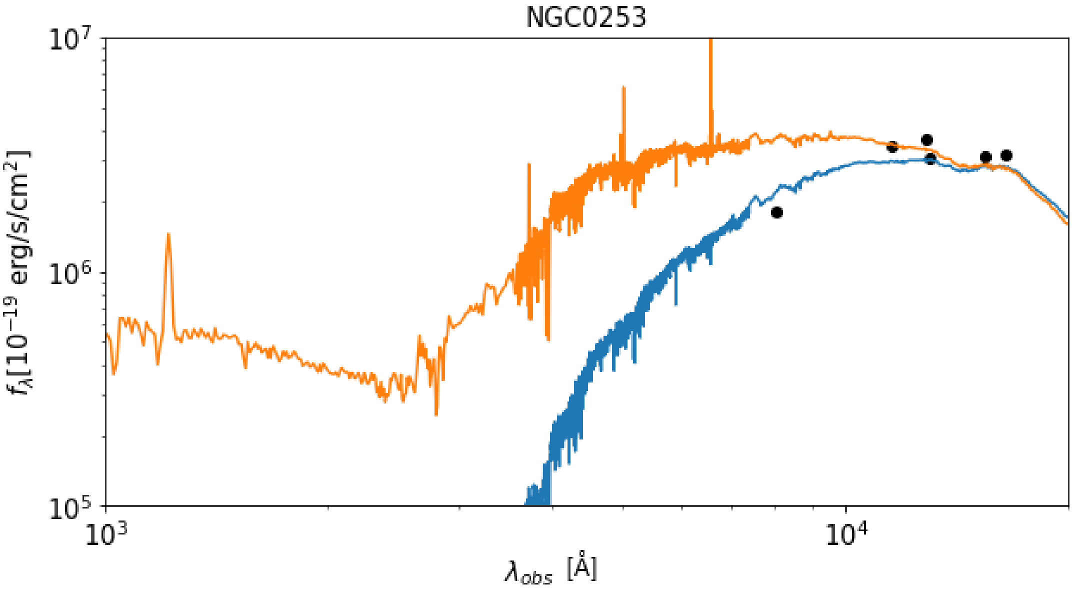

NGC0253
10^7
10^6
10^5
$f_\lambda[10^{-19}$ erg/s/cm$^2]$
10^3
10^4
λ_{obs} [Å]

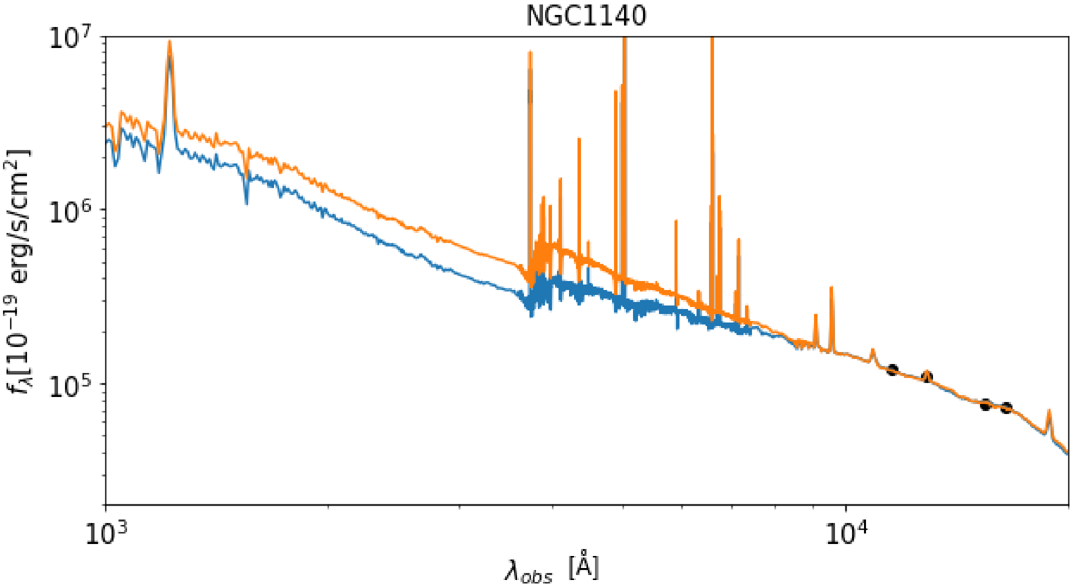

NGC1140
10^7
10^6
10^5
$f_\lambda[10^{-19}$ erg/s/cm$^2]$
10^3
10^4
λ_{obs} [Å]

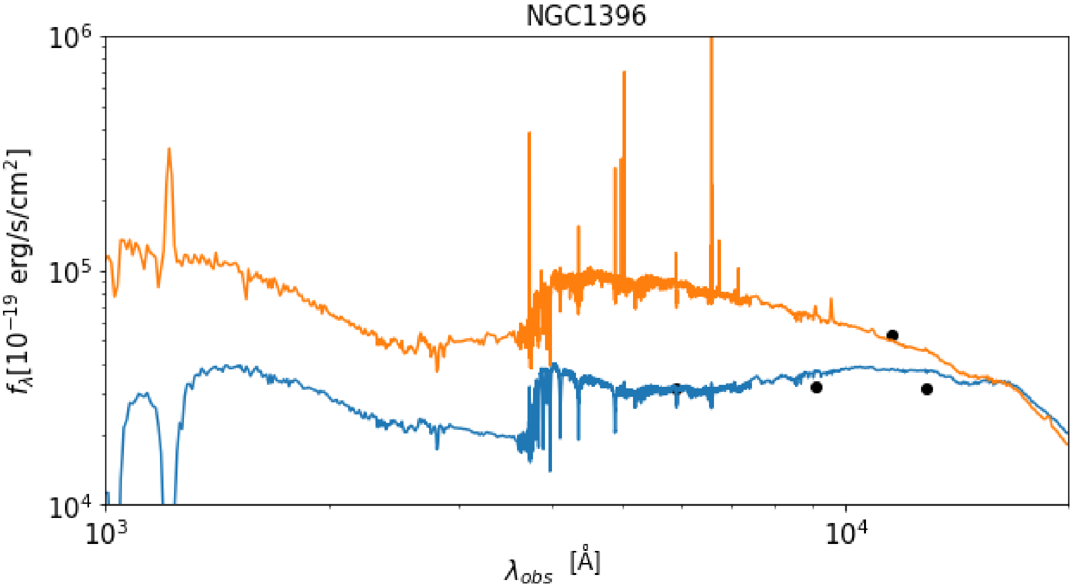

NGC1396
10^6
10^5
10^4
$f_\lambda[10^{-19}$ erg/s/cm$^2]$
10^3
10^4
λ_{obs} [Å]

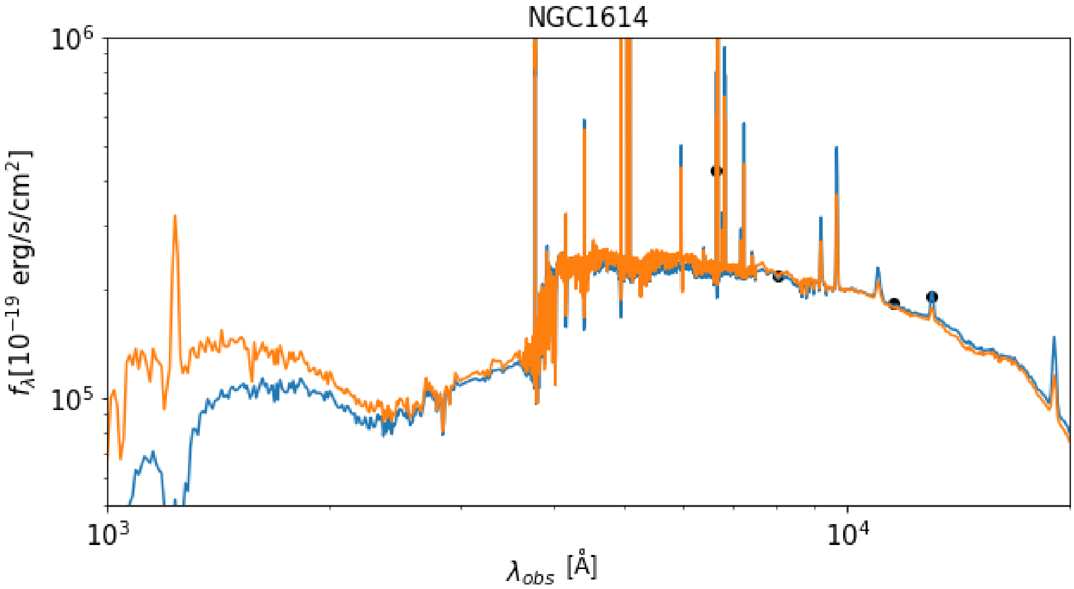
NGC1614
10^6
10^5
$f_\lambda[10^{-19}$ erg/s/cm$^2]$
10^3
10^4
λ_{obs} [Å]

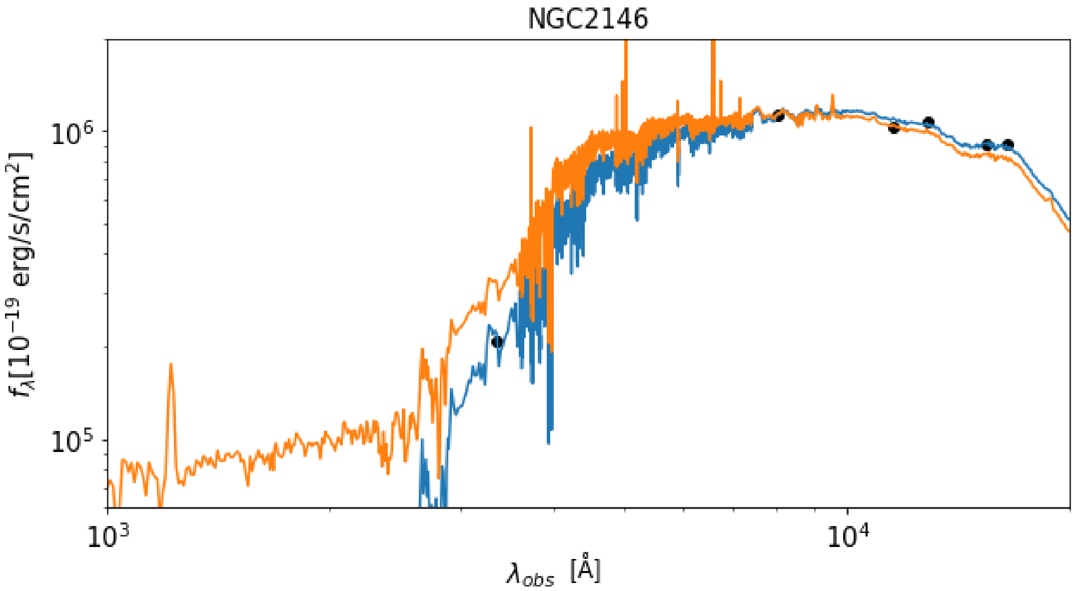
NGC2146
10^6
10^5
$f_\lambda[10^{-19}$ erg/s/cm$^2]$
10^3
10^4
λ_{obs} [Å]

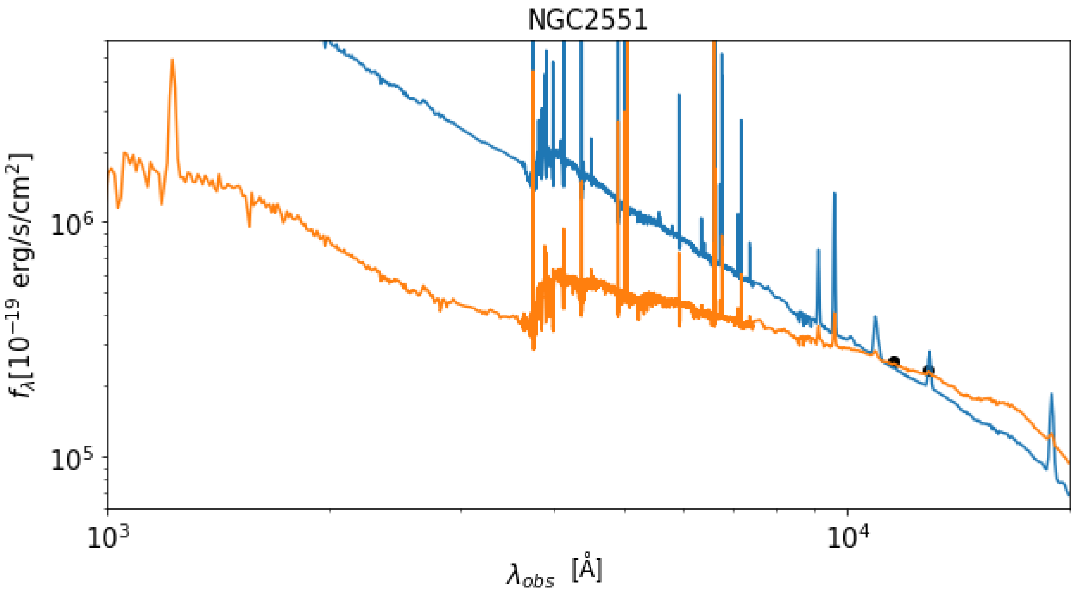
NGC2551
10^6
10^5
$f_\lambda[10^{-19}$ erg/s/cm$^2]$
10^3
10^4
λ_{obs} [Å]

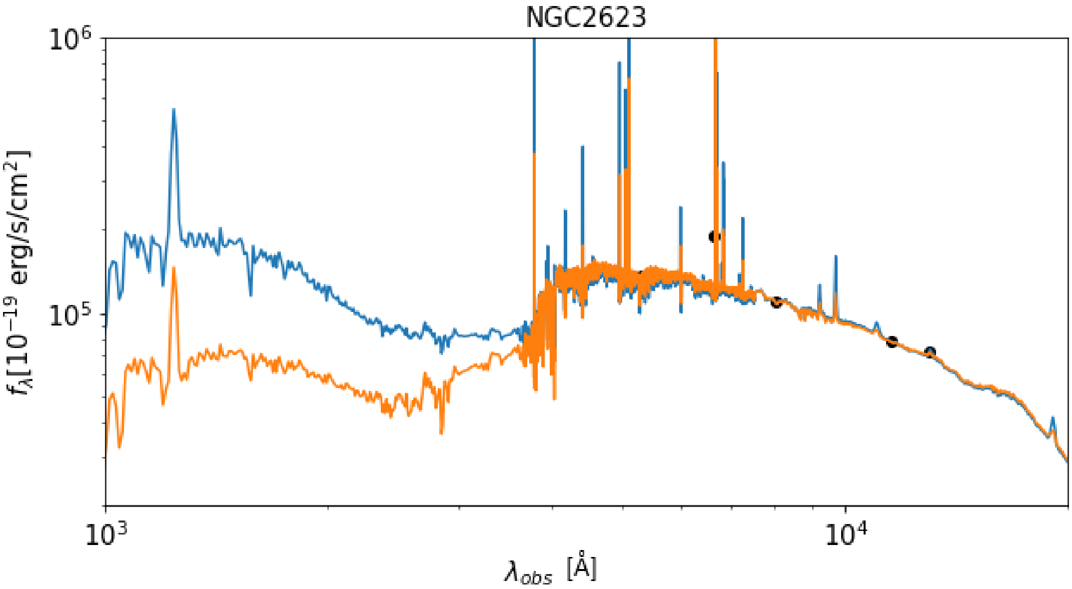
NGC2623
10^6
10^5
$f_\lambda[10^{-19}$ erg/s/cm$^2]$
10^3
10^4
λ_{obs} [Å]

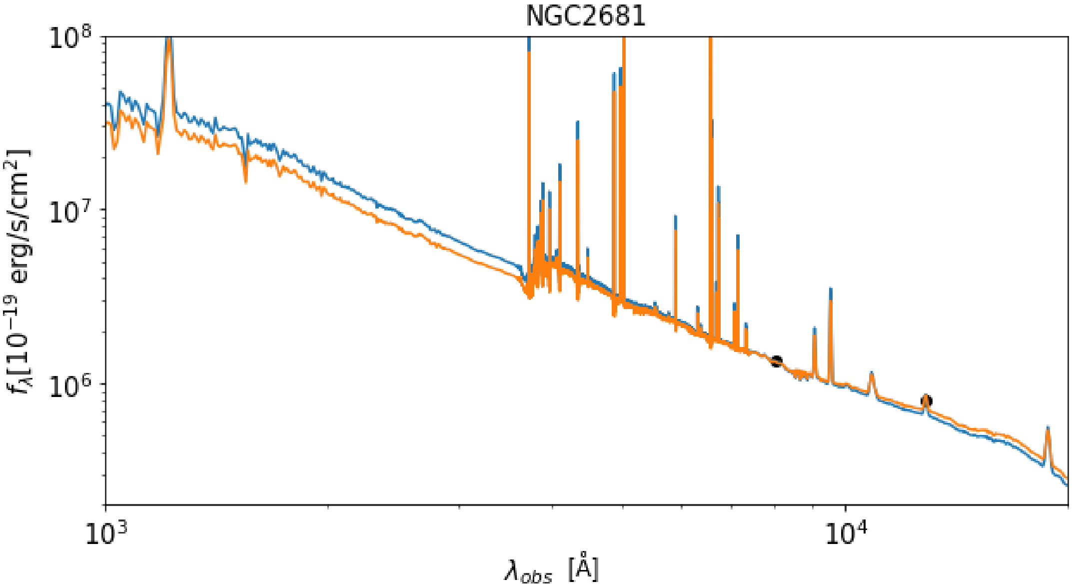
NGC2681
10^8
10^7
10^6
$f_\lambda[10^{-19}$ erg/s/cm$^2]$
10^3
10^4
λ_{obs} [Å]

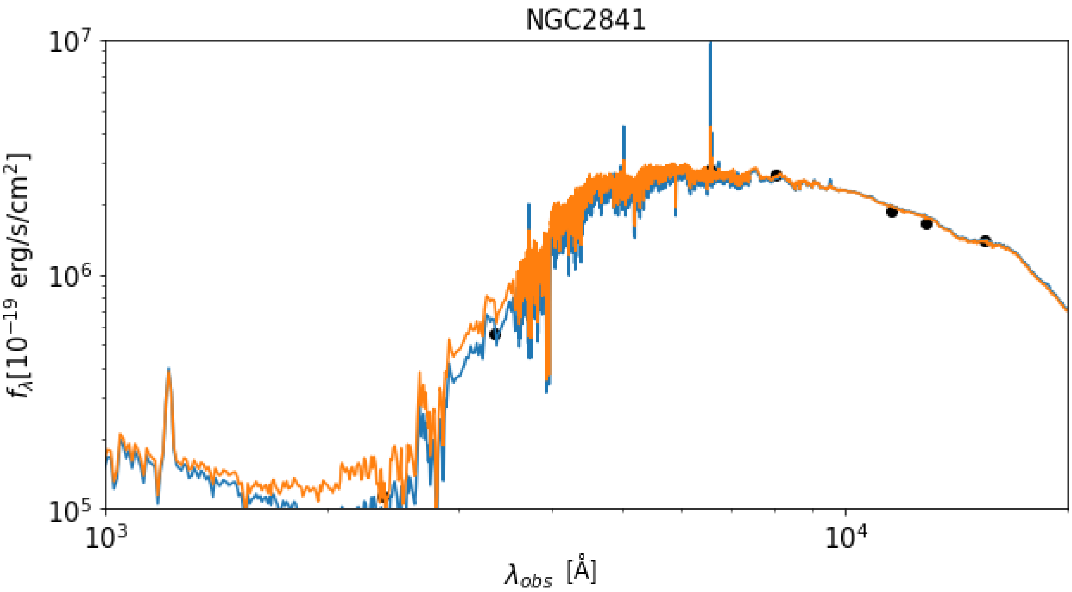
NGC2841
10^7
10^6
10^5
$f_\lambda[10^{-19}$ erg/s/cm$^2]$
10^3
10^4
λ_{obs} [Å]

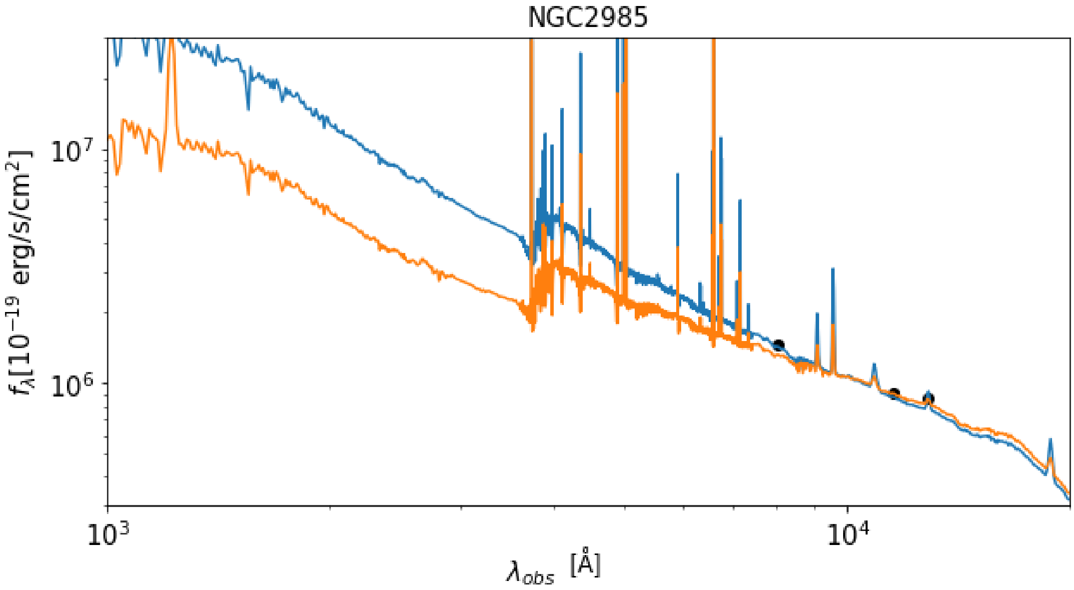
NGC2985
10^7
10^6
$f_\lambda[10^{-19}$ erg/s/cm$^2]$
10^3
10^4
λ_{obs} [Å]

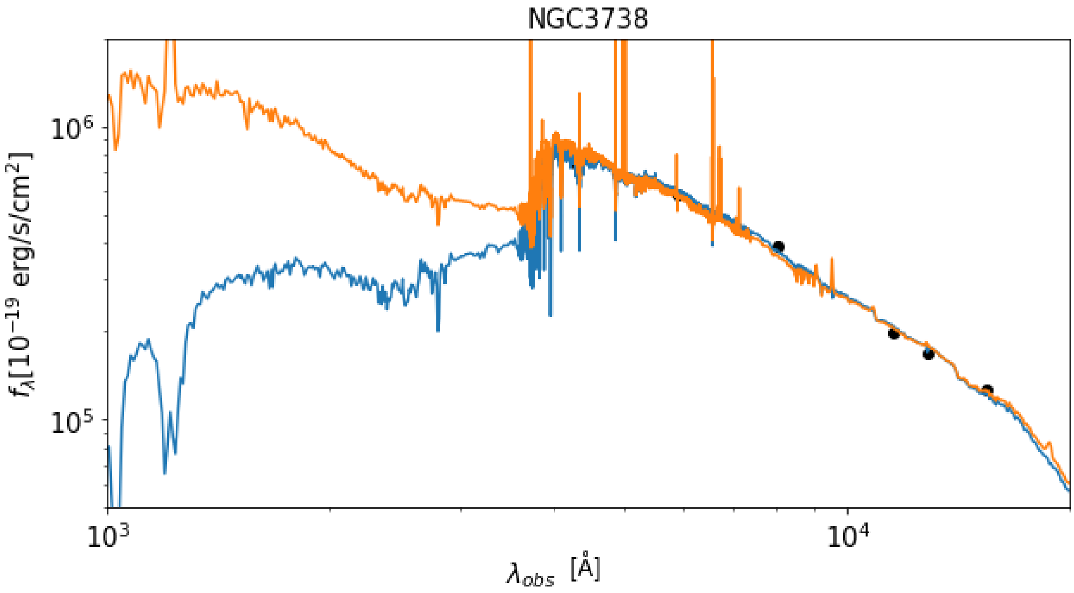
NGC3738
10^6
10^5
$f_\lambda[10^{-19}$ erg/s/cm$^2]$
10^3
10^4
λ_{obs} [Å]

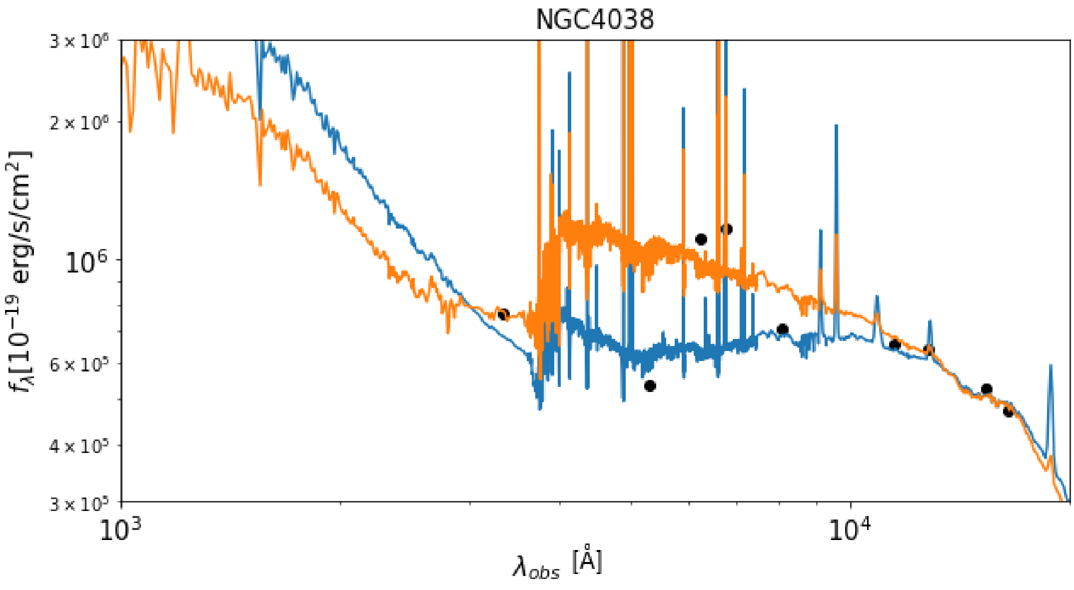
NGC4038
3×10^6
2×10^6
10^6
6×10^5
4×10^5
3×10^5
$f_\lambda[10^{-19}$ erg/s/cm$^2]$
10^3
10^4
λ_{obs} [Å]

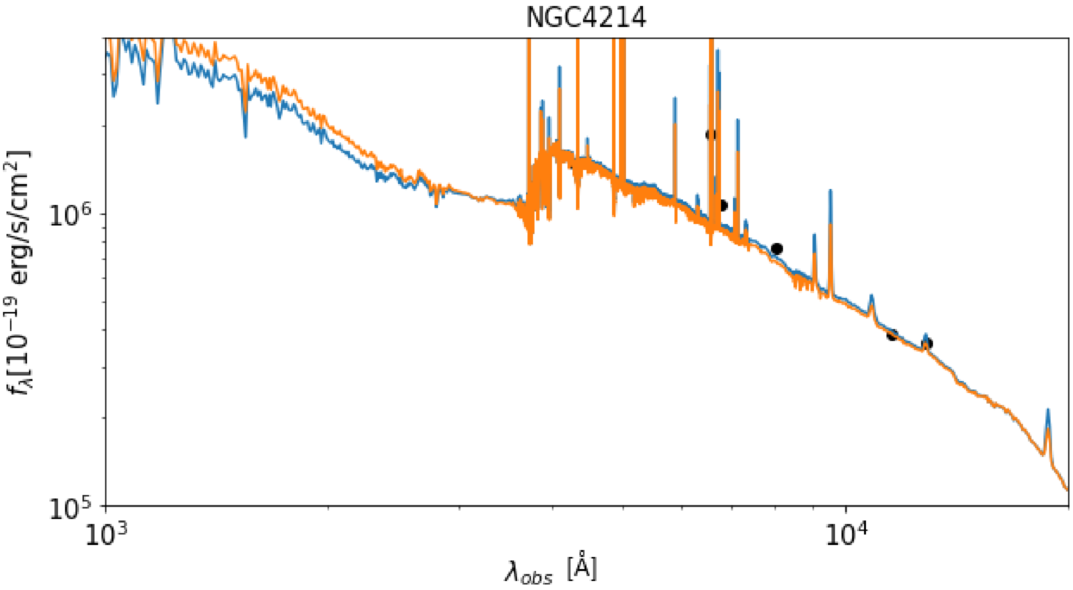
NGC4214
$f_\lambda[10^{-19}$ erg/s/cm$^2]$
10^6
10^5
10^3
10^4
λ_{obs} [Å]

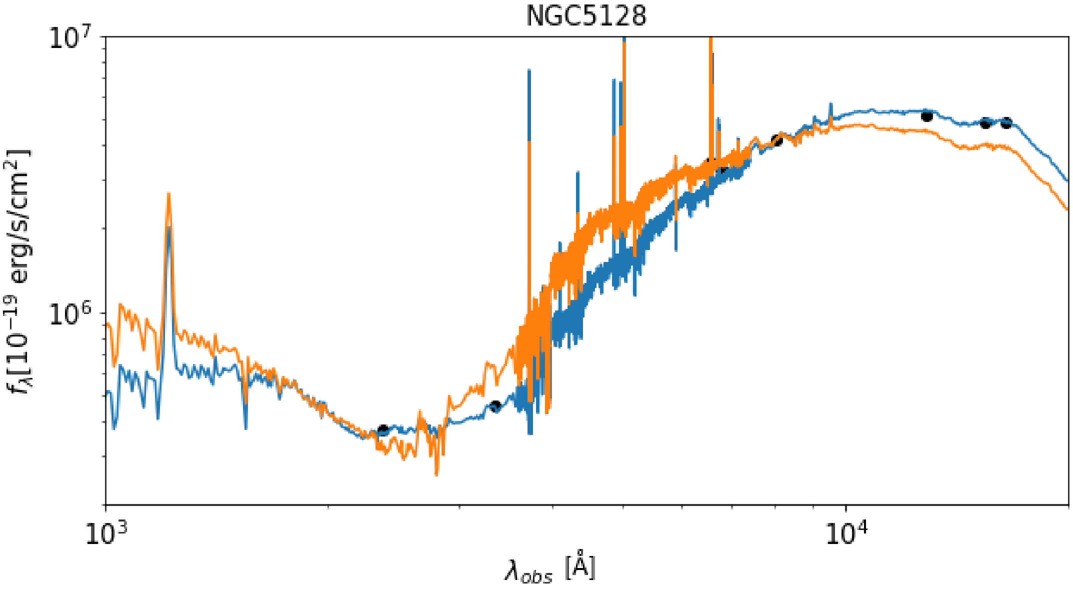
NGC5128
$f_\lambda[10^{-19}$ erg/s/cm$^2]$
10^7
10^6
10^3
10^4
λ_{obs} [Å]

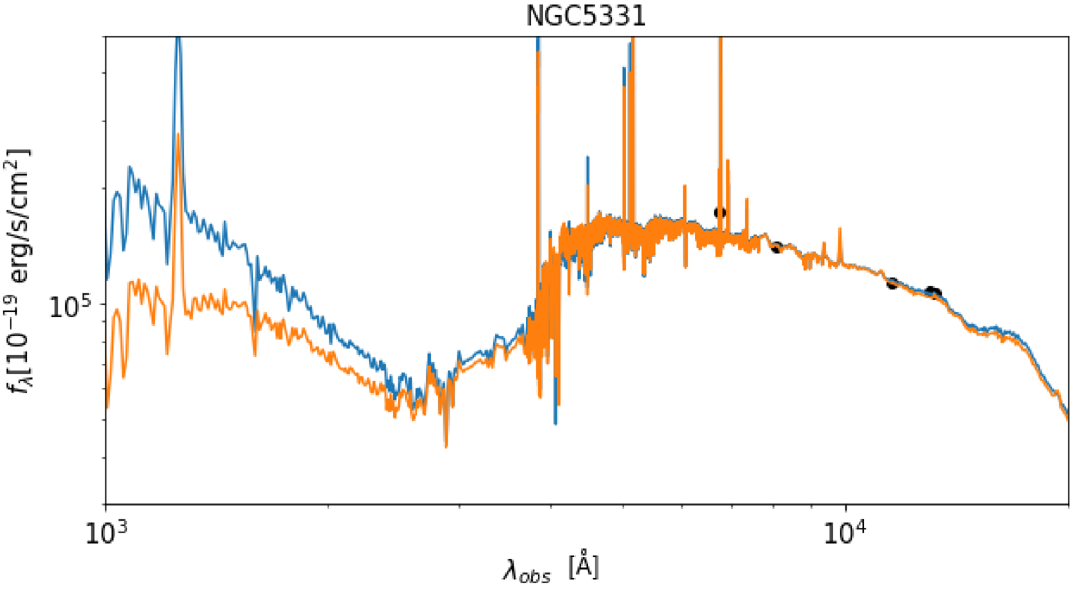
NGC5331
$f_\lambda[10^{-19}$ erg/s/cm$^2]$
10^5
10^3
10^4
λ_{obs} [Å]

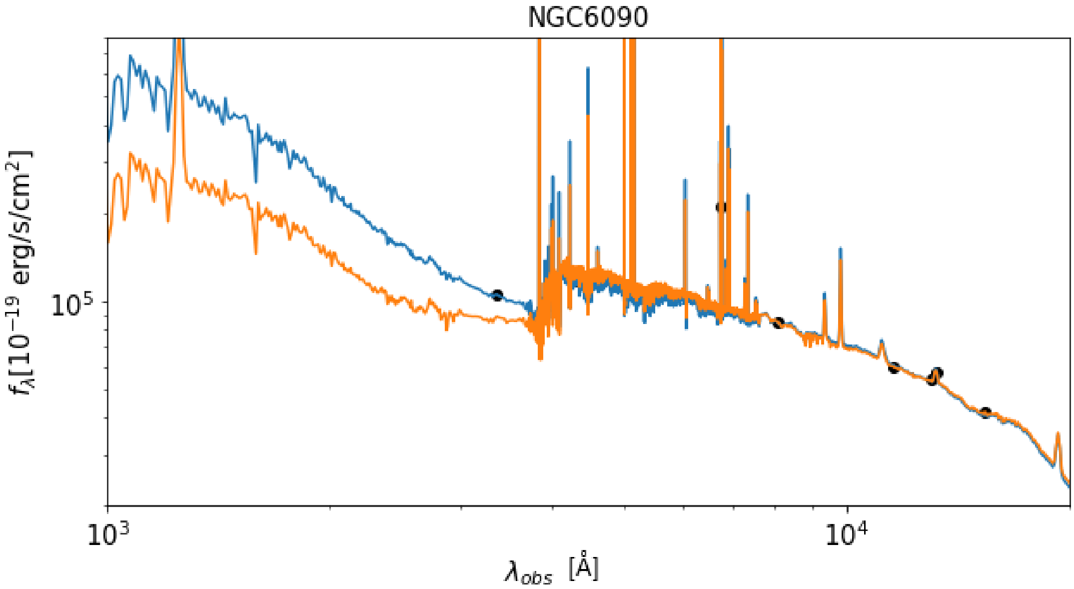
NGC6090
$f_\lambda[10^{-19}$ erg/s/cm$^2]$
10^5
10^3
10^4
λ_{obs} [Å]

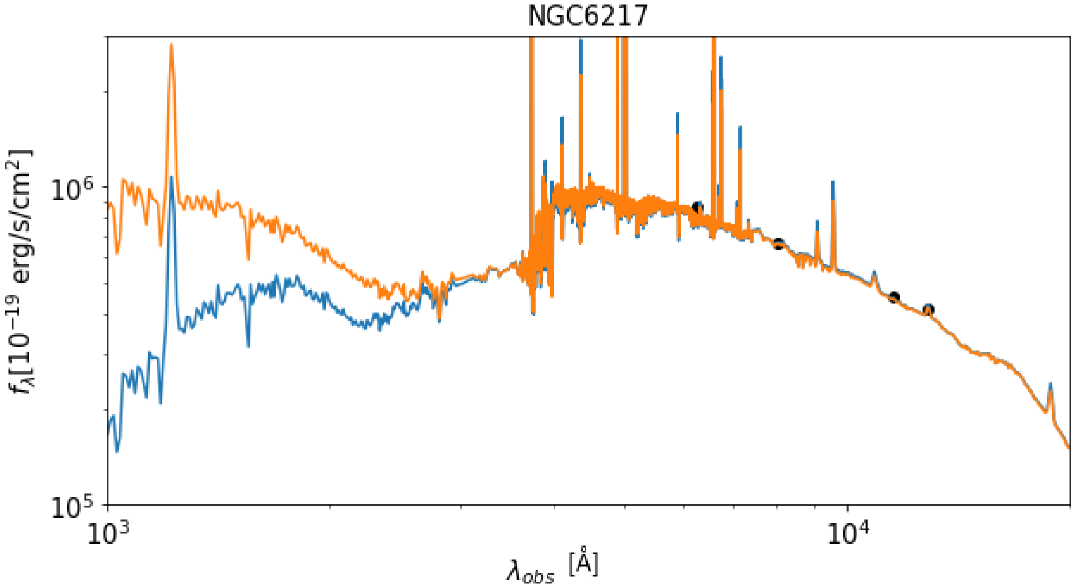
NGC6217
$f_\lambda[10^{-19}$ erg/s/cm$^2]$
10^6
10^5
10^3
10^4
λ_{obs} [Å]

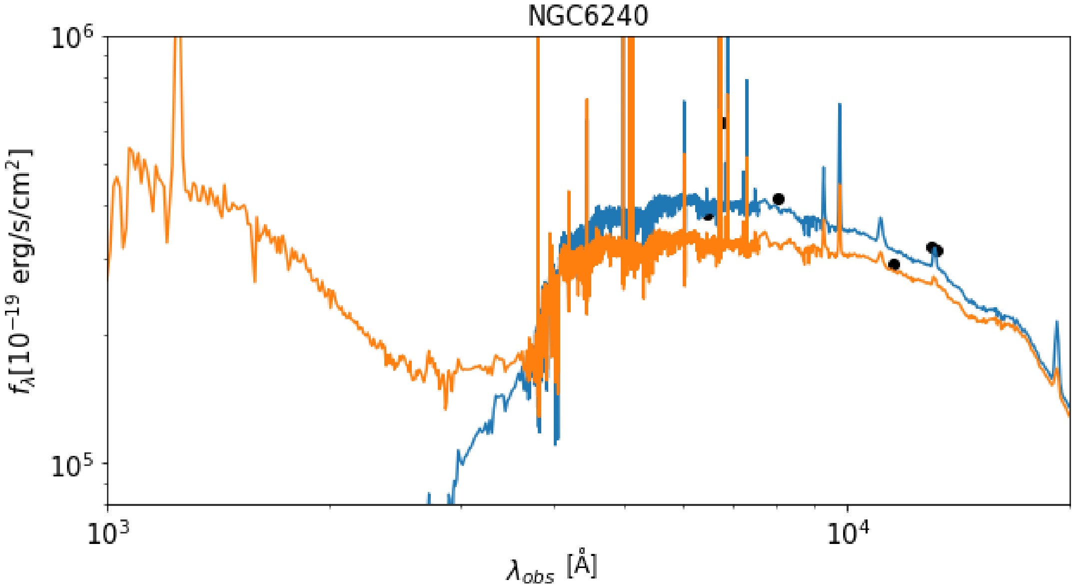
NGC6240
$f_\lambda[10^{-19}$ erg/s/cm$^2]$
10^6
10^5
10^3
10^4
λ_{obs} [Å]

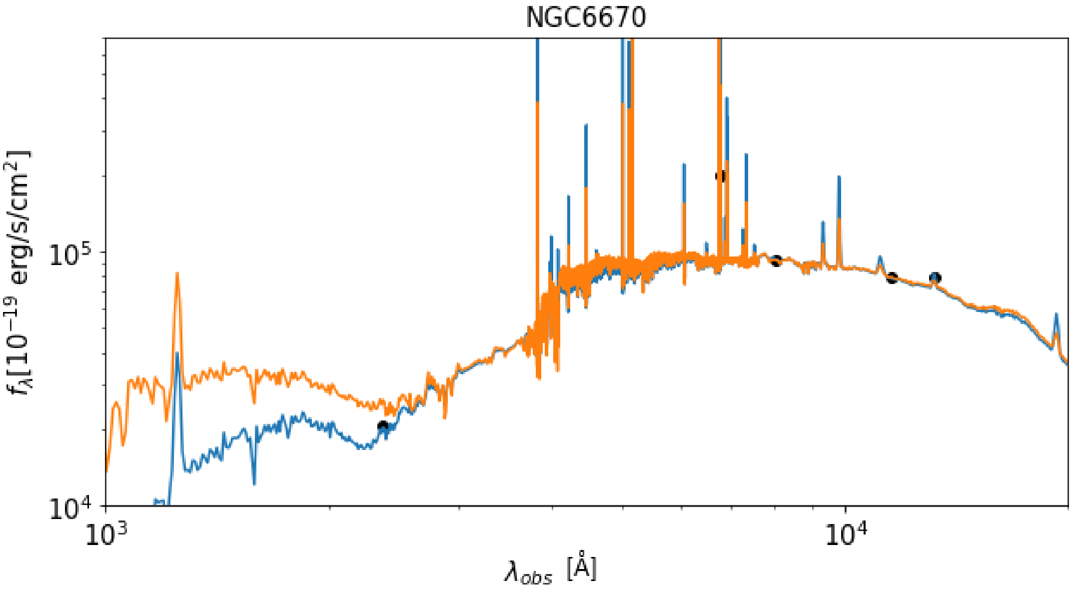
NGC6670
$f_\lambda[10^{-19}$ erg/s/cm$^2]$
10^5
10^4
10^3
10^4
λ_{obs} [Å]

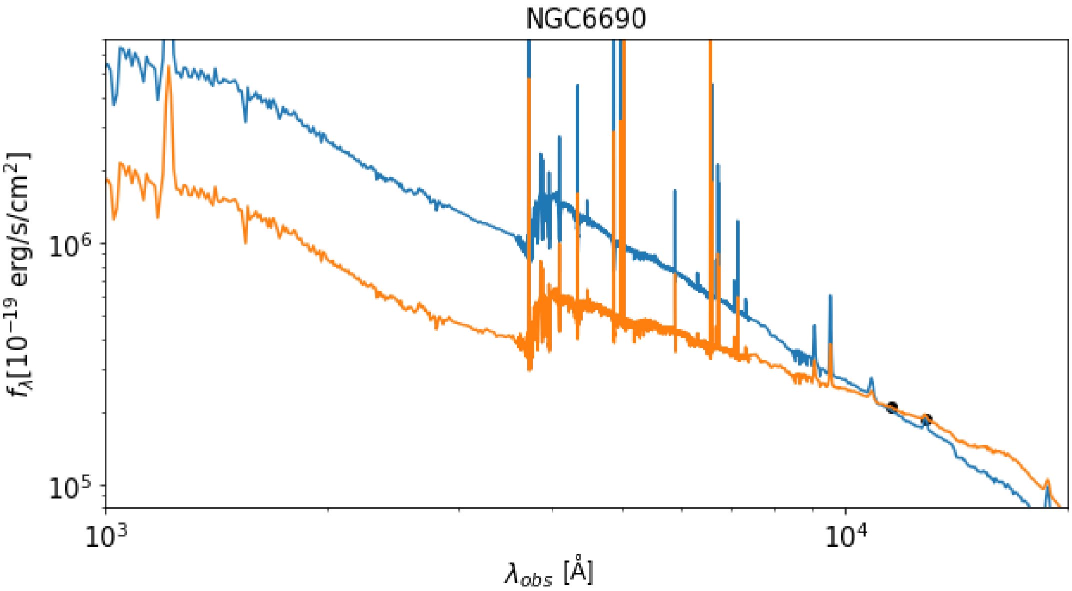
NGC6690
$f_\lambda[10^{-19}$ erg/s/cm$^2]$
10^6
10^5
10^3
10^4
λ_{obs} [Å]

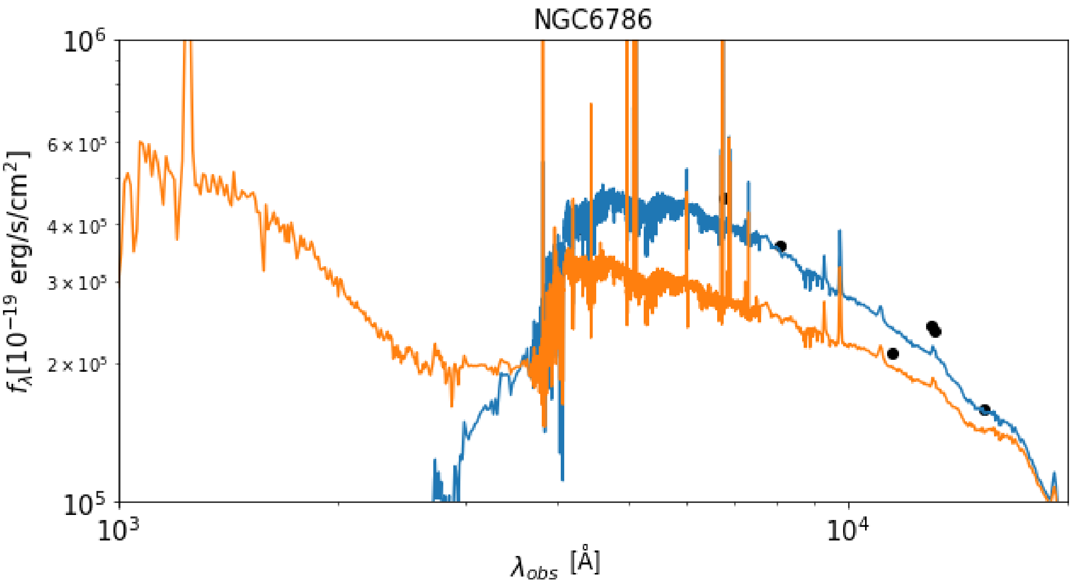
NGC6786
$f_\lambda[10^{-19}$ erg/s/cm$^2]$
10^6
6×10^5
4×10^5
3×10^5
2×10^5
10^5
10^3
10^4
λ_{obs} [Å]

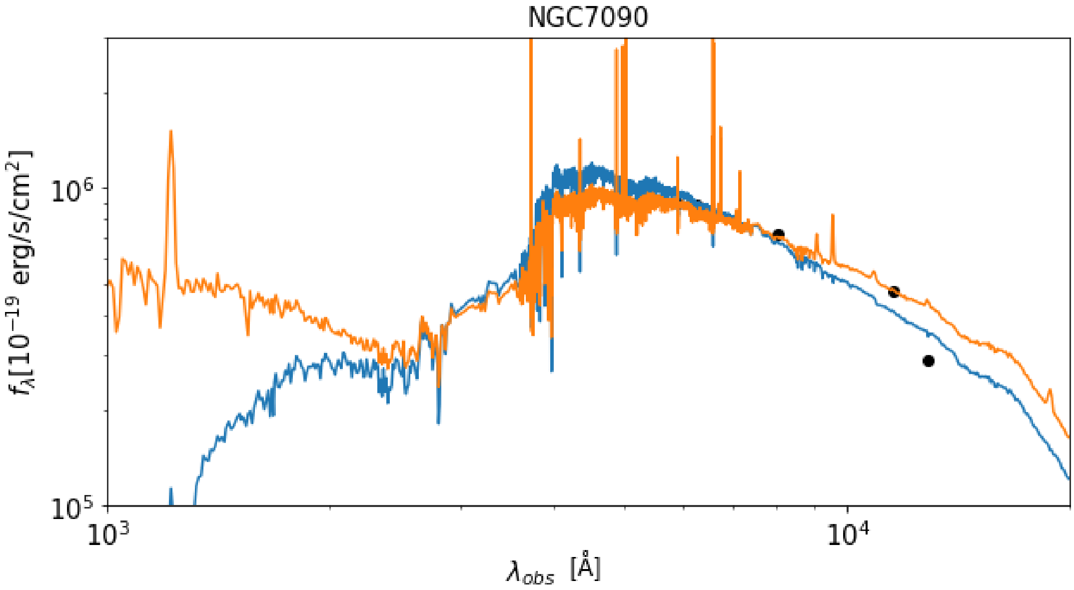
NGC7090
$f_\lambda[10^{-19}$ erg/s/cm$^2]$
10^6
10^5
10^3
10^4
λ_{obs} [Å]

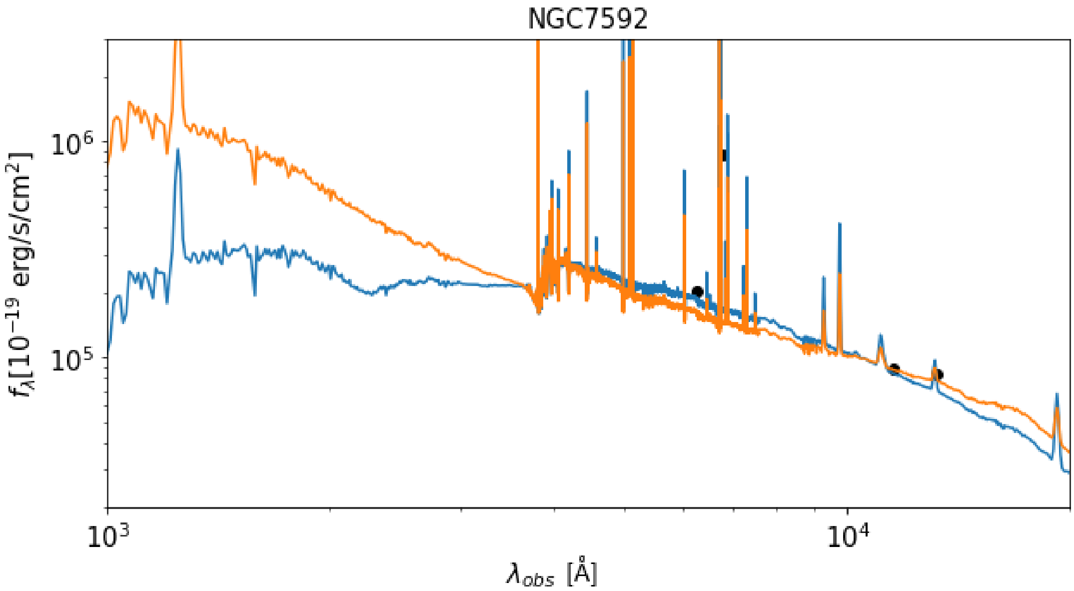
NGC7592
$f_\lambda[10^{-19}$ erg/s/cm$^2]$
10^6
10^5
10^3
10^4
λ_{obs} [Å]

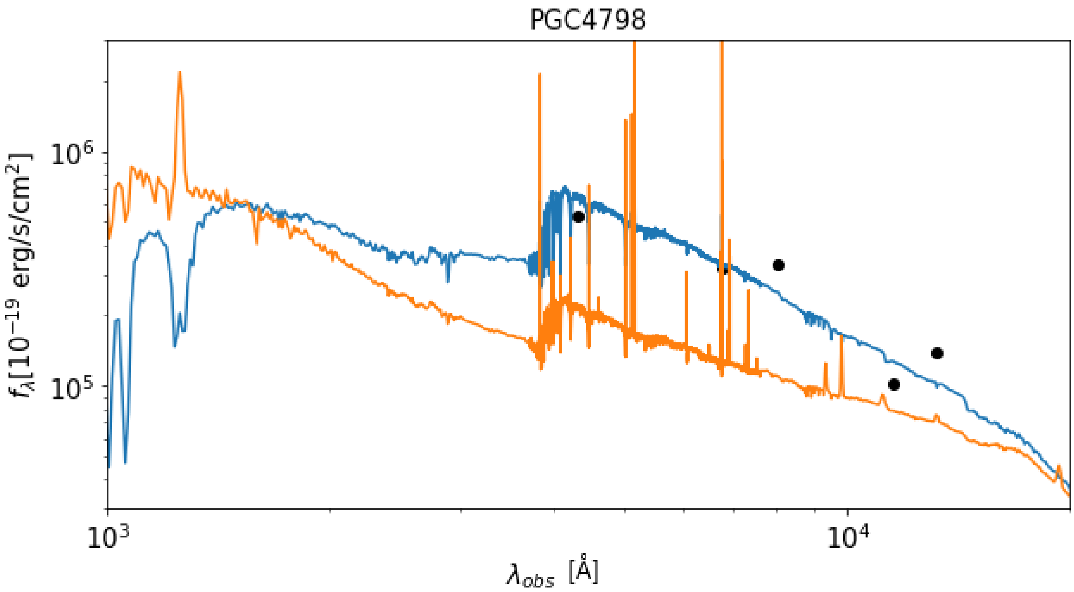
PGC4798
$f_\lambda[10^{-19}$ erg/s/cm$^2]$
10^6
10^5
10^3
10^4
λ_{obs} [Å]

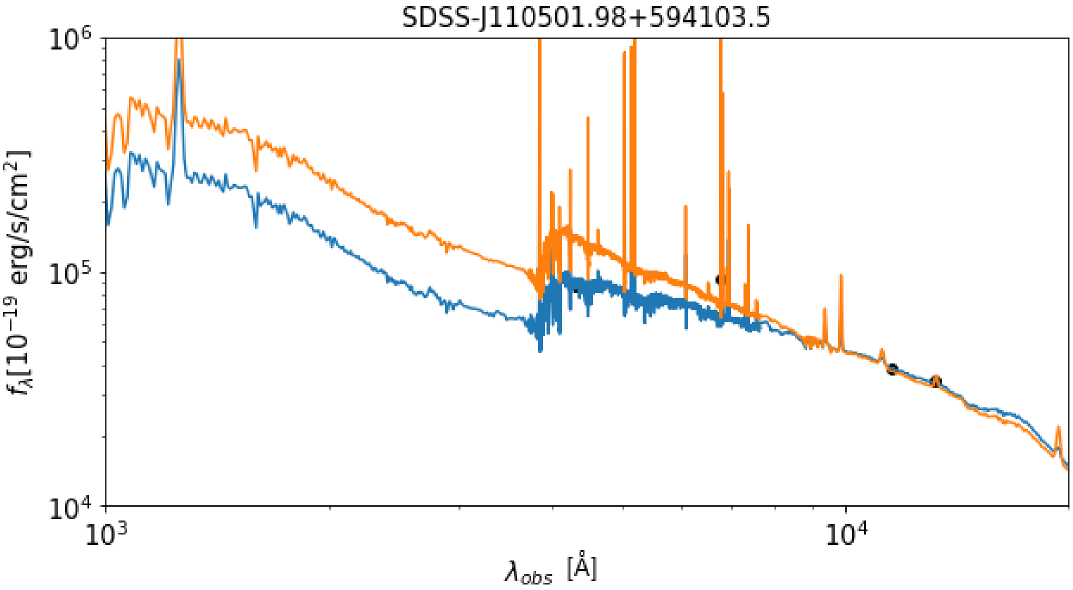
SDSS-J110501.98+594103.5
10^6
10^5
10^4
$f_\lambda[10^{-19}$ erg/s/cm^2]
10^3
10^4
λ_{obs} [Å]

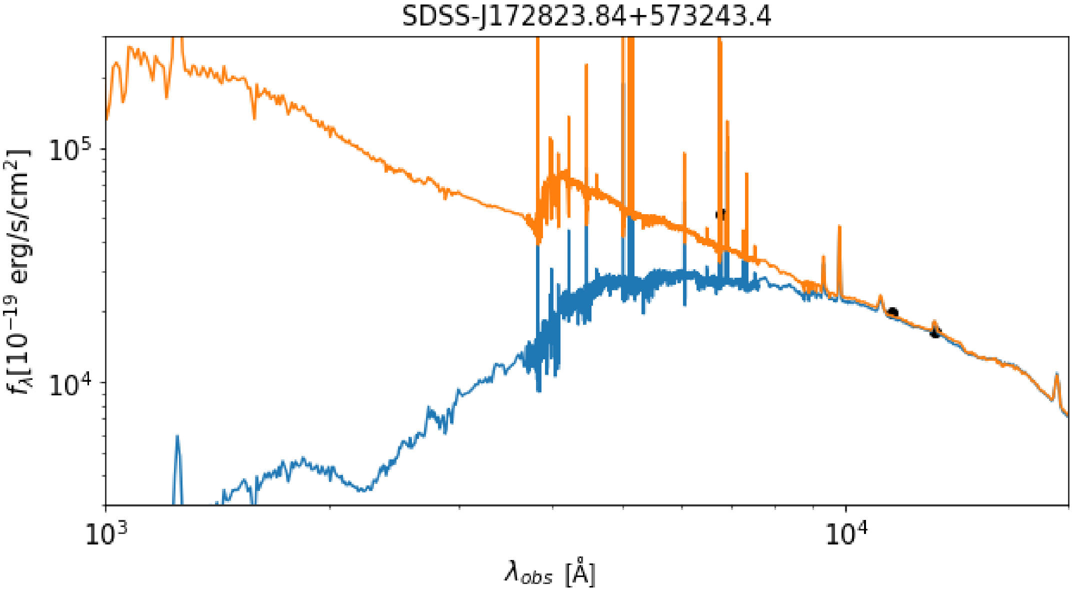
SDSS-J172823.84+573243.4
10^5
10^4
$f_\lambda[10^{-19}$ erg/s/cm^2]
10^3
10^4
λ_{obs} [Å]

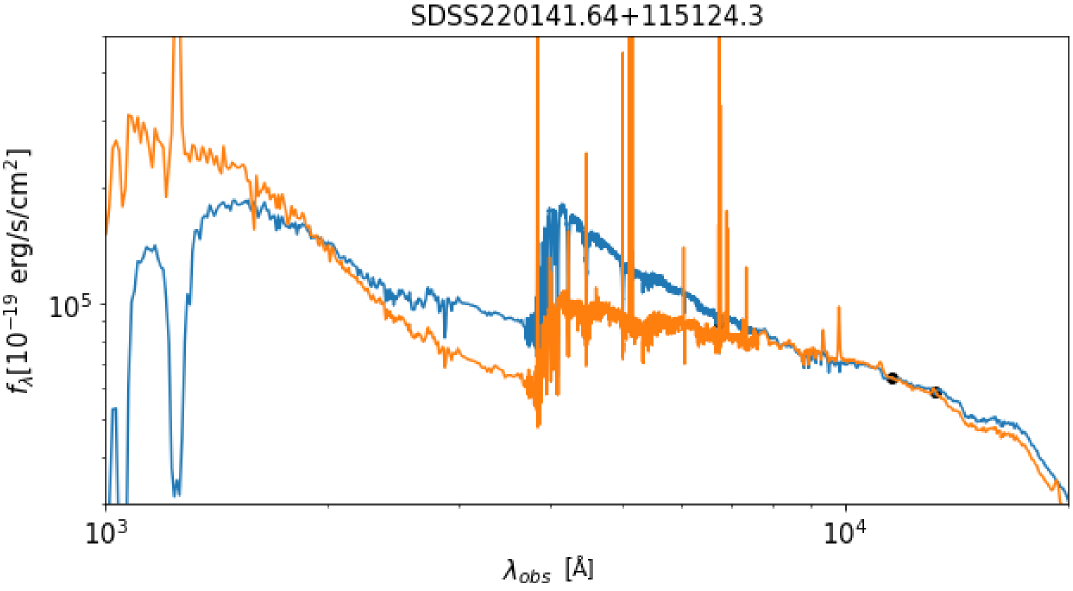
SDSS220141.64+115124.3
10^5
$f_\lambda[10^{-19}$ erg/s/cm^2]
10^3
10^4
λ_{obs} [Å]

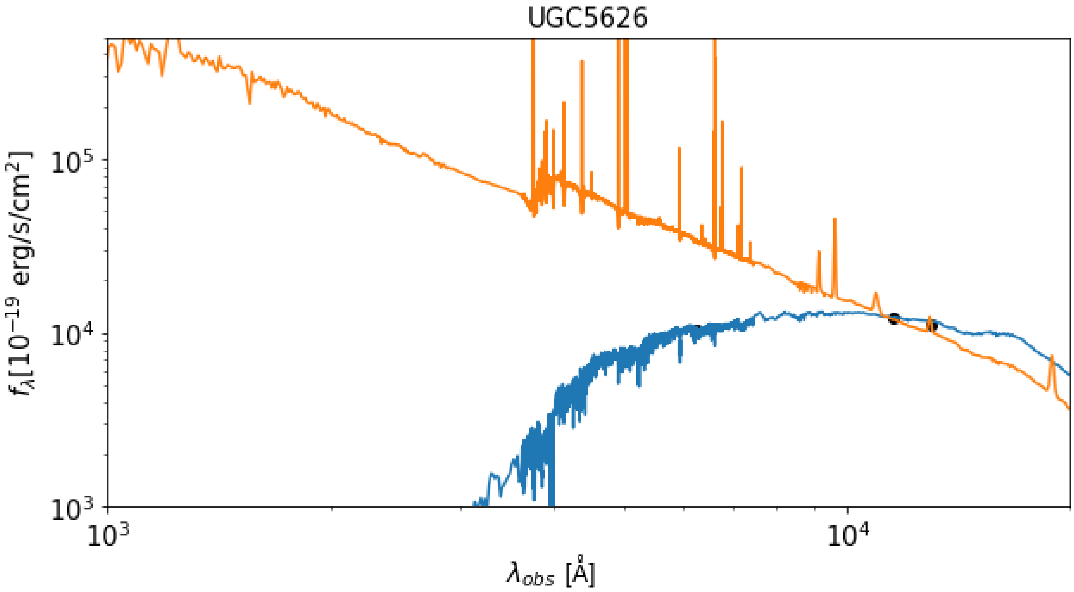
UGC5626
$f_\lambda[10^{-19}$ erg/s/cm$^2]$
10^5
10^4
10^3
10^3
10^4
λ_{obs} [Å]

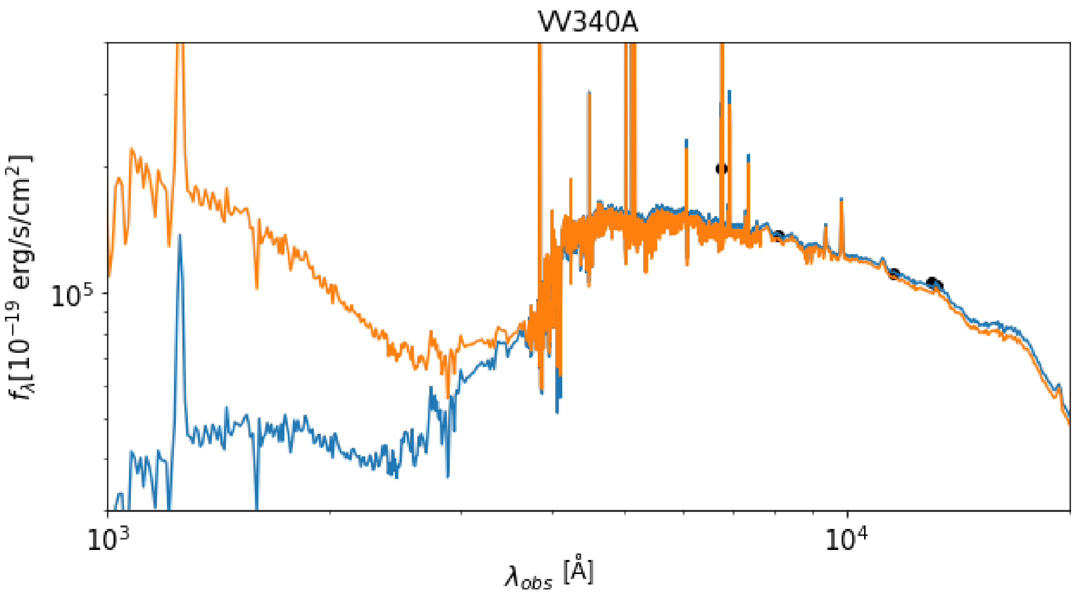
VV340A
$f_\lambda[10^{-19}$ erg/s/cm$^2]$
10^5
10^3
10^4
λ_{obs} [Å]